n

Palacios, Leonel M. (2016) *Autonomous formation flying: unified control and collision avoidance methods for close manoeuvring spacecraft.* PhD thesis.

http://theses.gla.ac.uk/7765/

Copyright and moral rights for this work are retained by the author

A copy can be downloaded for personal non-commercial research or study, without prior permission or charge

This work cannot be reproduced or quoted extensively from without first obtaining permission in writing from the author

The content must not be changed in any way or sold commercially in any format or medium without the formal permission of the author

When referring to this work, full bibliographic details including the author, title, awarding institution and date of the thesis must be given

Glasgow Theses Service
http://theses.gla.ac.uk/
theses@gla.ac.uk

Autonomous Formation Flying

Unified Control and Collision Avoidance Methods for Close Manoeuvring Spacecraft

Leonel M. Palacios

School of Engineering

Aerospace Sciences Research Division

University of Glasgow

Submitted in fulfillment of the requirements for the degree of

Doctor of Philosophy

November 2016

Abstract

The idea of spacecraft formations, flying in tight configurations with maximum baselines of a few hundred meters in low-Earth orbits, has generated widespread interest over the last several years. Nevertheless, controlling the movement of spacecraft in formation poses difficulties, such as in-orbit high-computing demand and collision avoidance capabilities, which escalate as the number of units in the formation is increased and complicated nonlinear effects are imposed to the dynamics, together with uncertainty which may arise from the lack of knowledge of system parameters. These requirements have led to the need of reliable linear and nonlinear controllers in terms of relative and absolute dynamics.

The objective of this thesis is, therefore, to introduce new control methods to allow spacecraft in formation, with circular/elliptical reference orbits, to efficiently execute safe autonomous manoeuvres. These controllers distinguish from the bulk of literature in that they merge guidance laws never applied before to spacecraft formation flying and collision avoidance capacities into a single control strategy. For this purpose, three control schemes are presented: linear optimal regulation, linear optimal estimation and adaptive nonlinear control. In general terms, the proposed control approaches command the dynamical performance of one or several followers with respect to a leader to asymptotically track a time-varying nominal trajectory (TVNT), while the threat of collision between the followers is reduced by repelling accelerations obtained from the collision avoidance scheme during the periods of closest proximity.

Linear optimal regulation is achieved through a Riccati-based tracking controller. Within this control strategy, the controller provides guidance and tracking toward a desired TVNT, optimizing fuel consumption by Riccati procedure using a non-infinite cost function defined in terms of the desired TVNT, while repelling accelerations generated from the CAS will ensure evasive actions between the elements of the formation. The relative dynamics model, suitable for circular and eccentric low-Earth

reference orbits, is based on the Tschauner and Hempel equations, and includes a control input and a nonlinear term corresponding to the CAS repelling accelerations.

Linear optimal estimation is built on the forward-in-time separation principle. This controller encompasses two stages: regulation and estimation. The first stage requires the design of a full state feedback controller using the state vector reconstructed by means of the estimator. The second stage requires the design of an additional dynamical system, the estimator, to obtain the states which cannot be measured in order to approximately reconstruct the full state vector. Then, the separation principle states that an observer built for a known input can also be used to estimate the state of the system and to generate the control input. This allows the design of the observer and the feedback independently, by exploiting the advantages of linear quadratic regulator theory, in order to estimate the states of a dynamical system with model and sensor uncertainty. The relative dynamics is described with the linear system used in the previous controller, with a control input and nonlinearities entering via the repelling accelerations from the CAS during collision avoidance events. Moreover, sensor uncertainty is added to the control process by considering carrier-phase differential GPS (CDGPS) velocity measurement error.

An adaptive control law capable of delivering superior closed-loop performance when compared to the certainty-equivalence (CE) adaptive controllers is finally presented. A novel noncertainty-equivalence controller based on the Immersion and Invariance paradigm for close-manoeuvring spacecraft formation flying in both circular and elliptical low-Earth reference orbits is introduced. The proposed control scheme achieves stabilization by immersing the plant dynamics into a target dynamical system (or manifold) that captures the desired dynamical behaviour. They key feature of this methodology is the addition of a new term to the classical certainty-equivalence control approach that, in conjunction with the parameter update law, is designed to achieve adaptive stabilization. This parameter has the ultimate task of shaping the manifold into which the adaptive system is immersed. The performance of the controller is proven stable via a Lyapunov-based analysis and Barbalat’s lemma.

In order to evaluate the design of the controllers, test cases based on the physical and orbital features of the Prototype Research Instruments and Space Mission Technology Advancement (PRISMA) are implemented, extending the number of elements in the formation into scenarios with reconfigurations and on-orbit position switching in elliptical low-Earth reference orbits. An extensive analysis and comparison of the performance of the controllers in terms of total Δv and fuel consumption, with and without the effects of the CAS, is presented. These results show that the three proposed controllers allow the followers to asymptotically track the desired nominal trajectory and, additionally, those simulations including CAS show an effective decrease of collision risk during the performance of the manoeuvre.

Table of contents

List of tables viii

List of figures x

Nomenclature xv

1 Introduction 1

1.1 Spacecraft Formation Flying . . . 1

1.2 Autonomous Control of Spacecraft . . . 3

1.3 Control Architectures in Spacecraft Formation Flying . . . 5

1.4 Relevant Literature Survey on Spacecraft Formation Flying Control . . . 7

1.4.1 Fuel Optimisation and Low Computational Resources . . . 7

1.4.2 Non-Classic Control and Collision Avoidance . . . 10

1.4.3 Nonlinear Control . . . 11

1.5 Current Spacecraft Formation Flying Missions . . . 12

1.5.1 TanDEM-X Autonomous Formation Flying System . . . 13

1.5.2 PRISMA Mission . . . 14

1.5.3 PROBA-3 Mission . . . 17

1.6 Thesis Objectives and Contributions . . . 20

1.7 Thesis Structure . . . 21

1.8 Thesis Outputs . . . 22

2 Equations of Motion 25

2.1 Reference Frames . . . 25

2.2 The Equations of Relative Motion 26
2.3 Linearized Translational Relative Dynamics 28
2.4 State-Space Representation and Error Dynamics 30
2.5 External Perturbations 31

3 Spacecraft Formation Flying Control via Linear Optimal Tracking and Artificial Potential Functions 34

3.1 Linear Quadratic Regulation 35
3.2 Kalman Controllability Conditions 38
3.3 Selection of the Weight Matrices 38
3.4 Control Strategy Design 40
    3.4.1 LQR-Based Control 40
    3.4.2 Obstacle Avoidance Scheme 43
    3.4.3 Final Control Strategy 45
3.5 Simulations 46
    3.5.1 Scenario 1 47
    3.5.2 Scenario 2 51
    3.5.3 Scenario 3 54
3.6 Chapter Conclusions 56

4 Spacecraft Formation Flying Control via State Estimation and Artificial Potential Functions 59

4.1 State Estimation 60
4.2 Conditions for Observability 62
4.3 The Forward-in-Time Separation Principle 62
4.4 Control Strategy 65
4.5 State and Model Uncertainty 67
4.6 Simulations 68
    4.6.1 Scenario 1 68
    4.6.2 Scenario 2 74
    4.6.3 Scenario 3 75

4.7 Chapter Conclusions 77

5 Spacecraft Formation Flying Control via Immersion and Invariance and Artificial Potential Functions 81

5.1 Immersion and Invariance 82

5.2 Control Strategy 84

5.3 Stability Analysis of the Controller 89

5.4 Simulations 90

5.4.1 Scenario 1 90

5.4.2 Scenario 2 96

5.4.3 Scenario 3 98

5.5 Chapter Conclusions 100

6 Conclusions and Future Work 106

6.1 Conclusions 106

6.2 Limitations of the work 109

6.3 Future work 110

6.3.1 Tuning of Control Parameters 110

6.3.2 Orbital Perturbations and Long-Time Horizons 111

6.3.3 More Realistic Simulations 111

References 112

List of tables

1.1 Summary of relevant physical features of Mango and Tango 15

1.2 Summary of Formation Flying experiments in PRISMA mission (D'Amico et al., 2013) 17

1.3 Summary of relevant physical features of the Coronagraph and Occulter 18

1.4 Summary of relevant physical features of the Coronagraph and Occulter 19

1.5 Summary of Δv values obtained in PROBA-3 mission experiments 19

3.1 Summary of equations for the solution of the linear optimal control problem 37

3.2 Initial and final conditions 42

3.3 LQR-APF control algorithm 46

3.4 Initial and final conditions in Scenario 1 47

3.5 Summary of results for Scenario 1 50

3.6 CAS parameters tune-up and corresponding Δv and fuel consumption for Mango 1. Each row represents a test case where the named parameter is set as specified, while the others are those defined in Scenario 1 50

3.7 Initial and final conditions in Scenario 2 51

3.8 Summary of results for Scenario 2 54

3.9 Initial and final conditions in Scenario 3 55

3.10 Summary of results for Scenario 3 56

4.1 SESP-CAS control algorithm 68

4.2 Initial and final conditions in Scenario 1 69

4.3 Summary of results for Scenario 1 72

4.4 CAS parameters tune-up and corresponding Δv and fuel consumption. Each row represents a test case where the named parameter is set as specified, while the others are those defined in Scenario 1 72
4.5 Weight matrices $\mathbf{W}_1(t)$ and $\mathbf{W}_2(t)$ tune-up and corresponding Δv and fuel consumption. Each row represents a test case where the named parameter is set as specified, while the others are those defined in Scenario 1 73
4.6 Initial and final conditions in Scenario 2 74
4.7 Summary of results for Scenario 2 78
4.8 Initial and final conditions in Scenario 3 78
4.9 Summary of results for Scenario 3 78

5.1 I&I-CAS control algorithm 88
5.2 Initial and final conditions in Scenario 1 90
5.3 Summary of results for Scenario 1 95
5.4 CAS parameters tune-up and corresponding Δv and fuel consumption. Each row represents a test case where the named parameter is set as specified, while the others are those defined in Scenario 1 95
5.5 Weight matrices tune-up and corresponding Δv and fuel consumption. Each row represents a test case where the named parameter is set as specified, while the others are those defined in Scenario 1 96
5.6 Initial and final conditions in Scenario 2 98
5.7 Summary of results for Scenario 2 102
5.8 Initial and final conditions in Scenario 3 102
5.9 Summary of results for Scenario 3 102

List of figures

1.1 TanDEM-X mission. Courtesy of DLR 13
1.2 Mango and Tango satellites from PRISMA mission. Courtesy of DLR 15
1.3 Proba-3 Formation Flying. Courtesy of ESA 18

2.1 Reference frames 26

3.1 State and control input with $\alpha = \beta = 1$ 39
3.2 State and control input with $\alpha = 10$ and $\beta = 1$ 40
3.3 State and control input with $\alpha = 1$ and $\beta = 10$ 40
3.4 Initial state 41
3.5 State and control input with $\alpha = 15$ and $\beta = 1$ 42
3.6 State and control input with $\alpha = 25$ and $\beta = 1$ 42
3.7 State and control input with $\alpha = 15$ and $\beta = 5$ 43
3.8 Potential Distribution with $\varepsilon_R = 3 \times 10^{-8}$ and $D = 10$ m 44
3.9 Potential Distribution with $\varepsilon_R = 3 \times 10^{-7}$ and $D = 5$ m 44
3.10 Guidance and control scheme 45
3.11 Manoeuvre trajectory in Scenario 1 48
3.12 Separation distance between the spacecraft in Scenario 1 48
3.13 Magnitude of the position error in Scenario 1 49
3.14 Magnitude of the control input in Scenario 1 49
3.15 Repulsive force used for collision avoidance in Scenario 1 49
3.16 Relevant plots with $D = 6$ m in Scenario 1 51
3.17 Relevant plots with $\sigma = 2.5$ in Scenario 1 52

3.18 Manoeuvre trajectory in Scenario 2 52

3.19 Separation distance in Scenario 2 53

3.20 Magnitude of the position error in Scenario 2 53

3.21 Magnitude of the control input in Scenario 2 53

3.22 Components of the total control input with CAS in Scenario 2 54

3.23 Manoeuvre trajectory in Scenario 3 55

3.24 Separation distance in Scenario 3 56

3.25 Magnitude of the position error in Scenario 3 56

3.26 Magnitude of the control input in Scenario 3 57

3.27 Components of the total control input with CAS in Scenario 3 57

4.1 Diagram of the control strategy 67

4.2 Manoeuvre trajectory in Scenario 1 69

4.3 Separation distance in Scenario 1 70

4.4 Magnitude of the position error in Scenario 1 70

4.5 Magnitude of the estimated position error in Scenario 1 70

4.6 Magnitude of the control input in Scenario 1 71

4.7 Components of the total control input with CAS in Scenario 1 71

4.8 Relevant plots with $D = 7\text{m}$ in Scenario 1 73

4.9 Relevant plots with $\sigma = 0.8$ in Scenario 1 73

4.10 Manoeuvre trajectory in Scenario 2 75

4.11 Separation distance in Scenario 2 75

4.12 Magnitude of the position error in Scenario 2 76

4.13 Estimated magnitude of the position error in Scenario 2 76

4.14 Magnitude of the control input in Scenario 2 77

4.15 Components of the total control input with CAS in Scenario 2 77

4.16 Manoeuvre trajectory in Scenario 3 79

4.17 Separation distance in Scenario 3 79

4.18 Magnitude of the position error in Scenario 3 80

4.19 Magnitude of the estimated position error in Scenario 3 80

4.20 Magnitude of the control input in Scenario 3 80

4.21 Components of the total control input with CAS in Scenario 3 80

5.1 Diagram of the control strategy 88

5.2 Manoeuvre trajectory in Scenario 1 91

5.3 Separation distance in Scenario 1 92

5.4 Magnitude of the position error in Scenario 1 92

5.5 Magnitude of the control input in Scenario 1 92

5.6 Components of the total control input with CAS in Scenario 1 93

5.7 Estimated parameters without CAS in Scenario 1 94

5.8 Estimated parameters with CAS in Scenario 1 94

5.9 Relevant plots with $D = 6$ m in Scenario 1 96

5.10 Relevant plots with $\sigma = 6$ in Scenario 1 97

5.11 Relevant plots with $\Gamma = 10$ in Scenario 1 97

5.12 Manoeuvre trajectory in Scenario 2 98

5.13 Separation distance in Scenario 2 99

5.14 Magnitude of the position error in Scenario 2 99

5.15 Magnitude of the control input in Scenario 2 100

5.16 Components of the total control input with CAS in Scenario 2 100

5.17 Estimated parameters without CAS in Scenario 2 101

5.18 Estimated parameters with CAS in Scenario 2 101

5.19 Manoeuvre trajectory in Scenario 3 103

5.20 Separation distance in Scenario 3 103

5.21 Magnitude of the position error in Scenario 3 104

5.22 Magnitude of the control input in Scenario 3 104

5.23 Components of the total control input with CAS in Scenario 3 104

5.24 Estimated parameters without CAS in Scenario 3 105

5.25 Estimated parameters with CAS in Scenario 3 105

Acknowledgements

Scotland… There are not enough words in my mind to express the bliss in my heart when I think of my days in this glorious country. And it is not only memories from the many sights I witnessed during my trips to the Highlands, the islands of Mull and Arran or from the numerous majestic fairy-tale castles, but the people I met there, the scent of early morning wind every time I left my apartment, the light rain in my face when I walked back from office and the peaceful sensation embracing my very soul every time I toured the halls of the University of Glasgow. I am humbly thankful to God, for the blessing of my time in Scotland.

However, I wonder, how can someone truly value such experience? For me, the key was mindful balance, which flows to my life through the happiness of my soulmate, Luz Gonzalez. I will never forget her smile embellished with the flowers of the glasshouses in the Botanical Gardens or the sun light shining in her hair, like the copper-coloured autumn leaves in the trees of Kelvingrove Park. I am (and will be) eternally thankful for her warming and unconditional love, her company and support during our adventure in Scotland.

Travelling and living far away from home is not always a simple venture, however, the burden of distance can be faded thanks to family support. Throughout my life, my mother Malena Moreno and my brother Jorge Palacios, have unconditionally bestowed upon me all the love, blessings and support that only family can provide. They trusted me in every challenge without hesitating about my capacities. It is because of them and the countless experiences we have lived together, that I became the man I am now. I am truly thankful to them.

I would like to express my full gratitude to my supervisor, Dr. Gianmarco Radice, for the technical advice, patience and encouragement he has provided throughout my time as his student. He created the perfect balance between student freedom and supervision, which made the four years of my doctoral degree one of the best academic experiences so far in my life. It is also my wish to thank Dr. Matteo Ceriotti. His guidance, patience and teachings were keys to my success in obtaining the doctoral degree. I would also like to thank with all my heart to all the true friends I met in Glasgow. In particular, I would like to thank Iain Moore, Susana Garcia, Olga Linden, Caroline Pearson, Ana Perez, Alessandro Peloni, Alisha Contractor, Abdul Lawal, Sittiporn Channumsin, Aldo Vargas, Spencer Sivoman, Nicola Sullo, Yohei Sugimoto and Chenthamarai Pandian. You made rainy and windy days in Glasgow warm, bright and colourful. You made me feel at home. Thanks to you, all these years in Scotland were the best of my life.

To the memory of my beloved father, Leonel

To my wife, Luz

Nomenclature

Chapter 2

$\mathbf{A}$	linear dynamics matrix
a	semimajor axis of the leader's orbit
$\boldsymbol{a}_D$	perturbation acceleration due to atmospheric drag
$\boldsymbol{a}_J$	perturbation acceleration due to Earth oblateness
a_n	components of the external acceleration perturbation vector $\boldsymbol{a}$ with $n = x, y, z$
$\boldsymbol{a}$	external perturbation acceleration vector
$\mathbf{B}$	control matrix
$\boldsymbol{b}_n$	set of orthonormal right-handed unit base vectors of the frame $\mathcal{B}$
C_D	drag coefficient
$\ddot{\theta}$	second time derivative of the true anomaly
$\dot{\theta}$	first time derivative of the true anomaly
$\delta\boldsymbol{x}$	tracking error dynamics
e	eccentricity of the leader's orbit
$\mathbf{F}$	external perturbation force vector
$\mathbf{G}$	velocity matrix

$\mathbf{H}$	position matrix
$\boldsymbol{i}_n$	set of orthonormal right-handed unit base vectors of the frame $\mathcal{I}$
J_2	zonal harmonic coefficient
$\boldsymbol{k}$	auxiliar vector of the perturbation $\boldsymbol{a}_J$
$\boldsymbol{l}_n$	set of orthonormal right-handed unit base vectors of the frame $\mathcal{L}$
m_F	mass of the follower
m_L	mass of the leader
μ	gravitational parameter
n	mean motion of the leader's orbit
$\boldsymbol{\omega}$	angular velocity of the $\mathcal{L}$ frame
r	magnitude of the orbital position of the leader spacecraft
r_E	radius of the Earth
$\boldsymbol{r}_F$	absolute orbit position of the follower spacecraft
ρ	atmospheric density
$\boldsymbol{r}_L$	absolute orbit position of the leader spacecraft
$\mathbb{R}^{n\times m}$	set of $n \times m$ real matrices
$\mathbb{R}^n$	real column vectors
S	cross-section area
u_n	components of the control input signal $\boldsymbol{u}$ with $n = x, y, z$
$\boldsymbol{u}$	control input signal
$\boldsymbol{v}$	relative velocity of the follower

$\boldsymbol{\varrho}$	relative position of the follower with respect to the leader
$\boldsymbol{v}_{atm}$	velocity of the atmosphere at the follower position
ω_E	angular velocity of Earth
$\boldsymbol{x}$	follower state vector
$\boldsymbol{x}_D$	follower desired state vector
x, y, z	components of the relative position vector $\boldsymbol{\varrho}$

Chapter 3

$\mathbf{A}$	dynamics matrix
A	positive constant defining the obstacle shape in the CAS
α	tuning parameter of $\mathbf{Q}$
$\boldsymbol{a}_R$	accelerations due to the CAS
$\mathbf{B}$	control matrix
β	tuning parameter of $\mathbf{R}$
D	effective dimension of the obstacle in the CAS
Δv	delta-v
$\delta \boldsymbol{x}$	state-space relative dynamics vector
$\mathbf{F}$	terminal cost weight matrix
g_0	acceleration due to gravity at sea level
H	Hamiltonian of a dynamical system
$\boldsymbol{I}$	identity matrix
I_{sp}	specific impulse

$\boldsymbol{\Phi}$	state transition matrix
$\mathcal{J}$	cost functional
$\mathbf{K}$	Kalman gain
$\boldsymbol{\lambda}$	costate vector
$\boldsymbol{\lambda}^*$	optimal costate vector
m_0	initial mass of the follower
$\mathbf{P}$	solution to the differential Riccati equation
$\mathbf{Q}$	the error weighted matrix
$\mathbf{R}$	the control weighted matrix
σ	width of the Gaussian function in the CAS
$\boldsymbol{u}$	control input
ε_R	tuning parameter of the CAS
$\boldsymbol{\varrho}_D$	desired relative position
$\boldsymbol{v}_D$	desired relative velocity
$\mathbf{W}_c$	controllability Grammian
$\boldsymbol{x}$	state vector
$\boldsymbol{x}_D$	desired relative state
$\boldsymbol{x}_o$	position of the obstacle spacecraft
$\boldsymbol{x}^*$	optimal state vector

Chapter 4

$\mathbf{A}$	dynamics matrix

$\bar{\mathbf{A}}$	auxiliar matrix of $\mathbf{A}$
$\boldsymbol{a}_R$	acceleration due to the CAS as defined in Chapter 3
$\mathbf{B}$	control matrix
$\bar{\mathbf{B}}$	auxiliar matrix of $\mathbf{B}$
$\mathbf{C}$	measurement matrix
$\delta\boldsymbol{x}$	relative state error vector
$\delta\boldsymbol{y}$	relative state error vector output
$\boldsymbol{e}$	error state vector
E	mean square reconstruction error
$\mathbf{K}$	Kalman gain
$\mathbf{L}$	gain matrix of the observer
$\mathbf{P}$	solution to the DRE
$\mathbf{\Phi}$	state transition matrix
$\mathbf{Q}$	state weight matrix
$\mathbf{R}$	control input weight matrix
$\mathbf{T}$	auxiliar matrix
$\boldsymbol{u}$	control input
$\mathbf{V}$	mean square construction error matrix
$\mathbf{W}$	weight matrix of E
$\boldsymbol{w}_1$	state excitation noise
$\mathbf{W}_1$	weight matrix for model uncertainty

$\boldsymbol{w}_2$	observation noise
$\mathbf{W}_2$	weight matrix for sensor uncertainty
$\mathbf{W}_o$	observability Grammian
$\boldsymbol{x}$	state vector
$\hat{\boldsymbol{x}}$	estimated state
$\boldsymbol{y}$	output vector

Chapter 5

$\boldsymbol{a}_J$	perturbation acceleration due to J_2 as defined in Chapter 2
$\boldsymbol{a}_R$	repelling acceleration due to CAS as defined in Chapter 3
α,κ	positive constant design parameters used to control the rate of position and velocity errors
$\boldsymbol{a}_D$	perturbation acceleration due to atmospheric drag as defined in Chapter 2
$\boldsymbol{a}_T$	the sum of all perturbation accelerations
$\boldsymbol{\beta}$	vector function used to provide shape to the manifold $\mathcal{M}$
$\delta\boldsymbol{x}$	relative state error vector
ϵ	auxiliar variable
$\boldsymbol{f}$	generic vector function
$\boldsymbol{g}$	generic matrix function
Γ	positive constant design parameter for $\boldsymbol{\beta}$
$\hat{\boldsymbol{\varepsilon}}$	estimation of the uncertain parameter vector
$\mathbf{M}$	mass matrix of the follower
$\mathcal{M}$	manifold

$\boldsymbol{u}$	feedback control law
$\boldsymbol{u}_f$	linear filter for the control input
$\boldsymbol{\varepsilon}$	uncertain parameter vector
$\mathbf{W}$	regression matrix
$\mathbf{W}_f$	linear filter for the regression matrix
$\boldsymbol{x}$	generic state vector
$\boldsymbol{x}_D$	generic nominal or desired state vector
$\boldsymbol{x}_f$	linear filter for the state error
$\boldsymbol{z}$	estimation error vector

Acronyms / Abbreviations

APF	Artificial Potential Function
CAS	Collision Avoidance Scheme
DRE	Differential Riccati Equation
DSS	Distributed Space Systems
FFC	Formation Flying Control
I&I	Immersion and Invariance
LQR	Linear Quadratic Regulator
MIMO	Multiple-Input, Multiple-Output
SAR	synthetic aperture radar
SESP	State Estimation by Separation Principle
SFF	Spacecraft Formation Flying
TVNT	Time-Varying Nominal Trajectory

Chapter 1

Introduction

1.1 Spacecraft Formation Flying

Distributed Space Systems (DSS) are a technological concept in which several coordinated satellites work together in order to perform a specific mission. Within DSS, the major tasks performed by a satellite, commonly handled by a single monolithic unit, are distributed among several smaller spacecraft so that challenging mission objectives, otherwise impossible to obtain, can be achieved. These tasks may include several spacecraft acting as one, very large, synthetic aperture radar, simultaneous multipoint sensing and data fusion from different payloads. Different terminology for DSS applications has been proposed in literature according to mission features, the most usual being, constellations, formations of spacecraft, clusters and swarms.

The first of these terms refers to a group of satellites sparsely distributed without any direct interaction between its elements nor on-board control of relative positions or orientation. After launch and initial correcting manoeuvers, adjusting a spacecraft orbit would be an occasional activity planned from the ground. This paradigm is typically used for Earth observation, communication, geolocation and meteorology. A cluster is formed by a group of spacecraft sharing a common reference orbit and orbiting close to each other in order to increase sensing capabilities. They are required to maintain inter-spacecraft distances bounded for the entire mission lifetime. A formation of spacecraft, on the other hand, additionally requires the tracking or maintenance of a desired relative separation, orientation or position between or among spacecraft (Alfriend et al., 2009). These type of DSS is usually considered for missions such as in-orbit inspection, Synthetic Aperture Radar (SAR) interferometry, magnetospheric observation and gravimetry. The duration of the mission is the aspect that differentiates formation flying from rendezvous missions, yielding thus to different control requirements and, in most cases, to other dynamical representations (D'Errico, 2013). A swarm mission implies a larger number of small spacecraft, usually nano or pico in size, orbiting close to each other with decentralised control inspired from the behaviour of social insects like ants and bees. Some applications for swarm mission could be coordinated observation, planet exploration, and on-orbit self-assembly (Pinciroli et al., 2008). Although control requirements for DSS depend mainly on the nature of every mission, fuel use optimisation is expected to be a primary concern for orbit maintenance. Additional aspects affecting fuel use are initial conditions, navigation uncertainties, atmospheric drag, thrusting errors and dynamical process noise.

This thesis deals with the formation flying dynamics of clusters or Spacecraft Formation Flying (SFF). In general, SFF is usually defined in terms of relative motion of a follower with respect to a leader in a non-inertial reference frame attached to the latter. The dynamical problem of relative SFF is then defined as the developing of the relative position, velocity and attitude of the follower with respect to the leader as a function of time (or true anomaly) in the Local-Vertical-Local-Horizontal (LVLH or $\mathcal{L}$) frame, once the absolute motion of the leader is determined.

There are several potential advantages of DSS missions (Alfriend et al., 2009; D'Errico, 2013; Helvajian, 1999; Tollefson, 2001). Distributing mission functions among several smaller satellites may enable multiple-mission capabilities and mission design flexibility due to on-orbit reconfiguration capabilities, such as, spacecraft redistribution, position switch, orbital transfers and layout expansion/contraction. Since the spacecraft within the formation may redistribute, change configuration geometry, extend or contract the formation or adapt the mission by adding new spacecraft to the formation, missions can be more versatile thus augmenting the scientific output. Depending on the nature of the mission and if functionality redundancy exists, fault tolerance may be improved in SFF by re-distributing tasks between the spacecraft within the formation. If a mission uses miniature or small satellites, the launch cost would be reduced if the satellites are stacked as secondary payload within the launcher. Also, since miniature satellites are now being designed using simpler mass-produced components, there is potential reduction in payload technical complexity and manufacturing costs.

On the other hand, SFF also presents some potential disadvantages (Alfriend et al., 2009; D'Errico, 2013; Helvajian, 1999; Tollefson, 2001); for example, there is no standard technical procedure that dictates how to distribute the functions of a massive spacecraft within several smaller satellites, which may lead to inconsistent quality of design, mission performance variation and procedural errors due to misinterpretation of non-standard information. Moreover, spacecraft misalignment may produce communication problems. For instance, misaligned spacecraft within the formation and sensors complicate the exchange and distribution of information while introducing measurements errors. On a technical level, spacecraft operations, such as initialisation and formation maintenance, become more complex and require sophisticated procedures (Helvajian, 1999; Tollefson, 2001). Finally, there is a potential threat of space debris increase when no de-orbit plan has been included in the missions (Bastida Virgili et al., 2016).

1.2 Autonomous Control of Spacecraft

The term autonomous means having the faculty of self-governing, therefore an autonomous controller is one with the ability to self-regulate its performance with little or no human interaction (Antsaklis et al., 1991). Autonomous control systems must perform when significant uncertainties in the plant and the environment are present over long time scales. Additionally, they should adapt and compensate in case of system failures, while planning and executing the necessary control sequence toward the desired control objectives, such as tracking (or in other words, to keep the system output close a desired output) and regulation (that is, to keep the system output close to zero) (Antsaklis et al., 1991; Starek et al., 2016).

The interest of the engineering community for autonomy in SFF has grown over the last decade as access to space improves and mission frequency grows due to space commercialisation, thus opening the way for several important needs (D'Errico, 2013; Scharf et al., 2004; Starek et al., 2016). The increase in the frequency of SFF missions (Bandyopadhyay et al., 2016; CSA, 2015; ESA, 2015; Peters et al., 2014; UrtheCast, 2015) will make a ground-based control centre for each spacecraft in the formation prohibitive due to scheduling conflicts and massively increases in operational costs. Also, the larger number of spacecraft in orbit will increase the chance for human error (D'Errico, 2013). Autonomous control may satisfy these constraints while enabling numerous new missions (Starek et al., 2016). Novel real-time, on-board guidance and control algorithms must be developed to meet the challenges of SFF autonomy, particularly during translational, attitude and collision avoidance manoeuvres. In general, on-line orbit integration is used to propagate the orbital state variables between measurements required for closed-loop orbit control. This imposes constraints in terms of complexity and on the allowed computational memory resources. Since the computational processing power of most satellites is limited, this usually imply that those algorithms should be as simple as possible, while providing good estimates of the states (Gurfil, 2003). Moreover, having a large group of spacecraft manoeuvring at close distances of a few meters requires implementing even more complex and sophisticated control algorithms. One way to confront all these needs is by designing robust, real-time implementable and verifiable autonomous control systems using available computational resources (Starek et al., 2016). The interest in developing autonomy technologies for SFF have several additional motivations (D'Errico, 2013). The significant resources used to operate ground control facilities and staff in order to command spacecraft currently accounts for around 5% of the total cost of a mission per year (D'Errico, 2013). Implementing autonomous control schemes would contribute significantly to the decrease of these costs. An additional motivation is the possibility to overcome periods of inactivity and ensure maximum efficiency in spacecraft resources by granting some degree of autonomy to the elements of the formation, avoiding communication delays and ground control scheduling. Other important desired aspects in every mission are robustness, adaptability and responsiveness (Wertz, 2005). Spacecraft in formation must be able to adapt their behaviour under non-ideal conditions and to rapidly respond to changes in its environment, for example in case of failures or in the presence of uncertainties and danger. Moreover, SFF is a complex dynamical problem which escalates as the number of spacecraft increases and severe constraints are imposed - such as a large number of elements in the formation, close manoeuvring operations, complicated nonlinear dynamics, collision avoidance capabilities and optimal fuel and time restrictions - generating heavy operational and computational loads. The design of novel autonomous approaches could provide an acceptable means to handle the complexities typically associated with in-orbit operations. Finally, after considering all the previous motivations, high-level autonomy may be regarded as an enabler for new mission concepts such as highly-responsive swarms of spacecraft (D'Errico, 2013) applied, for example, to emergency/disaster assistance services and imminent collision avoidance systems to avoid crashes between the elements of the formation, external spacecraft or debris. Further applications may include (Bandyopadhyay et al., 2016) high-precision observations instruments, improved global positioning systems, experiments to increase the body of knowledge in advance theoretical topics such as relativistic and quantum mechanics, high-precision measurement instruments, enhance weather prediction, in-orbit assembly, assistance in space situational awareness, among many others.

1.3 Control Architectures in Spacecraft Formation Flying

The process of designing control and stabilisation architectures in SFF is called formation flying control (FFC). In SFF, at least one member of the formation must be tracking a desired state relative to another spacecraft in the formation and the associated tracking control law must, at least, be function of the state of this other spacecraft. A control law satisfying the latter condition is termed formation tracking control law and typically also includes regulation within its context (Alfriend et al., 2009). Several coordination approaches, that exploit the coupled nature of SFF, have been proposed in literature (Alfriend et al., 2009; Scharf et al., 2004). The Multiple-Input, Multiple-Output (MIMO) control architectures are designed using a dynamical model comprising the entire formation in which all the methods of modern control, such as those techniques based on time-domain state-space representation, may be applied to achieve formation control (Alfriend et al., 2009; D'Errico, 2013; Scharf et al., 2004). In MIMO systems several components of the state of the spacecraft are controlled by several control inputs. Notice, however, that the number of states does not need to be the same as the number of control inputs. One of the most studied control architectures in SFF is the Leader/Follower (L/F, also known as Chief/Deputy, Master/Slave and Target/Chaser) which uses a hierarchical arrangement such that one leader spacecraft is controlled to a reference orbit and the follower spacecraft control their relative states with respect to that leader (Alfriend et al., 2009; D'Errico, 2013; Scharf et al., 2004). This approach allows to control the orbit of the leader while the followers control only their relative state with respect to the leader. The follower tracks the natural dynamics of the reference orbit of the leader while only performing routine control with respect to the relative states of other elements of the formation and the leader. Another approach is the Virtual Structure (VS) in which the followers behave as a single, virtual, rigid body and its manoeuvers include rigid body motion and extensions/contractions (Alfriend et al., 2009; D'Errico, 2013; Scharf et al., 2004). Cyclic control architectures, although similar to L/F, are formed by connecting individual spacecraft controllers, however these controllers are not hierarchical. By allowing nonhierarchical connections between individual spacecraft controllers, cyclic algorithms can perform better than leader/follower algorithms and can distribute control effort more evenly (Alfriend et al., 2009; Ramirez-Riberos et al., 2010; Scharf et al., 2004). Behavioural architectures are combinations of MIMO, L/F and cyclic architectures. This type of control is based upon the idea that by adding control actions for individual behaviours, one obtains a part of each behaviour. In reference (Scharf et al., 2004) a behaviour is consider to be an objective such as collision-avoidance or tracking functions that the spacecraft must individually or collectively execute.

Each of the control architectures presented above has advantages and disadvantages (Alfriend et al., 2009; D'Errico, 2013; Scharf et al., 2004); MIMO architecture mostly guarantees optimality and stability even when a full state is not available and estimation must be carried out however, require a large amount of information which is a concern in terms of computational load and in general are not robust to local failures. On the other hand, L/F architectures are able to handle both of these concerns. The amount of information is reduced, since each follower only needs information about the leader and robustness is ensured in the case of possible leader failure by reassigning its follower to another leader. However, optimality is not guaranteed under this approach. Fuel balance problems may arise given that the leader, whose state is always located at the formation reference orbit, requires less control inputs than the followers. This mass imbalance produce differential drag which causes drift between the followers and the leader. The cyclic architecture is a middle-point between MIMO and L/F architectures. This approach may perform better than L/F architectures by allowing non-hierarchical connections, although their stability is poorly understood, but in many case may present high computational load as in MIMO architectures. According to (Scharf et al., 2004) and up to the knowledge of the author, there are no studies where rigorous stability conditions have been derived for cyclic architectures for spacecraft formation flying. However, there are studies in the field of robotics which can be taken into consideration for future stability proofs for this type of architecture in formation flying. The behavioural architecture combines the outputs of multiple controllers designed to achieve complex manoeuvring objectives, however it is possible for the behaviours to destructively interfere between each other and, in general terms, the only tool to verify that the combination of behaviours functions perform as desired is by implementing them in simulated scenarios.

1.4 Relevant Literature Survey on Spacecraft Formation Flying Control

The challenge of developing in-orbit autonomous control approaches to perform manoeuvring operations in spacecraft formation flying (SFF), such as formation keeping and reconfiguration in close-proximity, conducts to explore various essential requirements as presented in previous sections:

- Low-computational demands and the need for collision avoidance methods, while considering complicated dynamics and a large number of elements in the formation.
- Capacity to optimize fuel and overcome non-ideal conditions, uncertainties and changes in its environment.

In general terms, the research done in control of SFF has adopted a multidisciplinary profile and a large body of knowledge has been developed. Therefore, the purpose of this section is to address pertinent literature regarding the aforementioned requirements. In order to facilitate the presentation of this literature, the information has been divided in three categories: fuel optimisation and low computational resources, non-classic control and collision avoidance and nonlinear control.

1.4.1 Fuel Optimisation and Low Computational Resources

Regarding control schemes using linear optimisation with relative dynamics, one of the first work on the use of LQR for the control of spacecraft in formation was presented by Starin (Starin, 2001) using the Clohessy-Wiltshire (CW) (Clohessy and Wiltshire, 1960) model for circular reference orbits, in which an infinite time cost function was minimised by the algebraic Riccati equation. Bainum et al. (Bainum et al., 2005) presented further studies where the LQR was used along with the Tschauner and Hempel (TH) (Tschauner and Hempel, 1965) model for elliptic reference orbits. Following this same line of work, Capo-Lugo and Bainum (Capó-Lugo and Bainum, 2007) used the LQR and the TH model to maintain the separation distance between a pair of satellites for the NASA Benchmark Tetrahedron Constellation. This was accomplished while providing minimum time and fuel consumption through two different approaches, adapting the time-varying term in the TH equations in a piecewise manner and using the TH equations as a time-varying dynamical system.

In Bando et al. (Bando and Ichikawa, 2012), a formation flying problem is formulated using the TH equations as an output regulation problem for a periodic system. A feedback controller that assures asymptotic tracking and asymptotic disturbance rejection, while maintaining the closed-loop stability was developed making use of the Riccati procedure contained within the LQR theory. In Bae et al. (Bae and Kim, 2013), a formation pattern analysis is performed for the periodic relative motions between two spacecraft in arbitrary elliptic orbits. Pattern formations in the radial and along-track plane and in the along-track and cross-track plane are considered with respect to that of the leader spacecraft. Numerical simulation results show the formation pattern according to various eccentricities of the reference orbit. Results show the tendencies of the formation radius as a function of eccentricity of the leader, providing constraints and guideline to design the spacecraft formation pattern between two spacecraft in the elliptic orbits. Other strategies based on analytical procedures were also developed, for instance, Palmer (Palmer and Halsall, 2009) presented strategies to design satellite formations in near-circular low Earth orbits that exploit the dynamical features of an analytical model for the relative motion of satellites. The main objective of these strategies is to remove the need for station-keeping actuator control while including the principal oblateness disturbing effects of Earth. To do this, a set of orbital parameters is determined for each of the satellites, so that the natural dynamics will approximately maintain a formation geometry under J_2 and J_3 terms. Higher-order terms are then treated as a disturbance to the formation, which require a much smaller control thrust. Palmer also presented a general analytic formulation for optimal transfers for spacecraft formation flying based on the circular Hill's problem (Palmer, 2006). In this strategy, optimisation is performed to minimise the transfer energy required from the thruster. It is showed that this optimal control problem has simple analytic solutions that provide an effective way to develop formation control strategies. Yoo et al. (Yoo et al., 2013) presented fuel balancing strategies for manoeuvres between projected circular orbits, formulating the optimal control problem from Palmer's CW analytical solution (Palmer, 2006) for general configurations. Model predictive control was applied to formation flying in the work done by Breger and How (Breger et al., 2005), where a controller was designed using dynamics based on a modified version of Gauss variational equations and incorporating osculating J_2 effects. Additionally, an analytic model predictive controller for fuel-minimised, collision-free trajectory follower was developed in the work done in (Sauter and Palmer, 2012). The controller exploits the natural dynamics for relative tracking motion using minimal fuel consumption and minimal computational burden. The controller tracks a nominal trajectory even in the presence of disturbances and noise, while avoiding collisions with other members of the formation. In the work done by Hamel et al. (Hamel and Lafontaine, 2007) a geometric approach is used to develop an analytical state transition matrix that accurately models relative motion about elliptical reference orbits under J2 perturbation, while using simpler expressions and without the need to numerically propagate the states of the reference trajectory. This simplified model is oriented toward an on-board implementation for mission scenarios in which computational power is limited, such as low-cost scientific missions. Sengupta et al. (Sengupta et al., 2008), developed expressions for describing averaged relative motion between two satellites in neighboring orbits around an oblate planet and while assuming small relative distances between the satellites, the results are uniformly valid for all elliptic orbits as well as the special case of a circular reference orbit by the use of nonsingular orbital elements. These expressions were applied in the derivation of an analytical filter that removes short-periodic variations in relative states without the use of tuned numerical filters, one for each frequency of interest, which are normally used for disturbance accommodation in control system design. Later, the use of this analytical filter was demonstrated for formation keeping on a prescribed relative trajectory. In the work done by Xu et al.(Xu et al., 2012), a Hamiltonian structure-preserving controller is derived for the three-dimensional time-periodic system that models the J2-perturbed relative dynamics on a mean circular orbit. The unstable and stable manifolds are employed to change the hyperbolic equilibrium to elliptic one with the poles assigned on the imaginary axis. Detailed stability investigations are conducted on the critical controller gain for Floquet stability and the optimal gain for the fuel cost, respectively. These stability results show that any initial relative position and velocity leads to a bounded trajectory around the controlled elliptic equilibrium. Next, numerical simulations indicate that the controller effectively stabilizes motions relative to the perturbed elliptic orbit with small eccentricity and unperturbed elliptic orbit with arbitrary eccentricity. Following a similar research line as in the previous reference, Ming Xu et al. Xu et al. (2016) developed an extensive work on Hamiltonian structure-preserving control of cluster flight on an elliptic reference orbit is introduced, in order to yield bounded relative movement. The motions are stabilized around the natural relative trajectories rather than track a reference relative configuration. Moreover, the bounded quasi-periodic trajectories generated by the controller have advantages in rapid reconfiguration and unpredictable evolution. Works based on absolute dynamics of formations were also developed. In De Florio et al (De Florio et al., 2014) the problem of autonomous absolute orbit control is analysed as a specific case of the PRISMA mission using two spacecraft in formation affected by the non-spherical Earth gravitational field and atmospheric drag. For this purpose, a linear controller was implemented using velocity increments as control inputs by pole placement and LQR.

1.4.2 Non-Classic Control and Collision Avoidance

Control approaches may also include non-classic control strategies and reliable collision avoidance schemes (CAS) to safely handle the movement of the elements in the formation, particularly during proximity operations. Regarding control strategies, the concept of Coulomb spacecraft formation flying was thoroughly investigated by Schaub (Hogan and Schaub, 2012; Schaub, 2005; Schaub and Jasper, 2013; Schaub and Junkins, 2003; Schaub et al., 2004), where intervehicle active electrostatic forces were used in several instances to control close relative motion in a cluster using satellites with different masses and individual charge saturation limits. A similar control approach was used in Huang et al. (Huang et al., 2014) where controlled Lorentz forces were used on an electrostatically charged spacecraft as propellant-less electromagnetic propulsion for orbital manoeuvring in the planetary magnetic field. For this purpose, a closed-loop integral sliding mode controller was designed to effectively track a trajectory when external disturbances are also present. Additional novel control schemes, such as momentum exchange and differential drag, have been introduced. In the work done by Shestakov et al. (Shestakov et al., 2015) the concept of momentum exchange was applied to formation reconfiguration, drift stop, and also to relative motion trajectory maintenance under perturbation effect of J_2. Within this scheme, only one spacecraft, which is initially composed by the satellite body and a detachable mass, transfers the momentum. At command, the detachable mass separates from the satellite in a given direction with a given velocity. The separated mass moves to the other satellite and hits it absolutely inelastically while receiving impulse to its centre of mass. After the mass transfer, the resulting relative trajectory changes in an adjustable way. On the other hand, the concept of differential drag has also been introduced in several works. For example, Gurfil (Ben-Yaacov and Gurfil, 2013) presented differential drag based methods for long-term cluster keeping missions with multiple modules using orbital elements. The controller prove to be asymptotically stable and simulations show that the controller reduces the intersatellite distance significantly. Other interesting guidance and control approaches for formation flying included attractive/repulsive artificial potentials functions (APF), such as the ample work developed by McInnes (Badawy and McInnes, 2008, 2009; Lopez and McInnes, 1995; McInnes, 1993, 1995, 2007) where APF where used in a variety of cases to generate attractive and repulsive accelerations in order to control the reconfiguration manoeuvers, formation-keeping, on-orbit assembly and swarm behaviour of spacecraft. Following a similar line of work, Bennet and Suzuki (Bennet and McInnes, 2008, 2010; Suzuki et al., 2009) presented AFP schemes grounded in the theory of bifurcation to command the formation keeping of spacecraft and the transition during manoeuvring, providing a wide variety of configurations with only a single parameter change. Also, McCamish et al. (McCamish et al., 2007) investigated mixed control strategies, such as APF and LQR, to perform rendezvous and assembly manoeuvres using the CW relative dynamics.

1.4.3 Nonlinear Control

Additional control difficulties emerge when complicated nonlinear effects are included in the dynamics, inherent system uncertainties are contemplated and complicated mission constraints are imposed. To overcome these difficulties, several nonlinear control approaches have been proposed in literature, for example, interesting nonlinear control approaches have been developed in Mazal et al. (Mazal and Gurfil, 2013, 2014; Mazal et al., 2012, 2014) where a cluster-keeping control algorithm considering the effects of atmospheric drag and Earth oblateness was presented. For this purpose, an optimal guidance law with a cost function accounting for thruster throttle parameter and mass disposal was developed. Adaptive control has also been applied to formation flying. In this type of control method the resulting controller must adapt itself according to a dynamical system with varying or uncertain parameters. In the work presented by Queiroz et al. (De Queiroz et al., 2000) a Lyapunov-based nonlinear controller was developed guaranteeing global asymptotic convergence of the spacecraft relative position to any desired trajectory, despite the presence of unknown, constant, or slow-varying spacecraft masses and disturbance forces. Pan and Kapila (Pan and Kapila, 2001) developed an adaptive controller using coupled relative translational and attitude motion and a Lyapunov framework that ensures global asymptotic convergence despite the presence of unknown spacecraft mass and inertia parameters.

Intelligent control has also played a role in formation flying control, for instance, adaptive neural control applied to the problem of deep-space spacecraft formation flying was proposed by in Gurfil et al. (Gurfil et al., 2003) in order to control a formation while compensating for deep-space disturbances such as solar radiation pressure and fourth-body gravitation. For this purpose, the relative dynamics was modelled using highly nonlinear dynamics obtained from the Circular Restricted Three Body Problem with the Sun and the Earth as the primary gravitational bodies. While translational dynamics has been widely investigated in SFF, attitude dynamics has received less interest. In this regard, a control scheme for formation flying in six-degrees-of-freedom has been proposed in Lee et al. (Lee et al., 2015) where a decentralised tracking control scheme using Lie group theory and a Lennard-Jones potential for collision avoidance was developed. The simulated scenarios use a virtual leader approach[1] and focus on formation keeping using highly elliptical reference orbits, leading to almost global asymptotic convergence to the desired trajectory. In the work done in Gurfil (Segal and Gurfil, 2009) it was showed that 6 degrees-of-freedom rigid-body spacecraft relative motion must be obtained by combining the relative translational and rotational dynamics of arbitrary points on the spacecraft. When these points were not located at the spacecraft centre of mass, a kinematic coupling between the rotational and translational dynamics was generated. The objective of this work was to quantify the kinematic coupling effect of the translation and rotation dynamics and to show that this feature is essential to high-precision modelling of tight formation flying, rendezvous, and docking.

1.5 Current Spacecraft Formation Flying Missions

Given its mission objectives, practical applications, design parameters, mission constraints and manoeuvring features, most of the work presented in this thesis is influenced by the missions TanDEM-X (TerraSAR-X add-on for Digital Elevation Measurement) (Montenbruck and Kahle, 2008), the mission Prototype Research Instruments and Space Mission Technology Advancement (PRISMA) (D'Amico et al., 2013) and PROBA-3 (Peters et al., 2014). This chapter provides an overview of these missions, including their objectives and contributions to the development of SFF technology.

---

[1] In spacecraft formation flying, a virtual leader means that the centre of the formation is vacant.

1.5.1 TanDEM-X Autonomous Formation Flying System

TanDEM-X (Montenbruck and Kahle, 2008) is the first configurable SAR interferometer mission employing formation flying and it comprises two nearly identical spacecraft, named TSX and TDX as show in Fig. (1.1), which have a size of 5 m × 2.4 m, a mass of 1200 kg and carry a high-resolution synthetic aperture radar (SAR) operating in the $X-$band (9.65 GHz). TSX has been launched by a DNEPR rocket on June 15, 2007 and was injected into a 514 km sun-synchronous dusk-dawn orbit with 97° inclination. TDX was launched later on June 21, 2010. The main objective of TanDEM-X mission is to generate a global digital elevation model (DEM)[2] with high accuracy in order to assist in a wide variety of scientific research as well as for commercial DEM production. In order to collect sufficient measurements for a global DEM, three years of formation flying experiments were executed using different across-track baselines ranging from 150 m to few kilometres (Ardaens et al., 2014).

Fig. 1.1 TanDEM-X mission. Courtesy of DLR

After DEM acquisitions, SAR applications with more demanding formation control performance will be required. For this purpose, TanDEM-X formation is equipped with an onboard autonomous formation keeping control system, called TanDEM-X Autonomous Formation Flying (TAFF). Two closed-loop in-flight experiments have been carried out to evaluate its functional behavior and control

---

[2] A 3D representation of a terrain's surface

performance. The first experiment campaign was conducted in March 2011 demonstrating TAFF abilities to maintain formation, however, the experiments presented problems due to GPS receivers degradation. After fixing this problem, a second experiment campaign was conducted one year later, in order to evaluate formation keeping and baseline reconfiguration.

Several constraint were imposed to TAFF campaign of experiments, for example, the system was not allowed to thrust during the acquisition of SAR images, a deterministic control scheme was required to facilitate the planning of operations and a low computational load to compensate for the limited on-board resources. TAFF navigation and control algorithms are based on a special state parameterisation using the relative orbital elements $a\delta a$, $a\delta\boldsymbol{e} = \begin{bmatrix} a\delta e_x & a\delta e_y \end{bmatrix}^T$, $a\delta\boldsymbol{i} = \begin{bmatrix} a\delta i_x & a\delta i_y \end{bmatrix}^T$ and $a\delta\lambda$ built upon the Clohessy-Wiltshire (Clohessy and Wiltshire, 1960) model and denoted respectively as the relative semi-major axis, the relative eccentricity vector, the relative inclination vector and the relative mean longitude between spacecraft. Additionally, TAFF performs an estimation the six relative orbit elements using a procedure based in a Kalman Filter (Ardaens et al., 2014; Montenbruck and Kahle, 2008).

TAFF second campaign of experiments was divided in open-loop and closed-loop performance. The objective of using an open-loop mode, using only the dynamical features of the initial state, was to observe the performance of the TAFF without control inputs. Once sufficient confidence was built on its performance, TAFF was set in closed-loop mode for 12 days, executing autonomously a total of 88 formation keeping and reconfiguration manoeuvers. The main goal on these manoeuvers was to observe TAFF performance changing formation baseline on a daily basis and to verify how fast a reconfiguration could be done.

According to reference (Ardaens et al., 2014), TAFF relative control performance during the second experiment campaign was finer than ±10m, which demonstrates that substantially increased performances can be achieved when the controller is implemented on-board rather than on-ground. Moreover, TAFF was shown to be operationally robust, easy to operate and fully predictable.

1.5.2 PRISMA Mission

PRISMA, a mission designed by the Swedish National Space Board and OHB Sweden, had the objective of testing spacecraft formation flying technologies and capabilities for future space missions

(D'Amico et al., 2012). This mission comprises a follower called Mango, which has full manoeuvrability with its 3-axis stabilisation and full 3D Δv manoeuvrability independent of the spacecraft attitude. This spacecraft is equipped with three propulsion systems, where the main system, a hydrazine propulsion system with 6×1 N thrusters, has approximately 120 m/s Δv capability. On the other hand, the leader spacecraft is called Tango and it has a $3-$axis stabilising, magnetic attitude control system and no orbit manoeuvre capability. Both spacecraft can be observed in Fig. (1.2). Tango follows a reference dusk-dawn orbit with a mean altitude of 757 km, an eccentricity of 0.004 and an inclination of 98.28°. Further physical aspects of these two spacecraft can be observed in Table (1.1).

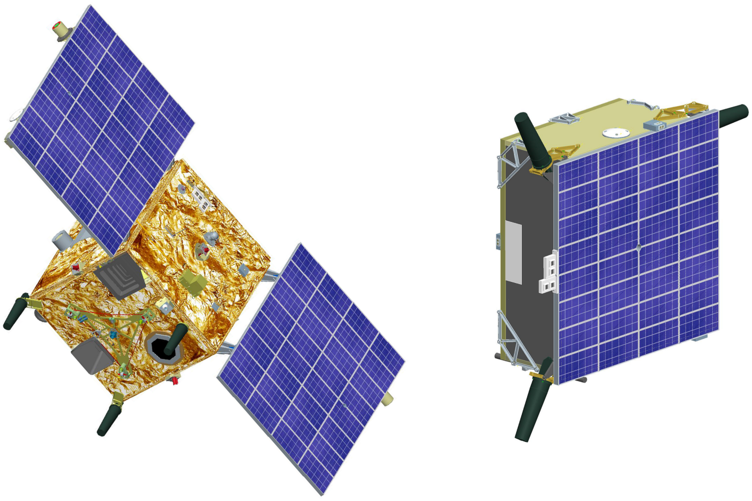

Fig. 1.2 Mango and Tango satellites from PRISMA mission. Courtesy of DLR

Table 1.1 Summary of relevant physical features of Mango and Tango

	MANGO 1	**MANGO 2**
Main Body (mm)	$750 \times 750 \times 820$	$570 \times 740 \times 295$
Deployed (mm)	2600	N/A
Wet Mass (kg)	150	40
Propulsion (N)	6×1 ($I_{sp} = 220$ s)[b]	N/A
Cross Section (m^2)	1.3 or 2.75[a]	0.38
Drag Coefficient	2.5	2.25

[a] After solar panels are deployed

[b] Approximately 5.6 kg of fuel and 60 m/s of Δv per mission

Within this mission, the German Aerospace Centre (DLR) and the German Space Operations Centre (GSOC) contribute with the Spaceborne Autonomous Formation Flying Experiment (SAFE) and the on-board Autonomous Orbit Keeping (AOK) for one follower. These experiment represent one of the first demonstrations of a complete guidance, navigation and control subsystem for spacecraft formation flying in low Earth orbit. The objectives of these experiments include (D'Amico et al., 2013):

- To provide GPS navigation data of both Mango and Tango
- To provide, on Mango, precise absolute/relative orbit solution for the formation
- To implement a guidance law for safe collision-free separation strategies
- To provide a robust control algorithm for formation keeping and reconfiguration
- To demonstrate autonomous orbit control of close formations
- To implement an automated on-ground process for precise orbit reconstruction

The flight control module software, called AFC in (D'Amico et al., 2013), estimates the state of the two satellites using GPS-based navigation with an Extended Kalman Filter (EKF). Each of the experiments included in SAFE were executed with the AFC in three different modes: without control inputs, in open loop (computed using only its current state and the model) and finally in closed-loop. During the first days of the experiments, the AFC was operated using the first two modes in order to verify its basic performance. During these experiments, the formation drifted under the influence of the initial relative state conditions, differential gravity and differential drag. Once enough confidence in the AFC performance was gained, the closed-loop mode entered in operation for the rest of the experiments. The geometries explored during SAFE can be observed in detail in Table (1.2) (D'Amico et al., 2013).

In the formation A it is required that $a\delta e_x = a\delta i_x = 0$ and stop the mean along-track drift at $a\delta\lambda = 1882.3$ m using the error feedback accumulated during the free motion phase. Formation B has the objective of demonstrating autonomous rendezvous by making $a\delta\lambda = 0$ m. Experiments from C to F demonstrate stepwise and simultaneous corrections of non-parallel $a\delta\boldsymbol{e}$ and $a\delta\boldsymbol{i}$ with a reduction of their amplitudes to a minimum of 200 m and enclosed angle of 60°, respectively. Finally,

Table 1.2 Summary of Formation Flying experiments in PRISMA mission (D'Amico et al., 2013)

Length (days)	**AFC Mode**	**Formation ID**	$a\delta a$ (m)	$a\delta\lambda$ (m)	$a\delta e_x$ (m)	$a\delta e_y$ (m)	$a\delta i_x$ (m)	$a\delta i_y$ (m)
1	G	Initial state	-0.5	-25	-10	405	-6	298
2	OL	Final state	5	1882.5	55	397	-7	296
2	CL (along-track)	A	0		0	400	0	300
1	CL (radial)	B						
2								
3		C					150	259.8
3		D				300		
1		E				250	125	216.5
1		F				200	100	173.2

G = Guidance
OL = Open-loop
CL = Closed-loop

the geometry defined in F corresponds to a minimum separation distance between Mango and Tango of 150 m (D'Amico et al., 2013; De Florio et al., 2013).

1.5.3 PROBA-3 Mission

The Project for Onboard Autonomy 3 (PROBA-3) (Peters et al., 2014) is a space mission from the European Space Agency (ESA) dealing with precise formation flying. The mission, to be launched in 2018, will demonstrate formation flying technology within a large-scale coronagraph study for a period of two years where two spacecraft, the Coronagraph and the Occulter as in Fig. (1.3), will perform as a virtual structure maintaining high-precision formation autonomously at baselines distances of 150 m or more.

The Coronagraph has a mass of 340 kg and a volume of 1100 × 1800 × 1700 mm^3 and it hosts the coronagraph instrument to observe the corona of the sun. Its guidance, navigation and control (GNC) system consists of four reaction wheels, 2 × 3 axis gyroscopes, one three-headed star tracker, six Sun sensors and two GPS receivers. Moreover, most of the formation flying modules are contained within this spacecraft. The second spacecraft, the Occulter, has a mass of 200 kg and a volume of 900 × 1400 × 900 mm^3 and its main task is to block the sun in such way that only the light of the Sun's corona enters into the coronagraph instrument (forming an artificial eclipse in space). Its GNC system consists of 4 reaction wheels, 3 three-axis gyroscopes one triple-headed star tracker, six Sun sensors and two GPS receivers. A summary of relevant physical attributes of the spacecraft can be found in Table (1.3). The reference orbit for the mission will be a highly elliptical orbit with a size of 600 × 60530 km and orbital parameters as shown in Table (1.4).

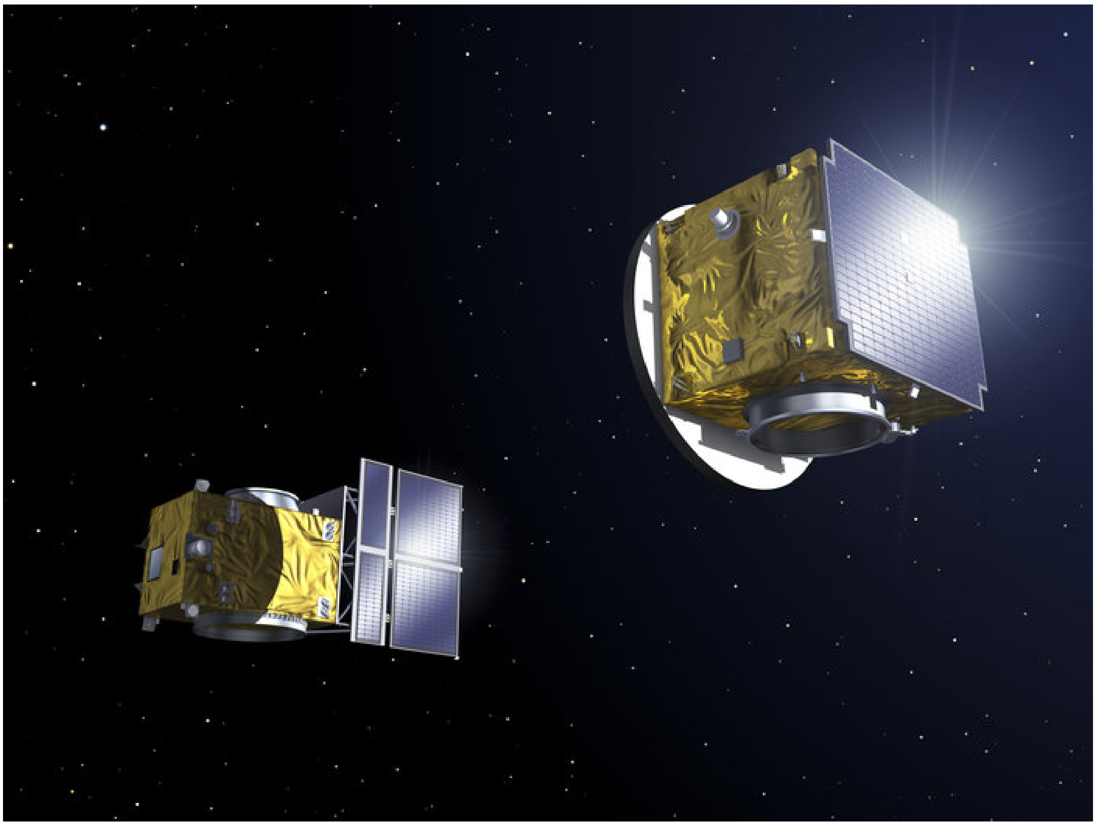

Fig. 1.3 Proba-3 Formation Flying. Courtesy of ESA

Table 1.3 Summary of relevant physical features of the Coronagraph and Occulter

PARAMETER	**OCCULTER**	**CORONAGRAPH**
Area (m^2)	1.77	3.34
Wet Mass (kg)	211	339
Dry Mass (kg)	190	327
SRP Coefficient	1.9	1.29
Thrust per thruster (mN)	10	1000
Specific Impulse (s)	68	235

SRP = solar radiation pressure

Table 1.4 Summary of relevant physical features of the Coronagraph and Occulter

PARAMETER	**VALUE**
Perigee height	600 km
Apogee height	60,530 km
Semimajor axis	36,943 km
Eccentricity	0.811
Inclination	59°
RAAN	84°
AoP	188°
Orbital Period	19h 38m

RAAN = Right Ascension of Ascending Node
AoP = Argument of Perigee

Table 1.5 Summary of Δv values obtained in PROBA-3 mission experiments

MANOEUVER	**Δv (m/s)**
Apogee formation keeping	7.29
Rigid resizing	77.5
Rigid retargeting	62.6

Successful mission performance will require to move the Occulter far away from the Coronagraph while still preserving eclipse-like conditions for long periods of time. For this purpose, several formation flying experiments have been presented in (Peters et al., 2014) and (Ardaens et al., 2013) in order to demonstrate acquisition, rendezvous, proximity operations, formation flying, coronagraph operations, separation and convoy flying every orbit with minimal ground control intervention. For example, in reference (Peters et al., 2014), the objective of the formation flying analysis is to provide a feasible operational sequence and the Δv required. The nominal orbit consists of a forced motion apogee pass, including the formation manoeuvers around apogee, a formation break up, a free-flying perigee pass and formation acquisition. In this work, a linearised model is used for the propagation of the relative motion and for manoeuver computation, including the effects of perturbations like J_2, third-body, air drag and solar radiation pressure. The manoeuvers consist of deployment, formation keeping for coronagraph experiments, rigid resizing and rigid retargeting. The selected strategy required the values of Δv presented in Table (1.5).

1.6 Thesis Objectives and Contributions

In previous sections it was observed that there is a need to develop new control schemes in spacecraft formation flying (SFF) to overcome problems such as in-orbit high-computing demand, collision avoidance capabilities and capacity to deal with nonlinear effects. In order to present novel solutions to these problems, the objective of this thesis is to introduce new control methods to allow spacecraft in formation, with circular/elliptical reference orbits, to efficiently execute safe autonomous manoeuvres. These controllers distinguish from the bulk of literature in that they merge guidance laws never applied before to SFF and collision avoidance capacities into a single control strategy. These control strategies are summarized as follow:

- Linear optimal tracking control and collision avoidance capabilities. See Chapter 3.
- Forward-in-time, state estimator based in the separation principle and collision avoidance capabilities. This controller also has the capacity to deal with incomplete measurements of the states of the spacecraft. See Chapter 4.
- Immersion and Invariance based nonlinear adaptive control and collision avoidance capabilities. This controller also has the capacity to deal with orbital perturbations, such as J2 and atmospheric drag. See Chapter 5.

A Leader/Follower (L/F) architecture is selected for the design of the controllers. Devising control strategies using L/F architectures will allow the designer to control the relative state of the follower with respect to the leader, while providing more insight into how the desired relative geometry is specified. Moreover, in order to account for fuel imbalance, a virtual leader (a vacant formation centre) may be used. In general terms, the proposed control approaches command the dynamical performance of one or several followers with respect to a leader to asymptotically track a time-varying nominal trajectory, while the threat of collision between the followers is reduced by repelling accelerations obtained from the collision avoidance scheme during the periods of closest proximity. The range of practical applications of these control schemes may include educational purposes, its implementation in software and hardware-in-the-loop simulations for initial and formal mission assessment, implementation as the actual in-orbit controller, among others.

1.7 Thesis Structure

This thesis is composed by 6 chapters, each one of them self-contained in terms of notation as noticed in the Nomenclature section. After the introduction in Chapter 1, this thesis starts with Chapter 2 where the equations of relative motions are derived, considering the spacecraft as point masses. First the required reference frames and the equations for the nonlinear relative translational motion are obtained. Following these two sections, a linearised version of the relative translational equations of motions is also presented followed by its state-space representation. This chapter additionally introduces expressions for the external perturbations usually found in low-Earth orbits, which include the effects of the oblateness of the Earth and atmospheric drag.

In Chapter 3, a Riccati-based tracking controller is presented. Within this control strategy, the controller will provide guidance and tracking toward a desired time-varying nominal trajectory (TVNT), optimising fuel consumption by Riccati procedure using a non-infinite cost function in terms of the desired TVNT. An important aspect of this thesis is to present a collision avoidance scheme (CAS) to enable spacecraft in formation to autonomously avoid collisions. To this end, the theory regarding artificial potential functions for collision avoidance schemes is also presented, where repelling accelerations are obtained from the negative gradient of a Gaussian-like potential function, which accounts for variable position of both the spacecraft and the obstacle. The repelling accelerations generated from the CAS will ensure evasive actions between the elements of the formation. The relative dynamics, suitable for circular and eccentric low-Earth reference orbits, is accounted by a linear system based in the Tschauner and Hempel equations.

A controller using a state estimator built on the forward-in-time separation principle is presented in Chapter 4. This proposed controller involves two stages: regulation and estimation. The first stage requires the design of a full state feedback controller using the state vector reconstructed by means of the estimator. The second stage requires the design of an additional dynamical system, called the estimator, to obtain the states which cannot be measured in order to approximately reconstruct the full state vector. The separation principle states that an observer built for a known input can also be used to estimate the state of the system and then, to generate the control input. This allows to design the observer and the feedback independently, by exploiting the advantages of linear quadratic regulator theory, in order to estimate the states of a dynamical system with model and sensor uncertainty. The relative dynamics is described with the linear system used in the previous controller, with nonlinearities entering via the repelling accelerations from the CAS during collision avoidance events and sensor uncertainty is added by considering carrier-phase differential GPS (CDGPS) velocity measurement error.

In Chapter 5, an adaptive control law capable of delivering superior closed-loop performance when compared to the certainty-equivalence (CE) adaptive controllers is designed. A novel uncertainty-equivalence controller based on Immersion and Invariance paradigm is introduced for close-manoeuvring spacecraft formation flying in both circular and elliptical low-Earth reference orbits. This controller commands the nonlinear dynamical performance of one or several followers with respect to a leader, by asymptotically tracking a TVNT, while uncertainty in the modelling of perturbation forces is present and collision between the followers is avoided using the CAS. The proposed control scheme achieves stabilisation by immersing the plant dynamics into a target dynamical system (or a manifold) that captures the desired dynamical behaviour. They key feature of this methodology is the addition of a new term to the classical certainty-equivalence control approach that, in conjunction with the parameter update law, is designed to achieve adaptive stabilisation. This parameter has the task of shaping the manifold into which the adaptive system is immersed. The performance of the controller is proven stable via a Lyapunov-based analysis and Barbalat's lema.

In order to validate the design of the controllers, test cases based on the physical and orbital features of the Prototype Research Instruments and Space Mission Technology Advancement (PRISMA) will be implemented at the end of Chapters 3, 4 and 5 extending the number of elements in the formation into scenarios with reconfigurations and on-orbit position switching in elliptical low-Earth reference orbits. An extensive analysis and comparison of the performance of the controllers in terms of total Δv and fuel consumption, with and without the effects of the CAS, is also presented. Finally, the thesis concludes with Chapter 6 where conclusions and some recommendations for future research in autonomous control of formation flying are presented.

1.8 Thesis Outputs

The following section presents a list containing all the journal and conference papers that have been obtained from the present work and a list with thesis contributions.

1. **Journal Publications**

    (a) L. Palacios, G. Radice, A. Misra, *Formation Flying via Immersion and Invariance: an Adaptive Control Approach for Close Manoeuvring Spacecraft through Attracting-Manifold Design*, Acta Astronautica, 2015, In revision. This paper corresponds to the work presented in Chapter 5.

    (b) L. Palacios, M. Ceriotti, G. Radice, *Close Manoeuvring Spacecraft Formation Flying Control via State Estimation and Artificial Potential Functions*, The Journal of the Astronautical Sciences, 2015, In revision This paper corresponds to the work presented in Chapter 4.

    (c) L. Palacios, M. Ceriotti, G. Radice, *Close proximity formation flying via linear quadratic tracking controller and artificial potential function*, Advances in Space Research, Vol. 56, Issue 10, 2015. This paper corresponds to the work presented in Chapter 3.

2. **Conference Publications**

    (a) L. Palacios, G. Radice, A. Misra, *Formation Flying via Immersion and Invariance: an Adaptive Control Approach for Close Manoeuvring Spacecraft through Attracting-Manifold Design*, 8th International Workshop on Satellite Constellations and Formation Flying Delft, Netherlands, 2015. This paper corresponds to the work presented in Chapter 5.

    (b) L. Palacios, M. Ceriotti, G. Radice, *State estimation for spacecraft formation flying based on the separation principle*, 65th International Astronautical Congress Toronto, Canada, 2014. This paper corresponds to the work presented in Chapter 4.

    (c) L. Palacios, M. Ceriotti, G. Radice, *Autonomous distributed LQR/APF control algorithms for CubeSat swarms manoeuvring in eccentric orbits*, 64th International Astronautical Congress Beijing, China, 2013. This paper corresponds to the work presented in Chapter 3.

    (d) L. Palacios, Y. Sugimoto, A. Lawal, G. Radice, *A Robust Near-Earth Asteroid Mitigation Campaign of Multiple Formation Flying Gravity Tractors*, 64th International Astronautical Congress Beijing, China, 2013. This paper corresponds to the work presented in Chapter 2 and 3.

(e) L. Palacios, M. Ceriotti, G. Radice, *Electromagnetic Formation Flying with Eccentric Reference Orbits*, 7th International Workshop on Satellite Constellations and Formation Flying Lisbon, Portugal, 2013

The control strategies presented in Subsection 1.6 represent the main contributions of this thesis. These contributions represent approaches never applied before in formation flying and are summarized as follow:

- Development of a linear optimal tracking control of spacecraft in formation with circular/elliptical reference orbits and collision avoidance capabilities from a Gaussian potential. See Chapter 3 and paper 1(c), 2(c) and 2(d).
- Design of a forward-in-time state estimator based in the mathematical framework developed in (Damak et al., 2013), applied to spacecraft formations with circular/elliptical reference orbits and collision avoidance capabilities from a Gaussian potential. This controller also has the capacity to deal with incomplete measurements of the states of the spacecraft. See Chapter 4 and paper 1(b) and 2(b).
- Development of a nonlinear adaptive control based in the mathematical framework Immersion and Invariance as in (Astolfi et al., 2008a; Seo and Akella, 2008), applied to spacecraft in formation with circular/elliptical reference orbits and collision avoidance capabilities from a Gaussian potential. This controller also has the capacity to deal with orbital perturbations, such as J2 and atmospheric drag. See Chapter 5 and paper 1(a) and 2(c).

Chapter 2

Equations of Motion

In this chapter, the equations of motion describing the dynamics of spacecraft orbiting in formations are presented. The chapter is divided in five sections and starts by introducing the reference frames required for the derivation of the equations. Next, the nonlinear equations describing the relative motion of the follower with respect to the leader (or the centre of the formation in case a virtual leader is considered) are presented. The chapter continues with the sections corresponding to the linearisation of the nonlinear equations of motion around eccentric reference orbits and its state-space representation and the external perturbations considered in the test cases presented in this thesis. As an additional note, the equations of motion are usually rescaled and/or non-dimensionalised for simulation purposes. This is done to reduce the number of variables, in order to analyse the behaviour of the system regardless of the units used to measure the variables, and to rescale the parameters and variables so that all computed quantities are of relatively similar magnitudes. Additionally, the equations presented in this chapter can also be formulated using other tools from classical mechanics, for example, using Lagrangian (Wong et al., 2002), Hamiltonian (Kasdin et al., 2005; Xu et al., 2012) or Kane dynamics (Kane et al., 1983), among others.

2.1 Reference Frames

Three coordinate systems are of interest for this work: the Earth-centred inertial denoted as $\mathcal{I}$, the Local-Vertical-Local-Horizontal frame denoted by $\mathcal{L}$ and the body-fixed reference frame denoted by $\mathcal{B}$. The reference frame $\mathcal{I}$ is defined by the set of orthonormal right-handed unit base vectors

$\left\{ \mathbf{i_1} \quad \mathbf{i_2} \quad \mathbf{i_3} \right\}$ and is fixed to the Earth. The unit vector $\mathbf{i_1}$ is directed from the Earth centre to the vernal equinox, the $\mathbf{i_1} - \mathbf{i_2}$ plane is the Earth's equatorial plane and the unit vector $\mathbf{i_3}$ is directed along the Earth's axis of rotation. The reference frame $\mathcal{L}$ is defined by the set of orthonormal right-handed unit base vectors $\left\{ \mathbf{l_1} \quad \mathbf{l_2} \quad \mathbf{l_3} \right\}$. In order to define this frame, consider two spacecraft, one called the leader (L) and the other called the follower (F). The $\mathcal{L}$ frame is rotating with a, possibly time-varying, angular velocity $\boldsymbol{\omega} \in \mathbb{R}^3$ with respect to the origin and attached to L with the same plane as the orbital plane. The unit vector $\mathbf{l_1}$ is directed radially outward from this spacecraft, $\mathbf{l_3}$ is normal to the fundamental plane and $\mathbf{l_2}$ completes the triad. The reference frame $\mathcal{B}$ is defined by the set of orthonormal right-handed unit base vectors $\left\{ \mathbf{b_1} \quad \mathbf{b_2} \quad \mathbf{b_3} \right\}$ fixed to F and parallel to its principal axes of inertia. The relative position between the three coordinate systems is illustrated in Fig. 2.1.

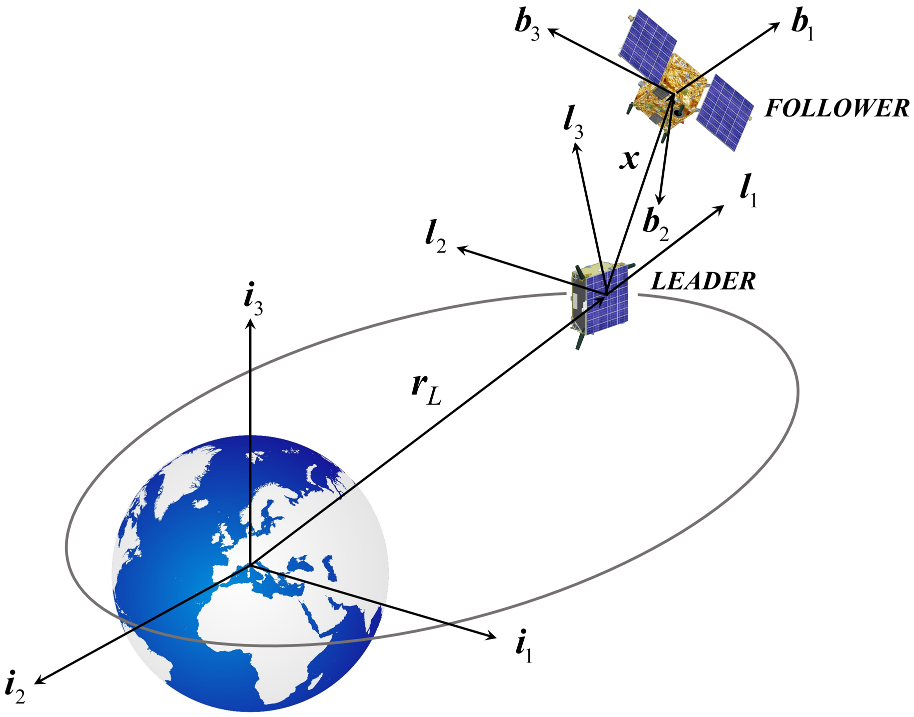

Fig. 2.1 Reference frames

2.2 The Equations of Relative Motion

Consider the leader and the follower spacecraft as point masses and assume the leader is following a reference Keplerian low Earth orbit. The translational equations of a follower spacecraft subjected to the action of the gravity force, external disturbances and control forces are presented according to reference (Alfriend et al., 2009). Consider first the equation of motion of the leader in the $\mathcal{I}$ frame, which is denoted as:

$$\ddot{\boldsymbol{r}}_L = -\frac{\mu}{\|\boldsymbol{r}_L\|^3}\boldsymbol{r}_L \tag{2.1}$$

In similar way, the equation of motion of the follower in the $\mathcal{I}$ frame is defined as:

$$\ddot{\boldsymbol{r}}_F = -\frac{\mu}{\|\boldsymbol{r}_F\|^3}\boldsymbol{r}_F \tag{2.2}$$

where the operator $\| \quad \|$ denotes the 2-norm of a vector or Euclidean norm, $\boldsymbol{r}_L \in \mathbb{R}^3$ is the orbital position vector of the leader, $\boldsymbol{r}_F \in \mathbb{R}^3$ is the orbital position vector of the follower and $\mu \in \mathbb{R}$ is the gravitational constant. Next, the relative position of the follower with respect to the leader is denoted by:

$$\boldsymbol{\varrho} = \boldsymbol{r}_F - \boldsymbol{r}_L \tag{2.3}$$

Therefore, subtracting Eq. (2.1) from Eq. (2.2) yields the expression:

$$\ddot{\boldsymbol{\varrho}} = -\frac{\mu\left(\boldsymbol{r}_L + \boldsymbol{\varrho}\right)}{\|\boldsymbol{r}_L + \boldsymbol{\varrho}\|^3} + \frac{\mu}{\|\boldsymbol{r}_L\|^3}\boldsymbol{r}_L \tag{2.4}$$

The absolute acceleration of the follower relative to the leader can be expressed using the relationship:

$$\ddot{\boldsymbol{\varrho}}^{\mathcal{L}} + 2\boldsymbol{\omega} \times \dot{\boldsymbol{\varrho}}^{\mathcal{L}} + \dot{\boldsymbol{\omega}} \times \boldsymbol{\varrho} + \boldsymbol{\omega} \times \left(\boldsymbol{\omega} \times \boldsymbol{\varrho}\right) = -\frac{\mu\left(\boldsymbol{r}_L + \boldsymbol{\varrho}\right)}{\|\boldsymbol{r}_L + \boldsymbol{\varrho}\|^3} + \frac{\mu}{\|\boldsymbol{r}_L\|^3}\boldsymbol{r}_L \tag{2.5}$$

where the superscript $\mathcal{L}$ means the derivation has been made with respect to the reference frame $\mathcal{L}$. After defining the vectors $\boldsymbol{\omega} = \begin{bmatrix} 0 & 0 & \dot{\theta} \end{bmatrix}^T$ in the $\mathcal{I}$ frame and $\boldsymbol{r}_L = \begin{bmatrix} r & 0 & 0 \end{bmatrix}^T$ and $\boldsymbol{\varrho} = \begin{bmatrix} x & y & z \end{bmatrix}^T$ in the $\mathcal{L}$ frame, Eq.(2.5) can be expressed in component-wise manner, including control and perturbation accelerations, as:

$$\ddot{x} - 2\dot{\theta}\dot{y} - \ddot{\theta}y - \dot{\theta}^2 x = -\frac{\mu\left(r + x\right)}{\left[\left(r + x\right)^2 + y^2 + z^2\right]^{3/2}} + \frac{\mu}{r^2} + a_x + u_x \tag{2.6}$$

$$\ddot{y} + 2\dot{\theta}\dot{x} + \ddot{\theta}x - \dot{\theta}^2 y = -\frac{\mu y}{\left[\left(r + x\right)^2 + y^2 + z^2\right]^{3/2}} + a_y + u_y \tag{2.7}$$

$$\ddot{z} = -\frac{\mu z}{\left[\left(r + x\right)^2 + y^2 + z^2\right]^{3/2}} + a_z + u_z \tag{2.8}$$

where the coordinates x, y, z correspond to the relative position of the follower, the terms r and θ are the position vector and the true anomaly of the reference orbit respectively, and the terms a_x, a_y, a_z and u_x, u_y, u_z are the sum of all perturbation and control accelerations, respectively. Equations (2.6), (2.7) and (2.8) together with the acceleration along the radial and tangential direction (Alfriend et al., 2009; Battin, 1999):

$$\ddot{r} = r\dot{\theta}^2 - \frac{\mu}{r^2} \tag{2.9}$$

$$\ddot{\theta} = -\frac{2\dot{r}\dot{\theta}}{r} \tag{2.10}$$

comprise a 10th order nonlinear system of differential equations.

2.3 Linearised Translational Relative Dynamics

With the assumption that $\|\boldsymbol{\varrho}\| \ll r$ the translational dynamics represented in Eq. (2.4) can be linearised around the formation centre to give (Alfriend et al., 2009):

$$\ddot{\boldsymbol{\varrho}} = -\frac{\mu}{\|\boldsymbol{r}_L\|^3}\left(\boldsymbol{\varrho} - \frac{3\boldsymbol{r}_L \cdot \boldsymbol{\varrho}}{\|\boldsymbol{r}_L\|^2}\boldsymbol{r}_L\right) \tag{2.11}$$

Combining the left side of Eq. (2.5) or (2.6 - 2.8) with Eq. (2.11) and the fundamental equations of orbital mechanics (for the unperturbed case) (Battin, 1999):

$$r = \frac{a\left(1 - e^2\right)}{1 + e\cos\theta} \tag{2.12}$$

$$\dot{\theta} = \frac{n\left(1 + e\cos\theta\right)^2}{\left(1 - e^2\right)^{3/2}} \tag{2.13}$$

where e is the eccentricity of the orbit and a its semi-major axis, and the natural frequency of the reference orbit is defined as:

$$n = \left(\frac{\mu}{a^3}\right)^{1/2} \tag{2.14}$$

then, the linearised translational equations of the relative dynamics for both circular and eccentric reference orbits are obtained as (Inalhan et al., 2002):

$$\ddot{x} - 2\dot{\theta}\dot{y} - \ddot{\theta}y - \dot{\theta}^2 x = 2n^2 \left(\frac{1 + e\cos\theta}{1 - e^2}\right)^3 x \tag{2.15}$$

$$\ddot{y} + 2\dot{\theta}\dot{x} + \ddot{\theta}x - \dot{\theta}^2 y = -n^2 \left(\frac{1 + e\cos\theta}{1 - e^2}\right)^3 y \tag{2.16}$$

$$\ddot{z} = -n^2 \left(\frac{1 + e\cos\theta}{1 - e^2}\right)^3 z \tag{2.17}$$

The term $\dot{\theta} \in \mathbb{R}$ is defined as in Eq. (2.13) and $\ddot{\theta} \in \mathbb{R}$ can be obtained using the equation (Battin, 1999):

$$\ddot{\theta} = -\frac{2en\sin\theta\dot{\theta}}{\left(1 - e^2\right)^{3/2}} \left(e\cos\theta + 1\right) \tag{2.18}$$

Equations (2.15) to (2.17) may be arranged in vector-matrix representation. It is also noticed that the subscript L has been dropped for clarity. If additional terms corresponding to the external perturbations $\boldsymbol{a}(t) \in \mathbb{R}^3$ and control input $\boldsymbol{u}(t) \in \mathbb{R}^3$ are included as, while assuming Eq.(2.13) and (2.18) are still valid, then Eq.(2.6 - 2.8), this set of equations can be expressed as:

$$\begin{aligned} \frac{d}{dt}\begin{bmatrix} \dot{x} \\ \dot{y} \\ \dot{z} \end{bmatrix} = & -2\begin{bmatrix} 0 & -\dot{\theta} & 0 \\ \dot{\theta} & 0 & 0 \\ 0 & 0 & 0 \end{bmatrix}\begin{bmatrix} \dot{x} \\ \dot{y} \\ \dot{z} \end{bmatrix} - \begin{bmatrix} -\dot{\theta}^2 & 0 & 0 \\ 0 & -\dot{\theta}^2 & 0 \\ 0 & 0 & 0 \end{bmatrix}\begin{bmatrix} x \\ y \\ z \end{bmatrix} \\ & - \begin{bmatrix} 0 & -\ddot{\theta} & 0 \\ \ddot{\theta} & 0 & 0 \\ 0 & 0 & 0 \end{bmatrix}\begin{bmatrix} x \\ y \\ z \end{bmatrix} + n^2 \left(\frac{1 + e\cos\theta}{1 - e^2}\right)^3 \begin{bmatrix} 2x \\ -y \\ -z \end{bmatrix} \\ & + \begin{bmatrix} a_x \\ a_y \\ a_z \end{bmatrix} + \begin{bmatrix} u_x \\ u_y \\ u_z \end{bmatrix} \end{aligned} \tag{2.19}$$

The terms on the right-hand side of this equation correspond to Coriolis acceleration, centripetal acceleration, angular acceleration, and the virtual gravity gradient terms with respect to the formation reference (Gurfil, 2003). In compact-matrix form, Eq. (2.19) can be represented as:

$$\ddot{\boldsymbol{\varrho}}(t) = \mathbf{G}(t)\dot{\boldsymbol{\varrho}}(t) + \mathbf{H}(t)\boldsymbol{\varrho}(t) + \boldsymbol{a}(t) + \boldsymbol{u}(t) \tag{2.20}$$

where:

$$\mathbf{G}(t) = 2\begin{bmatrix} 0 & \dot{\theta} & 0 \\ -\dot{\theta} & 0 & 0 \\ 0 & 0 & 0 \end{bmatrix} \quad \text{and} \quad \mathbf{H}(t) = \begin{bmatrix} H_{11} & \ddot{\theta} & 0 \\ -\ddot{\theta} & H_{22} & 0 \\ 0 & 0 & H_{33} \end{bmatrix} \tag{2.21}$$

with each diagonal component of the $\mathbf{H}(t)$ matrix defined as (Battin, 1999; Tillerson et al., 2002):

$$H_{11} = \dot{\theta}^2 + 2n^2\left(\frac{1+e\cos\theta}{1-e^2}\right)^3 \tag{2.22}$$

$$H_{22} = \dot{\theta}^2 - n^2\left(\frac{1+e\cos\theta}{1-e^2}\right)^3 \tag{2.23}$$

$$H_{33} = -n^2\left(\frac{1+e\cos\theta}{1-e^2}\right)^3 \tag{2.24}$$

2.4 State-Space Representation of Error Dynamics

Equations (2.19) can also be rearranged in state-space representation (Inalhan et al., 2002) using the state vector $\boldsymbol{x}(t) = \begin{bmatrix} x & y & z & \dot{x} & \dot{y} & \dot{z} \end{bmatrix}^T$ as:

$$\dot{\boldsymbol{x}}(t) = \mathbf{A}(t)\boldsymbol{x}(t) + \mathbf{B}(t)\left[\boldsymbol{a}(t) + \boldsymbol{u}(t)\right] \tag{2.25}$$

with dynamics matrix $\mathbf{A} \in \mathbb{R}^{6\times 6}$ and the control matrix $\mathbf{B} \in \mathbb{R}^{6\times 3}$ defined using (Bate et al., 1971):

$$\mathbf{A}(t) = \begin{bmatrix} \mathbf{0}_3 & \boldsymbol{I}_3 \\ \mathbf{G}(t) & \mathbf{H}(t) \end{bmatrix} \quad \mathbf{B}(t) = \begin{bmatrix} \mathbf{0}_3 \\ \boldsymbol{I}_3 \end{bmatrix} \tag{2.26}$$

and Eq. (2.13), (2.18) and (2.22 - 2.24). It is also possible to define Eq. (2.25) as a tracking error dynamics $\delta\boldsymbol{x}(t) \in \mathbb{R}^6$ with respect to a desired relative trajectory and velocity (also defined with respect to the centre of the formation) $\boldsymbol{x}_D(t) = \begin{bmatrix} x_D & y_D & z_D & \dot{x}_D & \dot{y}_D & \dot{z}_D \end{bmatrix}^T$ as $\delta\boldsymbol{x}(t) = \boldsymbol{x}(t) - \boldsymbol{x}_D(t)$

. After differentiating $\delta\boldsymbol{x}(t)$ we can obtain the following tracking dynamics:

$$\delta\dot{\boldsymbol{x}}(t) = \mathbf{A}(t)\delta\boldsymbol{x}(t) + \mathbf{B}(t)\left[\boldsymbol{a}(t) + \boldsymbol{u}(t)\right] \tag{2.27}$$

The same process of obtaining a tracking error can also be applied to a system defined by Eq. (2.20).

2.5 External Perturbations

In this work it is assumed the external accelerations and the control input in Eq. (2.27) are defined as:

$$\boldsymbol{a}(t) = \frac{\boldsymbol{F}_F(t)}{m_F} - \frac{\boldsymbol{F}_L(t)}{m_L} \tag{2.28}$$

and:

$$\boldsymbol{u}(t) = \boldsymbol{u}_F(t) - \boldsymbol{u}_L(t) \tag{2.29}$$

where $\boldsymbol{F}_F(t) \in \mathbb{R}^3$ and $\boldsymbol{F}_L(t) \in \mathbb{R}^3$ correspond to the external forces over the follower and the leader respectively. In order to simplify the design of the control law, the leader is forced to follow a Keplerian reference orbit, assuming that $\boldsymbol{u}_L(t) = -\boldsymbol{F}_L(t)/m_L$, which reduce the external acceleration and control vectors to $\boldsymbol{a}(t) = \boldsymbol{F}_F(t)/m_F$ and $\boldsymbol{u}(t) = \boldsymbol{u}_F(t)$.

As previously mentioned in Chapter 1, the simulations carried out in future chapters to test the performance of the controllers developed in this thesis, are based on several attributes and features present in the missions TanDEM-X (Montenbruck and Kahle, 2008), PRISMA (D'Amico et al., 2013) and PROBA-3 (Peters et al., 2014). One important aspect of these missions is that the reference orbit of the formation is a low Earth orbit in which perturbations like the effects due to Earth oblateness, specifically to the zonal harmonic coefficient J_2, and atmospheric drag are the most predominant external perturbations, especially over long periods of time (Sabatini and Palmerini, 2008). Given that the inclusion of these two perturbations in the linear plant can sensibly increase the performance of the controllers to be developed, in this work we assume that only the follower is influenced only by the zonal harmonic coefficient J_2 and the atmospheric drag, while the leader follow a Keplerian orbit, as previously explained.

The effects due to the zonal harmonic coefficient J_2, denoted here by $\boldsymbol{a}_J(t, \boldsymbol{x}) \in \mathbb{R}^3$, are by far the strongest perturbations due to Earth shape and affects the follower when considering a non-spherical Earth, giving rise to a perturbing acceleration coordinate-free expression defined as (Alfriend et al., 2009; Vallado, 1997):

$$\boldsymbol{a}_J(t, \boldsymbol{x}) = -\frac{\mu J_2 r_E^2}{2\|\boldsymbol{r}_F\|^5} \left\{ 6\left(\boldsymbol{r}_F \cdot \boldsymbol{k}\right)\boldsymbol{k} + \left[3 - \frac{15}{\|\boldsymbol{r}_F\|^2}\left(\boldsymbol{r}_F \cdot \boldsymbol{k}\right)^2\right]\boldsymbol{r}_F \right\} \tag{2.30}$$

where the vectors $\boldsymbol{r}(t) \in \mathbb{R}^3$ and $\boldsymbol{k}(t) \in \mathbb{R}^3$ may be expressed in $\boldsymbol{\mathcal{L}}$ coordinates as (Alfriend et al., 2009):

$$\boldsymbol{r}_F^{\mathcal{L}} = \begin{bmatrix} (r + x) \\ y \\ z \end{bmatrix} \quad \text{and} \quad \boldsymbol{k}^{\mathcal{L}} = \begin{bmatrix} s_\theta s_i \\ c_\theta s_i \\ c_i \end{bmatrix} \tag{2.31}$$

for spacecraft formation flying, with r_E as the equatorial radius of the Earth. In Eq. (5.29) the notation c_θ and s_θ is defined in reference to the sine and cosine of the true anomaly θ of the reference orbit, respectively, and the same notation applies to the orbit inclination angle i.

Even though the density at satellite altitudes (200 km and higher) is considerably lower than that at the sea level, the velocities of orbiting objects can be so high that there is still a drag acceleration affecting their performance. The differential acceleration exerted over the follower due to the effects of atmospheric drag $\boldsymbol{a}_D(t, \boldsymbol{x}) \in \mathbb{R}^3$ can be expressed by the equation (Vallado, 1997):

$$\boldsymbol{a}_D(t, \boldsymbol{x}) = -\frac{1}{2}\frac{C_D S \rho}{m_F}\left(\boldsymbol{v} - \boldsymbol{v}_{atm}\right)\|\boldsymbol{v} - \boldsymbol{v}_{atm}\| \tag{2.32}$$

with the vector $\boldsymbol{v} - \boldsymbol{v}_{atm} \in \mathbb{R}^3$ defined in the $\boldsymbol{\mathcal{L}}$ frame as (Alfriend et al., 2009):

$$\boldsymbol{v} - \boldsymbol{v}_{atm} = \begin{bmatrix} \dot{r} + \dot{x} - y\omega - z\omega_E c_\theta s_i + y\omega_E c_i \\ r\omega + \dot{y} + x\omega - (r + x)\omega_E c_i + z\omega_E s_\theta s_i \\ \dot{z} - y\omega_E s_\theta s_i + (r + x)\omega_E c_\theta s_i \end{bmatrix} \tag{2.33}$$

where $C_D \in \mathbb{R}$ is the drag coefficient defined with respect to the cross-sectional area, $S \in \mathbb{R}$ is the cross-sectional area with respect to drag, $\rho \in \mathbb{R}$ is the atmospheric density, $\omega_E \in \mathbb{R}$ is the angular velocity of Earth, $\boldsymbol{v} \in \mathbb{R}^3$ is the relative velocity of the follower and $\boldsymbol{v}_{atm} \in \mathbb{R}^3$ is the velocity of the atmosphere at the follower position.

Chapter 3

Spacecraft Formation Flying Control via Linear Optimal Tracking and Artificial Potential Functions

The objective of this chapter is to present the design of a mixed Linear Quadratic Regulator/Artificial Potential Function (LQR-APF) tracking controller for close-manoeuvring spacecraft in formation using dynamics of relative motion linearised near an elliptical reference orbit as presented in the work done by the author in reference (Palacios et al., 2015a). The proposed controller differs from other APF schemes, such as the ones presented in the work done by McInnes (McInnes, 1993), in that it merges the advantages of guidance control with the APF to provide a more complete control strategy. Furthermore, the proposed controller also differs from other LQR-APF formulations (McCamish et al., 2007) in that the control strategy offers a more general framework with capacity to deal with both circular and elliptical reference orbits. It provides guidance and tracking toward target nominal trajectories while optimising fuel consumption by Riccati procedure; additionally, the collision avoidance scheme, generated from a Gaussian-like potential function, is defined in terms of both spacecraft and obstacle position, ensuring evasive actions between the elements of the formation using repelling accelerations. This chapter starts introducing the theory of closed-loop optimal control of linear plants with quadratic performance index in Section 3.1, leading to the development of the Linear Quadratic Regulator (LQR) for state regulation and tracking. The LQR theory presented in this section may be complemented with the references (Athans and Falb, 2006; Bryson and Ho, 1975; Kwakernaak and Sivan, 1972; Lewis et al., 2012). Section 3.2 and 3.3 show the necessary conditions for controllability and a basic procedure to select the LQR weight matrices. The proposed control strategy is introduced in Section 3.4 and its performance is evaluated in the simulated scenarios in Section 3.5. Finally, conclusions are presented in Section 3.6.

3.1 Linear Quadratic Regulation

In this section, a general introduction to the LQR theory is presented. Later, in subsequent sections, it will be specifically applied to the problem presented in this thesis. First. consider a general linear, time-varying (LTV) system:

$$\dot{\boldsymbol{x}}(t) = \mathbf{A}(t)\boldsymbol{x}(t) + \mathbf{B}(t)\boldsymbol{u}(t) \tag{3.1}$$

with a cost functional defined as:

$$\mathcal{J}(t) = \frac{1}{2}\boldsymbol{x}(t_f)^T\mathbf{F}(t_f)\boldsymbol{x}(t_f) + \frac{1}{2}\int_{t_0}^{t_f}\Big\{\boldsymbol{x}(t)^T\mathbf{Q}(t)\boldsymbol{x}(t) + \boldsymbol{u}(t)^T\mathbf{R}(t)\boldsymbol{u}(t)\Big\}\,dt \tag{3.2}$$

where $\boldsymbol{x}(t)$ is the state vector and $\boldsymbol{u}(t)$ is the control vector. The matrix $\mathbf{A}(t)$ is the state matrix and $\mathbf{B}(t)$ is the control matrix. The control objective is then to keep the state vector $\boldsymbol{x}(t)$ close to zero without excessive control-energy expenditure $\boldsymbol{u}(t)$ (Bryson and Ho, 1975). For this purpose, the integrand:

$$\frac{1}{2}\boldsymbol{x}(t)^T\mathbf{Q}(t)\boldsymbol{x}(t) \tag{3.3}$$

should be nonnegative and small, which leads $\mathbf{Q}(t)$ to be symmetric and positive semidefinite. Also, the integrand:

$$\frac{1}{2}\boldsymbol{u}(t)^T\mathbf{R}(t)\boldsymbol{u}(t) \tag{3.4}$$

indicates a higher cost for larger control effort and since the control cost has to be a positive quantity, the matrix $\mathbf{R}(t)$ should be symmetric positive definite. The main purpose of the terminal cost weight matrix $\mathbf{F}(t)$ is to ensure that the vector $\boldsymbol{x}(t)$ is as small as possible at t_f and hence $\mathbf{F}(t)$ should be symmetric and positive semidefinite (Kwakernaak and Sivan, 1972). Within this formulation it is assumed that the initial condition $\boldsymbol{x}(0)$ is given and the terminal state $\boldsymbol{x}(t_f)$ is specified as the desired state. Given that optimizing execution time is not part of the objectives of this thesis (although it is considered in the Section 6 in the subsection corresponding to Future Work), the final time t_f is selected as the desired duration of the simulation. It is therefore necessary to select a time frame long enough to allow the controller to execute completely (which for our purpose is chosen as n times the reference orbit period). The procedure to obtain an optimal solution is based on Pontryagin minimum principle (Bryson and Ho, 1975) and is presented as follows using a Riccati approach. The Hamiltonian of the system comprised by Eq. (3.1) and the cost function in Eq. (3.2), is given as:

$$\begin{aligned} H\left[\boldsymbol{x}(t), \boldsymbol{u}(t), \boldsymbol{\lambda}(t)\right] &= \frac{1}{2}\boldsymbol{x}(t)^T\mathbf{Q}(t)\boldsymbol{x}(t) + \frac{1}{2}\boldsymbol{u}(t)^T\mathbf{R}(t)\boldsymbol{u}(t) \\ &\quad +\boldsymbol{\lambda}^T(t)\left[\mathbf{A}(t)\boldsymbol{x}(t) + \mathbf{B}(t)\boldsymbol{u}(t)\right] \end{aligned} \tag{3.5}$$

where $\boldsymbol{\lambda}(t)$ is the costate vector. Then the optimal control $\boldsymbol{u}^*(t)$ is obtained by using the relation:

$$\frac{\partial H}{\partial \boldsymbol{u}} = 0 \rightarrow \mathbf{R}(t)\boldsymbol{u}^*(t) + \mathbf{B}^T(t)\boldsymbol{\lambda}^*(t) = 0 \tag{3.6}$$

leading to:

$$\boldsymbol{u}^*(t) = -\mathbf{R}^{-1}(t)\mathbf{B}^T(t)\boldsymbol{\lambda}^*(t) \tag{3.7}$$

and the final condition:

$$\boldsymbol{\lambda}^*(t_f) = \mathbf{F}(t_f)\boldsymbol{x}^*(t_f) \tag{3.8}$$

where the superscript $(\ )^*$ refers to an optimal quantity. However, we can obtain the optimal control in Eq. (3.7) as a function of the state, after eliminating the costate $\boldsymbol{\lambda}^*(t)$, by examining the final condition given in Eq. (3.8) and assuming that:

$$\boldsymbol{\lambda}^*(t) = \mathbf{P}(t)\boldsymbol{x}^*(t) \tag{3.9}$$

where $\mathbf{P}(t)$ is a function to be determined. Using this form it is observed that the optimal control expression now becomes:

$$\boldsymbol{u}^*(t) = -\mathbf{R}^{-1}(t)\mathbf{B}^T(t)\mathbf{P}(t)\boldsymbol{x}^*(t) \tag{3.10}$$

which is now a negative feedback expression of the optimal state $\boldsymbol{x}^*(t)$. In order to obtain $\mathbf{P}(t)$ consider first the expressions:

$$\dot{\boldsymbol{x}}^*(t) = \frac{\partial H}{\partial \boldsymbol{\lambda}} \quad \text{which leads to} \quad \dot{\boldsymbol{x}}^*(t) = \mathbf{A}(t)\boldsymbol{x}^*(t) + \mathbf{B}(t)\boldsymbol{u}^*(t) \tag{3.11}$$

$$\dot{\boldsymbol{\lambda}}^*(t) = \frac{\partial H}{\partial \boldsymbol{x}} \quad \text{which leads to} \quad \dot{\boldsymbol{\lambda}}^*(t) = -\mathbf{Q}(t)\boldsymbol{x}^*(t) - \mathbf{A}^T(t)\boldsymbol{\lambda}^*(t) \tag{3.12}$$

and then let us differentiate Eq. (3.9) with respect to time to get:

$$\dot{\boldsymbol{\lambda}}(t) = \dot{\mathbf{P}}(t)\boldsymbol{x}^*(t) + \mathbf{P}(t)\dot{\boldsymbol{x}}^*(t) \tag{3.13}$$

In order to eliminate the costate $\boldsymbol{\lambda}^*(t)$, substitute Eq. (3.11) and (3.12) into Eq. (3.13) to obtain the expression:

$$\left[\dot{\mathbf{P}}(t) + \mathbf{P}(t)\mathbf{A}(t) + \mathbf{A}^T(t)\mathbf{P}(t) + \mathbf{Q}(t) - \mathbf{P}(t)\mathbf{B}(t)\mathbf{R}^{-1}(t)\mathbf{B}^T(t)\mathbf{P}(t)\right]\boldsymbol{x}^*(t) = \mathbf{0} \tag{3.14}$$

This equation should be satisfied for any t and for any initial state $\boldsymbol{x}(0)$, therefore it should hold for any value of $\boldsymbol{x}(t)$, meaning $\mathbf{P}(t)$ should satisfy the matrix differential equation:

$$\dot{\mathbf{P}}(t) = -\mathbf{P}(t)\mathbf{A}(t) - \mathbf{A}^T(t)\mathbf{P}(t) - \mathbf{Q}(t) + \mathbf{P}(t)\mathbf{B}(t)\mathbf{R}^{-1}(t)\mathbf{B}^T(t)\mathbf{P}(t) \tag{3.15}$$

This is the differential Riccati equation (DRE) and its solution is the optimal control feedback law. This equation must be solved backwards in time for the entire interval $[t, t_f]$ using the positive definite final condition:

$$\mathbf{P}(t_f) = \mathbf{F}(t_f) \tag{3.16}$$

leading to closed-loop stability of the system (Kwakernaak and Sivan, 1972):

$$\dot{\boldsymbol{x}}(t) = \left[\mathbf{A}(t) - \mathbf{B}(t)\mathbf{K}(t)\right]\boldsymbol{x}(t) \tag{3.17}$$

where $\mathbf{K}(t) = -\mathbf{R}^{-1}(t)\mathbf{B}^T(t)\mathbf{P}(t)$ is usually called the Kalman gain. The optimal control solution includes then the set equations summarised in Table (3.1).

Table 3.1 Summary of equations for the solution of the linear optimal control problem

$\dot{\mathbf{P}}(t) = -\mathbf{P}(t)\mathbf{A}(t) - \mathbf{A}^T(t)\mathbf{P}(t) - \mathbf{Q}(t) + \mathbf{P}(t)\mathbf{B}(t)\mathbf{R}^{-1}(t)\mathbf{B}^T(t)\mathbf{P}(t)$
$\dot{\boldsymbol{x}}(t) = \left[\mathbf{A}(t) - \mathbf{B}(t)\mathbf{K}(t)\right]\boldsymbol{x}(t)$
$\boldsymbol{u}^*(t) = -\mathbf{R}^{-1}(t)\mathbf{B}^T(t)\mathbf{P}(t)\boldsymbol{x}^*(t)$

The DRE depends only on the matrices $\mathbf{A}(t)$, $\mathbf{B}(t)$, $\mathbf{Q}(t)$ and $\mathbf{R}(t)$ and therefore it can be computed offline[1] using, for example, a backwards-in-time Runge-Kutta integration method, also known as the sweeping method (Bryson and Ho, 1975). Using a numerical method to solve the DRE may imply losing the symmetry of $\mathbf{P}(t)$. Therefore, it is necessary to symmetrise it after each step using the expression $1/2\left[\mathbf{P}(t)+\mathbf{P}^T(t)\right]$ (Kwakernaak and Sivan, 1972). An alternative procedure (not applied in this thesis) may be taking advantage of the symmetry of $\mathbf{P}(t)$ and eliminate the redundant terms in Eq. (3.15).

3.2 Kalman Controllability Conditions

The assessment of controllability, as defined by Kalman, is an important test for any controlled system and it is performed in order to find out if the control law obtained by solving the optimal control problem will be capable to drive any given state to another state in the limit $t_f = \infty$. If we would have to consider an infinite time interval in the cost function we certainly need controllability assessment by means of the controllability Grammian (Kalman, 1960), whose purpose is to impose conditions on the plant to ensure the control problem is meaningful in the time limit $t_f = \infty$. A plant is completely controllable at t if and only if the symmetric matrix:

$$\mathbf{W}_c(t_0,t_f) = \int_{t_0}^{t_f} \mathbf{\Phi}(t_0,t_f)\mathbf{B}(t)\mathbf{B}^T(t)\mathbf{\Phi}^T(t_0,t_f)dt \tag{3.18}$$

is positive definite for $t_f > t_0$ and $\mathbf{\Phi}(t_0,t_f)$ is the state transition matrix of Eq. (3.1). Nevertheless, this assessment is not necessary when dealing with cost functions with finite upper limits, as in the case of this thesis, because the contribution of the uncontrollable states to the cost function is always a finite quantity (Athans and Falb, 2006).

3.3 Selection of the Weight Matrices

In order to prevent large computational loads, it is assumed the weight matrices $\mathbf{Q}(t)$, $\mathbf{R}(t)$ and $\mathbf{F}(t)$ are time-invariant. Also for the previous reason and the sake of simplicity, they are assumed to be diagonal and $\mathbf{F} = \mathbf{Q}$. A simple yet practical rule to select the value of its diagonal elements

---

[1] computed during on-ground planning sessions and then uploaded to the satellite for execution

could be $\mathbf{Q} = \alpha\mathbf{I}$, $\mathbf{R} = \beta\mathbf{I}$ where the values of α and β are used for fine tune-up until an acceptable controller performance is found in terms of the designer desired dynamical behaviour. On the other hand, another choice for the selection of these values could be using a trial and error procedure on every element in the matrices. Additionally, several procedures to choose weight values have been proposed in literature using evolutionary algorithms, although these may be computationally heavy compromising part of the low computational load requirements proposed in this thesis (Li et al., 2008; Wongsathan and Sirima, 2009). In order to show the effects of the selection of the weight matrices on the performance of the LQR, a simple example is presented using the plant (Naidu, 2003):

$$\begin{aligned} \dot{x}_1(t) &= x_2(t) \\ \dot{x}_2(t) &= -2x_1(t) + x_2(t) + u(t) \end{aligned} \tag{3.19}$$

with initial conditions chosen as $x_1(0) = 2$ and $x_2(0) = -3$ and initial and final time as $t_0 = 0$ and $t_f = 15$ respectively. From this plant, we obtain the various matrix quantities required for the computation of the LQR:

$$\mathbf{A} = \begin{bmatrix} 0 & 1 \\ -2 & 1 \end{bmatrix} \quad \text{and} \quad \mathbf{B} = \begin{bmatrix} 0 \\ 1 \end{bmatrix} \tag{3.20}$$

For the first round of simulations, the weight matrices $\mathbf{Q}(t)$, $\mathbf{R}(t)$ and $\mathbf{F}(t)$ are selected using the first method with α and β equal to 1. The resulting plots are shown in Fig. (3.1).

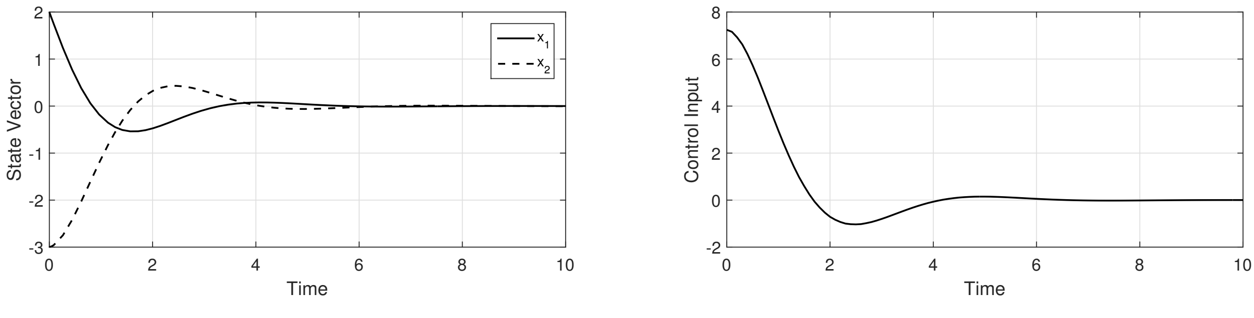

Fig. 3.1 State and control input with $\alpha = \beta = 1$

Changing the values of α and β yields to different dynamical performance. For instance, after changing the value of α to 10, while leaving β the same, the overshoot and the time of convergence of the state are noticeably reduced, as indicated in Fig. (3.2). This behaviour is observed since larger values of $\mathbf{Q}(t)$ in the cost functional $\mathcal{J}(t)$, in Eq. (3.2), yield to a stabilisation of the system with the least possible changes in the state. However, this rapid stabilisation leads to larger values of control input.

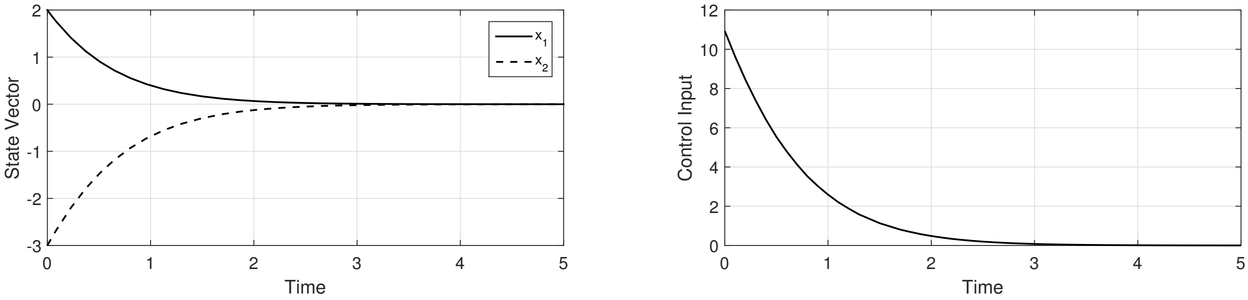

Fig. 3.2 State and control input with $\alpha = 10$ and $\beta = 1$

On the contrary, when the value of β is changed to 10, while α is leaving equal to 1, the overshoot and the time of convergence of the state is increased, as in Fig. (3.3). Selecting a large value of β in the cost functional $\mathcal{J}(t)$ means the system will stabilise using less energy, although, less energy to control the state means the state convergence time will increase.

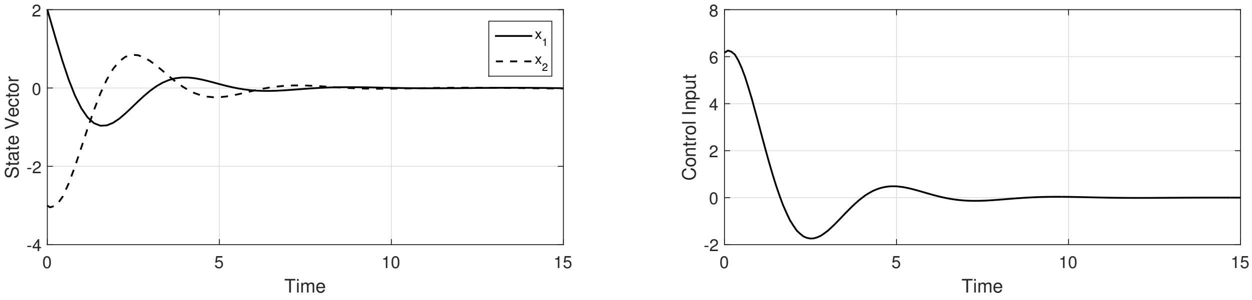

Fig. 3.3 State and control input with $\alpha = 1$ and $\beta = 10$

3.4 Control Strategy Design

3.4.1 LQR-Based Control

The Riccati-based procedure used in this chapter to control formation manoeuvres consists of two parts, tracking and collision avoidance, and it will be called LQR-APF control. First, the tracking of the nominal trajectories $\boldsymbol{x}_D(t) \in \mathbb{R}^6$ is achieved through the linear quadratic regulator (LQR) to minimise a quadratic cost function $\mathcal{J}(t) \in \mathbb{R}$ defined as:

$$\mathcal{J}(t) = \frac{1}{2}\delta\boldsymbol{x}(t_f)^T\mathbf{F}(t_f)\delta\boldsymbol{x}(t_f) + \frac{1}{2}\int_{t_0}^{t_f}\left\{\delta\boldsymbol{x}(t)^T\mathbf{Q}(t)\delta\boldsymbol{x}(t) + \boldsymbol{u}(t)^T\mathbf{R}(t)\boldsymbol{u}(t)\right\}dt \tag{3.21}$$

subjected to the state-space relative dynamics error $\delta\boldsymbol{x}(t) = \boldsymbol{x}(t) - \boldsymbol{x}_D(t) \in \mathbb{R}^6$ previously defined in Chapter 2 as:

$$\delta\dot{\boldsymbol{x}}(t) = \mathbf{A}(t)\delta\boldsymbol{x}(t) + \mathbf{B}(t)\left[\boldsymbol{a}(t) + \boldsymbol{u}(t)\right] \tag{3.22}$$

with the weight matrices $\mathbf{F}(t) \geq \mathbf{0} \in \mathbb{R}^{6\times6}$, $\mathbf{Q}(t) \geq \mathbf{0} \in \mathbb{R}^{6\times6}$, and $\mathbf{R}(t) > \mathbf{0} \in \mathbb{R}^{3\times3}$ perturbed by the nonlinear vector $\boldsymbol{a}_R(t) \in \mathbb{R}^3$, which in this chapter only includes the effects of the repelling accelerations generated by the collision avoidance scheme (presented in the next subsection). To provide an optimal solution to this problem the Riccati procedure presented in the previous section is used, along with the control law $\boldsymbol{u}(t) \in \mathbb{R}^3$ of the form:

$$\boldsymbol{u}(t) = -\mathbf{R}^{-1}(t)\mathbf{B}^T(t)\mathbf{P}(t)\delta\boldsymbol{x}(t) = \mathbf{K}(t)\delta\boldsymbol{x}(t) \tag{3.23}$$

and $\mathbf{P}(t)$ is the solution of the DRE in Eq. (3.15) with final value $\mathbf{P}(t_f) = \mathbf{F}(t_f)$. To show the general performance of the controller and the effects of the selection of the values of the weight matrices without the term $\boldsymbol{a}_R(t)$, a simple illustrative example is presented next. The full performance of the controller, including the effects of $\boldsymbol{a}_R(t)$ will be presented in the simulations in the following section. Consider a follower moving relative to the leader in the $\boldsymbol{\mathcal{L}}$ frame with initial and final position as observed in Fig. (3.4) and Table 3.2.

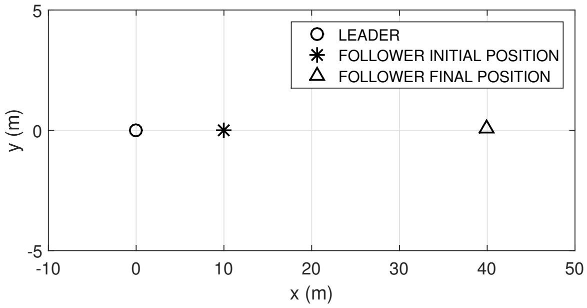

Fig. 3.4 Initial state

The objective of this example is to perform a manoeuvre in which the follower moves from its initial position at 10 m from the leader, on the $x-$ axis, to its final position at 40 m from the leader

Table 3.2 Initial and final conditions

Initial state (m and m/s)	$\begin{bmatrix} 10 & 0 & 0 & 0 & 0 & 0 \end{bmatrix}^T$
Final state (m and m/s)	$\begin{bmatrix} 40 & 0 & 0 & 0 & 0 & 0 \end{bmatrix}^T$

on the same axis. To this purpose α and β are selected to be 15 and 1, respectively for the first round of the simulation, leading to the performance observed in Fig. (3.5).

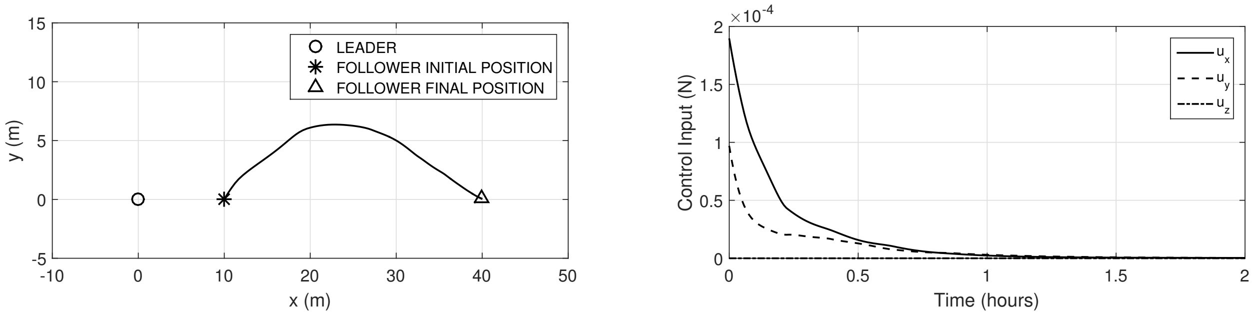

Fig. 3.5 State and control input with $\alpha = 15$ and $\beta = 1$

When the value of α is increased, for example to 25, while leaving β with its previous value then the convergence of the state of the follower toward the desired final position is faster, although with larger control input requirements, as noticed in Fig. (3.6). On the other hand, when the value of β is increased to 5, while leaving α with its initial value of 15, it is noticed in Fig. (3.7) that smaller values of control input are available to execute the manoeuvre and therefore, the follower moves far away from the $x-$axis before arriving to the desired final position.

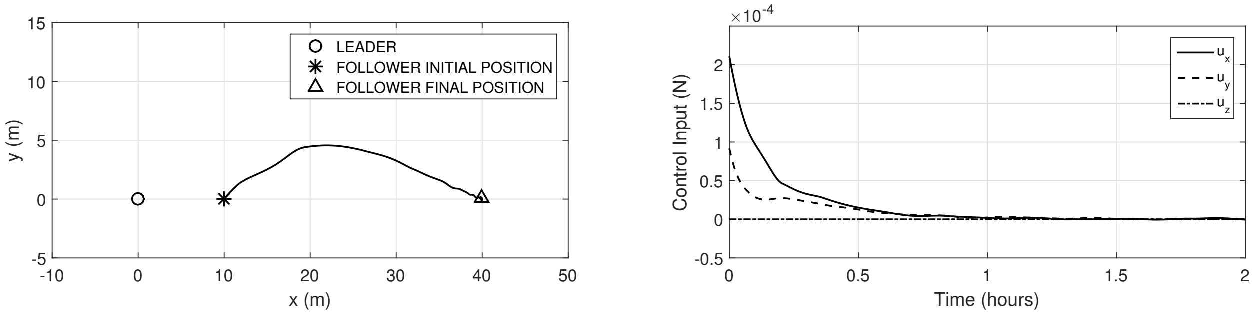

Fig. 3.6 State and control input with $\alpha = 25$ and $\beta = 1$

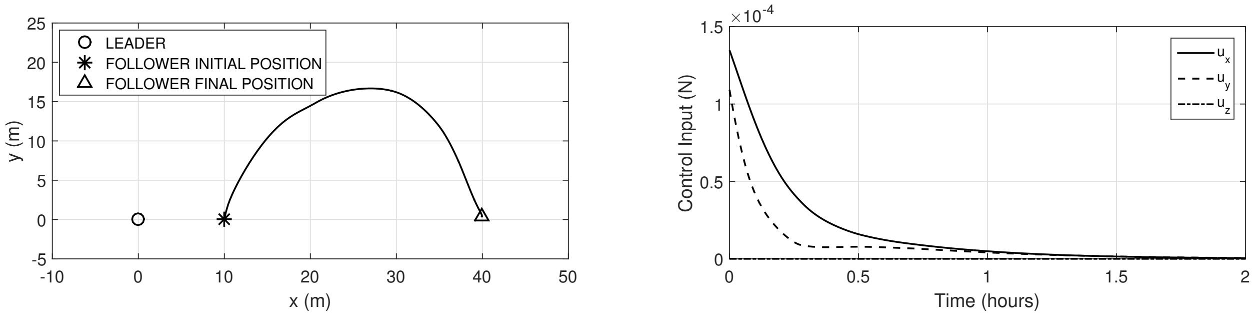

Fig. 3.7 State and control input with $\alpha = 15$ and $\beta = 5$

3.4.2 Obstacle Avoidance Scheme

Collision avoidance during manoeuvring is achieved through repulsive accelerations created by artificial potential functions (APF) (McInnes, 1993) between an actual spacecraft and an obstacle spacecraft. The accelerations, obtained through the negative gradient of the APF, result in a non-linear continuous dynamical system in which stability can be investigated robustly by Lyapunov methods. This type of scheme accounts for the separation distance of both spacecraft and obstacles, without previous knowledge of their trajectories. To obtain such accelerations, the proposed potential function $U \in \mathbb{R}$ is defined as a Gaussian-like function:

$$U = A \exp\left[-\frac{1}{\sigma}\|\boldsymbol{\varrho} - \boldsymbol{\varrho}_o\|^2\right] \tag{3.24}$$

where $\sigma \in \mathbb{R}$ is the width of the Gaussian function and the amplitude $A \in \mathbb{R}$ is a positive constant defined as (McQuade and McInnes, 1997):

$$A = \frac{\varepsilon_R \left(D + \|\boldsymbol{\varrho}_o\| - \|\boldsymbol{\varrho}_D\|\right)}{6 \exp(-3D)} \tag{3.25}$$

Here, the parameter $\varepsilon_R \in \mathbb{R}$ is a scaling factor for the strength of the potential, $\boldsymbol{\varrho}_o(t) \in \mathbb{R}^3$ is the relative position of the obstacle spacecraft, the term $\boldsymbol{\varrho}_D(t) \in \mathbb{R}^3$ is the desired position of the spacecraft from the desired state $\boldsymbol{x}_D = \begin{bmatrix} \boldsymbol{\varrho}_D & \dot{\boldsymbol{\varrho}}_D \end{bmatrix}^T$ and $D \in \mathbb{R}$ is the effective dimension of the obstacle. The potential U in Eq. (3.24) can be implemented in a simulation by tuning its parameters depending on the problem requirements, for example, Fig. (3.8) and (3.9) shows plots of the surface and the associated contours of the repulsive potential on a specific point of a 3-dimensional space.

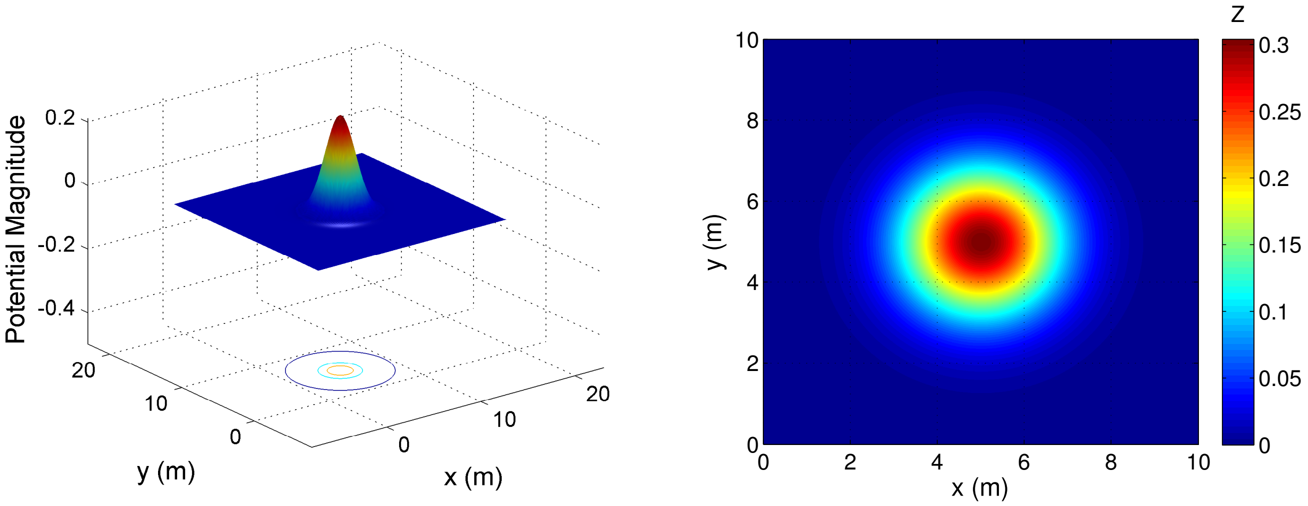

Fig. 3.8 Potential Distribution with $\varepsilon_R = 3 \times 10^{-8}$ and $D = 10$ m

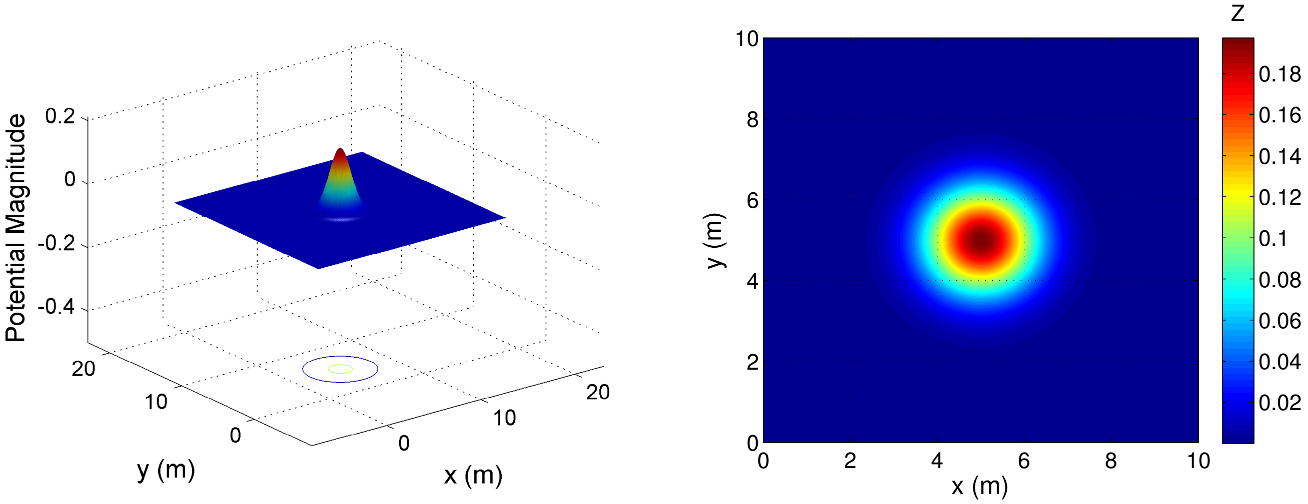

Fig. 3.9 Potential Distribution with $\varepsilon_R = 3 \times 10^{-7}$ and $D = 5$ m

Moreover, the corresponding repulsive acceleration $\boldsymbol{a}_R(t) \in \mathbb{R}^3$ can be defined as the negative gradient of the potential with respect to the spacecraft position and denoted as (McQuade and McInnes, 1997):

$$\boldsymbol{a}_R(t) = -\frac{2\varepsilon_R \left(D + \|\boldsymbol{\varrho}_o\| - \|\boldsymbol{\varrho}_D\|\right)}{6\exp(-3D)} \exp\left[-\frac{1}{\sigma}\|\boldsymbol{\varrho} - \boldsymbol{\varrho}_o\|^2\right] (\boldsymbol{\varrho} - \boldsymbol{\varrho}_o) \tag{3.26}$$

When considering multiple spacecraft, one spacecraft sees all other spacecraft as obstacles. Therefore, the total repulsive acceleration for one spacecraft is defined as the summation of all the

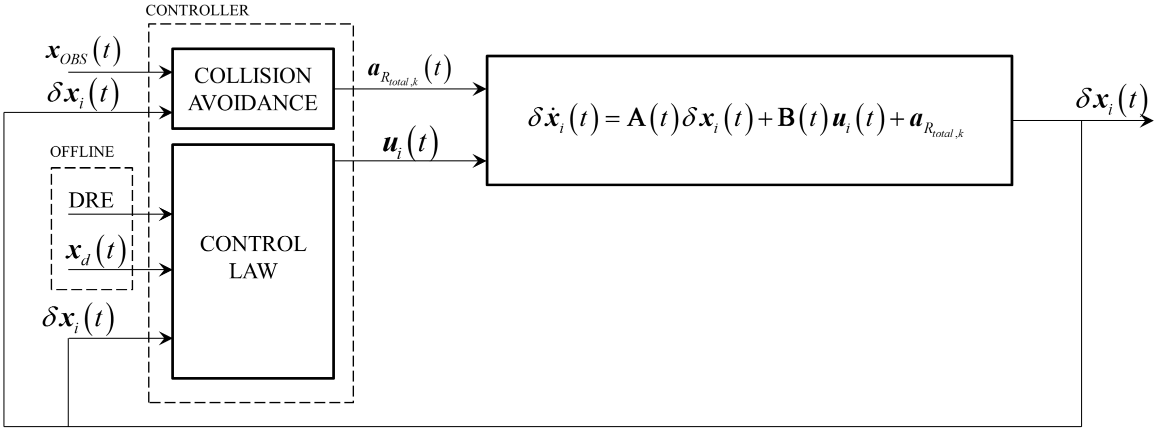

Fig. 3.10 Guidance and control scheme

repulsive accelerations due to the rest of the spacecraft in formation:

$$\boldsymbol{a}_{R_{total,k}}(t) = \sum_{\substack{i=1 \\ i\neq k}}^{j} \boldsymbol{a}_{R_i}(t) \tag{3.27}$$

where k represents the current spacecraft and j the total number of spacecraft involved in the manoeuvre.

3.4.3 Final Control Strategy

The control approach presented in this chapter is summarised in the diagram in Fig. (3.10) where the index i represents the current spacecraft and the subscript *obs* represent the signal with information about all the obstacle spacecraft. The algorithm tasks to implement the controller in a simulation are divided in two parts: offline (which can be subsequently uploaded to the spacecraft) and online (performed in-orbit). First, define offline the time vector, initial values of the weight matrices and the parameters of the repelling acceleration signal. Next, also offline and for every spacecraft in the formation, define the desired trajectory, the initial state and solve the corresponding DREs. Using these results, the signal of the control input and the repelling accelerations are calculated online respectively for every element in the formation. Next, the state of every spacecraft is integrated simultaneously and online using a numerical integrator such as *ode*45 in MATLAB. This control algorithm is also presented in Table (3.3).

Table 3.3 LQR-APF control algorithm

```
OFFLLINE
1. Define the time vector $t$
2. Obtain the values of the weight matrices $\mathbf{Q}$, $\mathbf{R}$ and $\mathbf{F}$
3. Select the parameters of the repelling acceleration $\lambda$, $\sigma$ and $D$
4. For every spacecraft in the formation:
    a. Define the initial state and the desired trajectory
    b. Solve the DRE, $\dot{\mathbf{P}}(t)$
5. Incorporate each spacecraft state into a single state vector $\boldsymbol{x}(t)$
6. Incorporate each spacecraft desired state into a single desired state vector $\boldsymbol{x}_D(t)$
7. Obtain the state error vector $\delta\boldsymbol{x}(t)$
ONLINE
For every time step in the simulation:
    1. Obtain the signal of the control input $\boldsymbol{u}(t)$
    2. For every spacecraft in the formation:
        a. Obtain the signal of the repelling accelerations
    3. Incorporate each signal of the CAS into a single $\boldsymbol{a}_R(t)$ vector
    4. Integrate the state error $\delta\dot{\boldsymbol{x}}(t)$
```

3.5 Simulations

To demonstrate the effectiveness of the proposed guidance and control system, two simulated scenarios are presented in the next subsections using eccentric reference orbits and PRISMA (De Florio et al., 2013) as reference mission. In these scenarios, several followers transfer to and then track a predefined target nominal trajectory while collision between the elements of the formation is avoided. The proposed controller is implemented using the model in Eq. (3.22) together with the control law in Eq. (3.23) and the CAS in Eq. (3.27) and it is assumed that no external perturbations, such as J_2 and atmospheric drag, affect the performance of the satellites and the controller. The capabilities of the proposed controller are analysed in terms of values of total manoeuvre delta-v (Δv) and fuel consumption, calculated using the equations:

$$\Delta v = \int_{t_0}^{t_f} \|\boldsymbol{u}_T(t)\| dt \tag{3.28}$$

and:

$$m_f = m_0 \exp\left(\frac{\Delta v}{g_0 I_{sp}}\right) \tag{3.29}$$

respectively, with and without the effects of the CAS. When considering the effects of the CAS, the vector $\boldsymbol{u}_T(t)$ corresponds to the sum of the control input and the repelling acceleration. The values of the initial mass of the follower m_0 and the specific impulse I_{sp} used in the following scenarios are defined in the next section and $g_0 = 9.81$ m/s^2. The simulations were carried out on a PC with a processor Intel(R) Core(TM) i5-3570 with 3.40 GHz, 4.00 GB of RAM and ode45 from MATLAB 2015 with an absolute and relative tolerance of 1×10^{-08}.

3.5.1 Scenario 1

This scenario simulates the on-orbit transfer of two Mango satellites with initial and final conditions as indicated in Table (3.4). The reference orbit has an eccentricity of 0.25, a perigee altitude of 450 km and a period of 2.4 hours.

Table 3.4 Initial and final conditions in Scenario 1

	MANGO 1	**MANGO 2**
Initial position (m)	$\begin{bmatrix} -15 & -50 & 0 \end{bmatrix}^T$	$\begin{bmatrix} 15 & -50 & 0 \end{bmatrix}^T$
Initial velocity (m/s)	$\begin{bmatrix} 0.35 & 0.35 & 0 \end{bmatrix}^T$	$\begin{bmatrix} -0.17 & 0.17 & 0 \end{bmatrix}^T$
Final position (m)	$\begin{bmatrix} -15 & 0 & 0 \end{bmatrix}^T$	$\begin{bmatrix} 15 & 0 & 0 \end{bmatrix}^T$
Final velocity (m/s)	$\begin{bmatrix} 0 & 0 & 0 \end{bmatrix}^T$	$\begin{bmatrix} 0 & 0 & 0 \end{bmatrix}^T$

First, the scenario is simulated without the effects of the CAS and its results are compared to those obtained when the CAS is active. In this scenario, the diagonal of the LQR gains are tuned using the procedure presented in Section 3.3. For this scenario $\alpha = 150$, leading to $\mathbf{Q} = \text{diag}\,[150]$. It is also assumed there is no restriction on the control input, meaning $\beta = 1$, which in turn yield $\mathbf{R} = \text{diag}\,[1]$. Also t_f is defined as twice the period of the reference orbit. Finally, the weight $\mathbf{F}$ is selected as $\mathbf{F} = \mathbf{Q}$ as suggested in references (Athans and Falb, 2006; Bryson and Ho, 1975; Kwakernaak and Sivan, 1972; Lewis et al., 2012). In both scenarios, it is assumed that every Mango occupies a spherical volume with a diameter of 2.6 m, taking into account the fully-deployed solar panels of Mango (See Table (1.1) in Chapter 1). However, a virtual safety layer is added to every spacecraft by surrounding each one of them with a spherical virtual volume, with a diameter approximated by the parameter D in Eq. (3.25). In this scenario, $D = 5$ m and the nondimensional CAS parameters are chosen as

$\lambda = -1.833 \times 10^{-6}$ and $\sigma = 1$. Starting at the perigee of the reference orbit, the planar manoeuvre carried out by both satellites during the simulation with and without the CAS is showed in Fig. (3.11), in terms of displacement in the $x - y$ plane of the $\mathcal{L}$ frame.

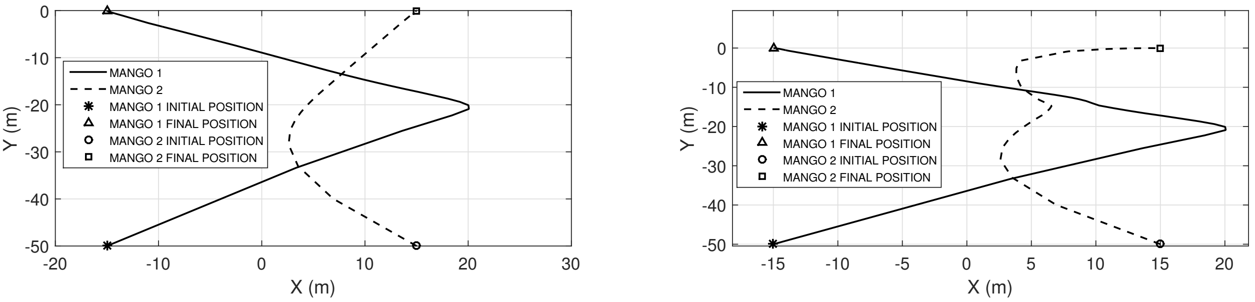

(a) Without CAS

(b) With CAS

Fig. 3.11 Manoeuvre trajectory in Scenario 1

The manoeuvre without the effects of the CAS is observed in Fig. (3.11a) where the followers' trajectories approach each other until, eventually, they intersect, resulting in a collision. This is not the case when the CAS is acting on them in Fig. (3.11b) and although it seems their trajectories collide, this intersection happens at different times, as observed in Fig. (3.12), where the separation distance between the followers during the entire manoeuvre is presented with and without the effects of the CAS.

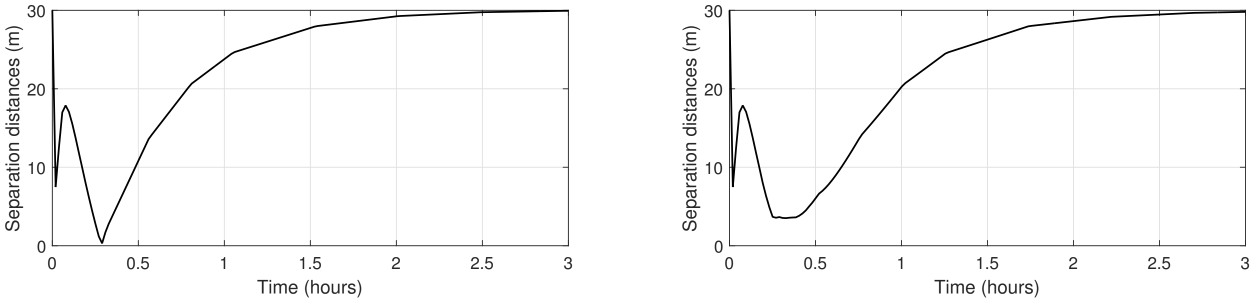

(a) Without CAS

(b) With CAS

Fig. 3.12 Separation distance between the spacecraft in Scenario 1

It is observed in Fig. (3.12a) that without the CAS the spacecraft generate a collision. Using the CAS with the previously selected parameters allow these separation distances to be shifted beyond the safety limit, as observed in Fig. (3.12b), decreasing the collision risk of the manoeuvre. This shift is also perceived in the error dynamics as indicated in Fig. (3.13a) in contrast with Fig. (3.13b), where the additional manoeuvring to avoid collision can be also observed.

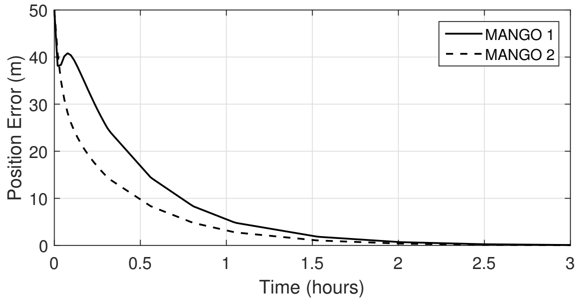

(a) Without CAS

(b) With CAS

Fig. 3.13 Magnitude of the position error in Scenario 1

This feature is likewise observable in the thrust behaviour as seen in Fig. (3.14) where an additional amount of thrust is required to carry out the avoidance action. The total control input with CAS has two components, the control input used to track the desired trajectory and the repulsive force used for collision avoidance. The later, can be observed in Fig. (3.15).

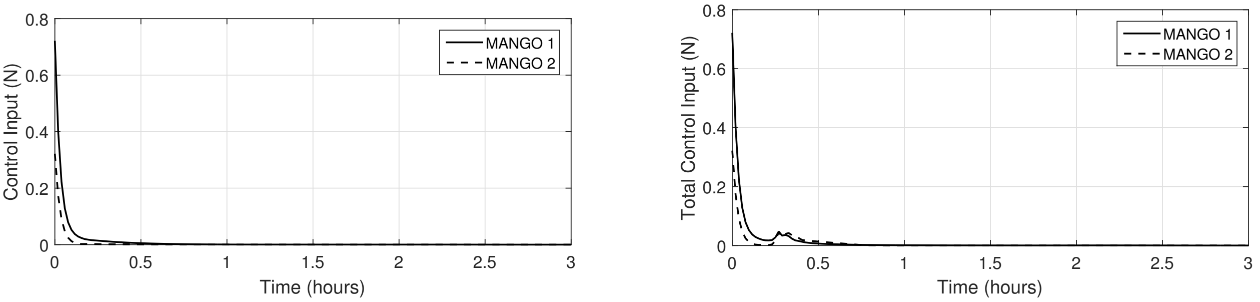

(a) Without CAS

(b) With CAS

Fig. 3.14 Magnitude of the control input in Scenario 1

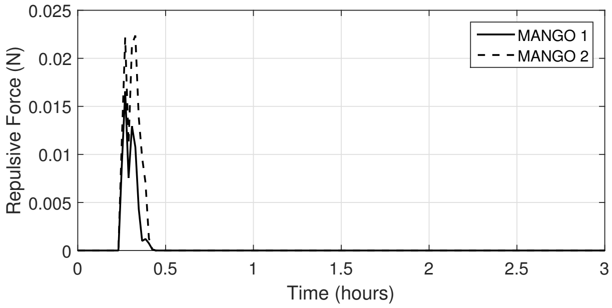

Fig. 3.15 Repulsive force used for collision avoidance in Scenario 1

The behaviour observed during the manoeuvres has an impact on Δv and fuel consumption, as observed in Table (3.5) where the requirements of the manoeuvring to avoid collision creates a difference between the values obtained with and without CAS. For instance, Mango 1 increases its total manoeuvre Δv and fuel consumption by 15%. The CAS parameters λ and σ in Eq. (3.25) are selected by trial-and-error by the designer together with D, in order to obtain a desired collision avoidance profile. A specific selection of these parameters will also have certain influence on the overall system performance during a collision threat, specifically in manoeuver Δv. For example, selecting different values of the parameter D means adjusting the virtual safety volume of the spacecraft, but also having some repercussion on the overall final values of manoeuver Δv.

Table 3.5 Summary of results for Scenario 1

WITHOUT CAS	**MANGO 1**	**MANGO 2**	**TOTAL**
Δv (m/s)	0.72	0.24	0.969
Fuel consumption (g)	50.12	17.33	67.45
Max. Thrust (N)	0.72	0.32	1.04
Final Position Error (m)	0	0	0
Final Velocity Error (m/s)	0	0	0
WITH CAS	**MANGO 1**	**MANGO 2**	**TOTAL**
Δv (m/s)	0.83	0.46	1.29
Fuel consumption (g)	58.02	32.3	90.32
Max. Thrust (N)	0.72	0.322	1.04
Final Position Error (m)	0	0	0
Final Velocity Error (m/s)	0	0	0

Table 3.6 CAS parameters tune-up and corresponding Δv and fuel consumption for Mango 1. Each row represents a test case where the named parameter is set as specified, while the others are those defined in Scenario 1

Parameter	**Δv (m/s)**	**Fuel Consumption (g)**
$D = 6$ m	0.91	63.29
$\sigma = 2.5$	0.98	68.43

The same reasoning would apply to the selection of the parameters λ and σ, however, it is worth to mention that the final overall values of manoeuver Δv will depend also on the model of the plant dynamics, tracking controller performance and the nature of the scenario in consideration. For instance, selecting a value of $D = 6$ m increases Δv and fuel consumption in Mango 1 by almost 10% as observed in Table (3.6), while relevant plots are depicted in Fig (3.16). Increasing σ would provide a similar effect as D in terms of Δv and fuel consumption, for example, after selecting a value of

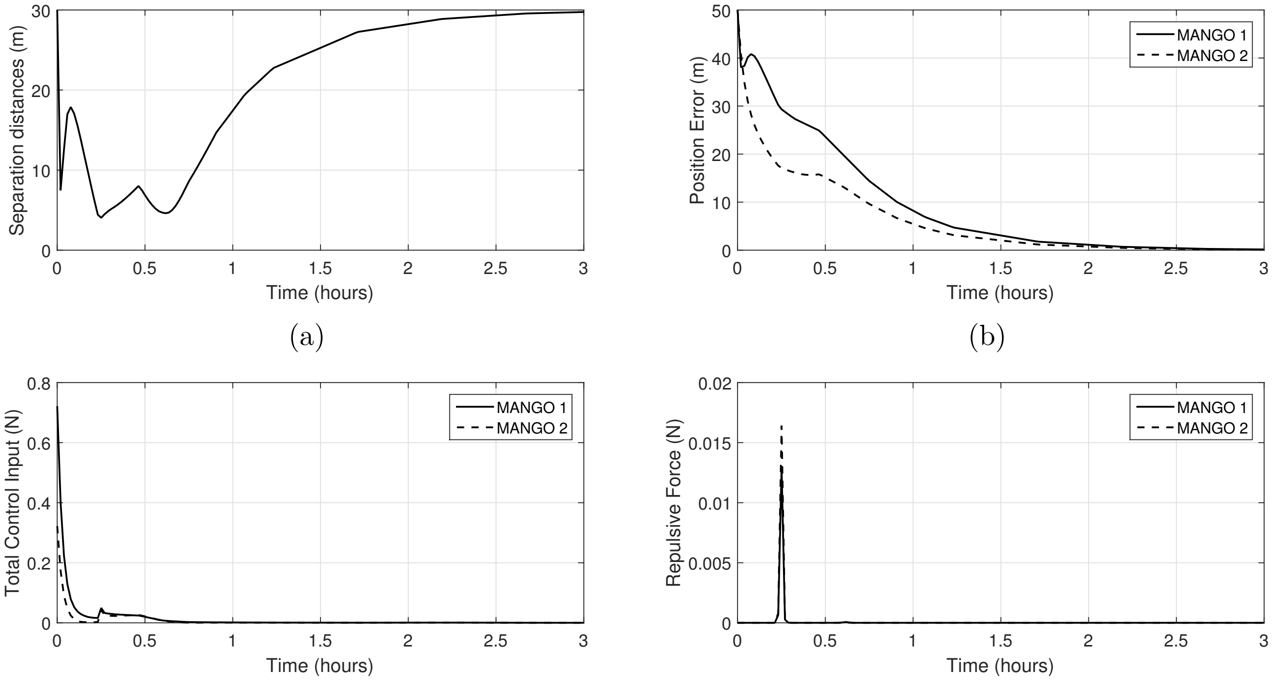

(a) (b)

(c) (d)

Fig. 3.16 Relevant plots with $D = 6$ m in Scenario 1

$\sigma = 2.5$ it can be noticed in Table (3.6) that Δv and fuel consumption in Mango 1 increase by 18%, while pertinent plots to this σ value are presented in Fig (3.17). As a final note on this scenario, in this last figure two peaks of collision avoidance input are noticed, meaning that the spacecraft required two avoidance manoeuvers at different times.

3.5.2 Scenario 2

In this scenario, a manoeuvre with four Mango satellites is simulated, each located at one vertex of an imaginary square with side length of 20 m in the $y - z$ plane and centred at the origin of the $\mathcal{L}$ reference frame, with initial and final states as observed in Table (3.7). Here, the same reference orbit as in Scenario 1 is used and t_f is defined as twice the period of the reference orbit.

Table 3.7 Initial and final conditions in Scenario 2

	MANGO 1	**MANGO 2**	**MANGO 3**	**MANGO 4**
Initial position (m)	$\begin{bmatrix} 0 & -10 & 10 \end{bmatrix}^T$	$\begin{bmatrix} 0 & 10 & 10 \end{bmatrix}^T$	$\begin{bmatrix} 0 & 10 & -10 \end{bmatrix}^T$	$\begin{bmatrix} 0 & -10 & -10 \end{bmatrix}^T$
Initial velocity (m/s)	$\begin{bmatrix} 0 & 0 & 0 \end{bmatrix}^T$	$\begin{bmatrix} 0 & 0 & 0 \end{bmatrix}^T$	$\begin{bmatrix} 0 & 0 & 0 \end{bmatrix}^T$	$\begin{bmatrix} 0 & 0 & 0 \end{bmatrix}^T$
Final position (m)	$\begin{bmatrix} 0 & 10 & -10 \end{bmatrix}^T$	$\begin{bmatrix} 0 & -10 & -10 \end{bmatrix}^T$	$\begin{bmatrix} 0 & -10 & 10 \end{bmatrix}^T$	$\begin{bmatrix} 0 & 10 & 10 \end{bmatrix}^T$
Final velocity (m/s)	$\begin{bmatrix} 0 & 0 & 0 \end{bmatrix}^T$	$\begin{bmatrix} 0 & 0 & 0 \end{bmatrix}^T$	$\begin{bmatrix} 0 & 0 & 0 \end{bmatrix}^T$	$\begin{bmatrix} 0 & 0 & 0 \end{bmatrix}^T$

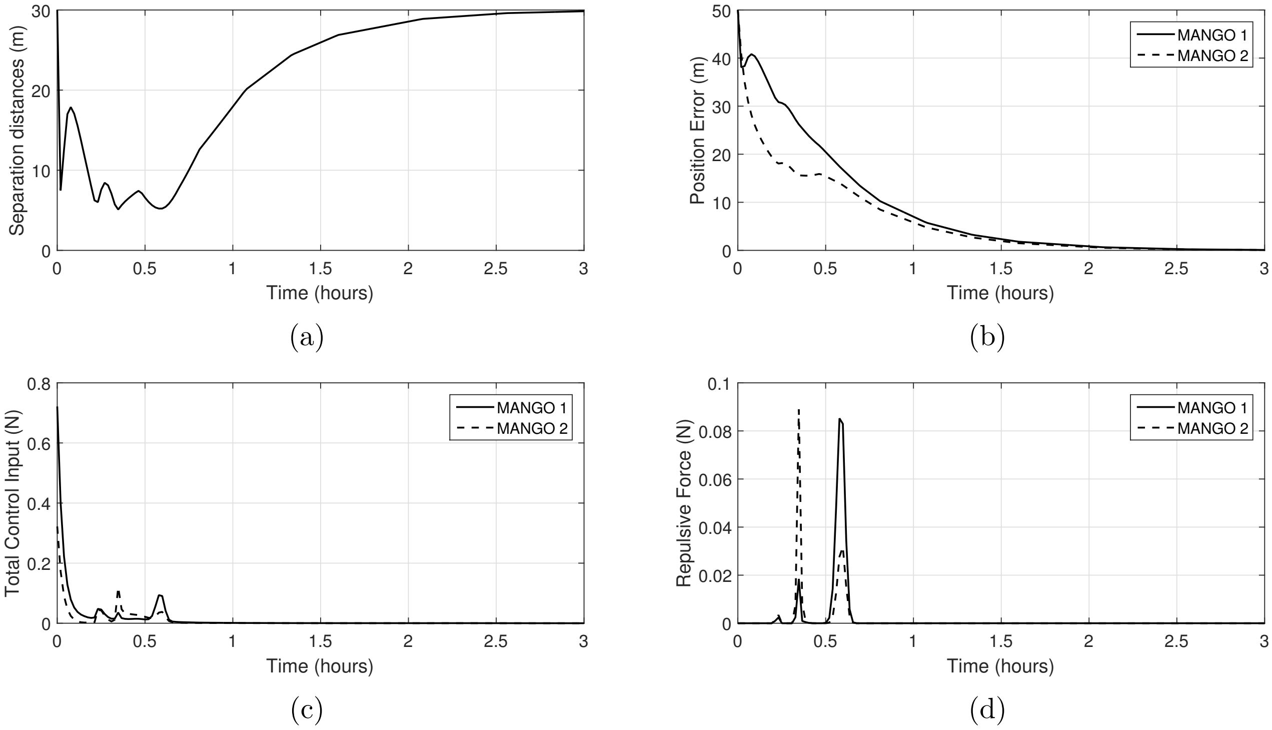

(a) (b)

(c) (d)

Fig. 3.17 Relevant plots with $\sigma = 2.5$ in Scenario 1

The objective of this manoeuvre is to swap positions diagonally while avoiding collision between the spacecraft. The values of the LQR matrices providing the desired controller output where the same as in the previous scenario and the CAS parameters are selected as $D = 5$ m, $\lambda = -1.883 \times 10^{-6}$ and $\sigma = 2.5$. The 3D manoeuvre, with and without the effects of the CAS, is shown in Fig. (3.18).

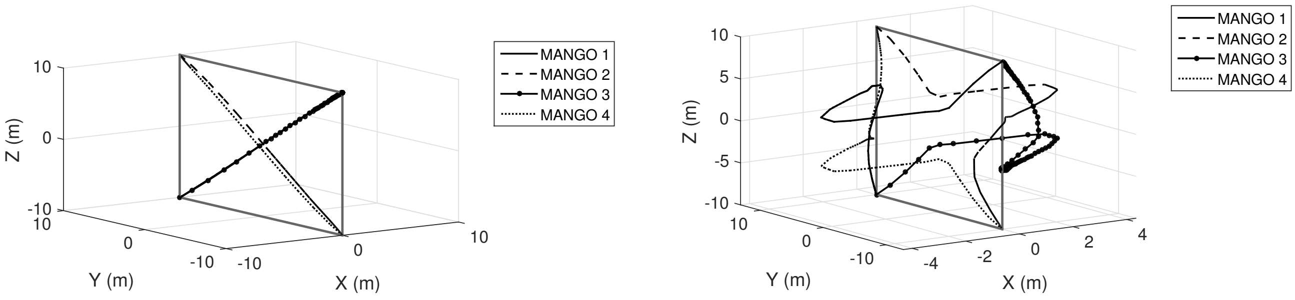

(a) Without CAS (b) With CAS

Fig. 3.18 Manoeuvre trajectory in Scenario 2

When a collision avoidance action is taken, extra manoeuvring is observed, as in Fig. (3.18b), in contrast with those manoeuvres without CAS in Fig. (3.18a). These avoidance actions are also visible in Fig. (3.19) where the separation distance between each spacecraft is plotted for the complete manoeuvre.

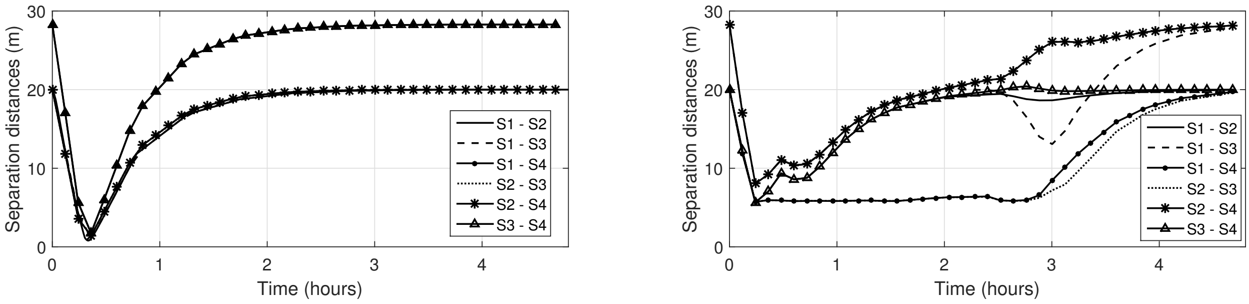

(a) Without CAS

(b) With CAS

Fig. 3.19 Separation distance in Scenario 2

In Fig. (3.19a), it is also observed that without the CAS some spacecraft generate a collision threat, which vanishes when the CAS is activated shifting the separation distances above the safety limit, as observed in Fig. (3.19b). This shift is also perceived in the error dynamics as indicated in Fig. (3.20a) in contrast with Fig. (3.20b) and in the thrust behaviour as seen in Fig. (3.21a) and (3.21b). The components of the total thrust input, obtained with the CAS, can also be observed in Fig (3.22).

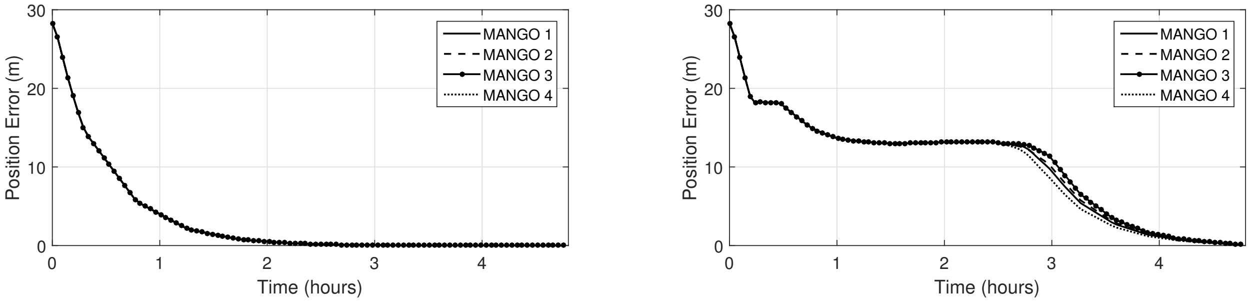

(a) Without CAS

(b) With CAS

Fig. 3.20 Magnitude of the position error in Scenario 2

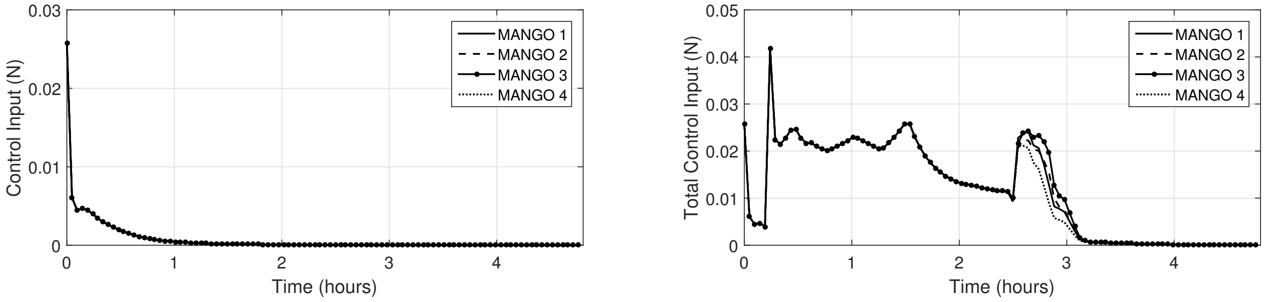

(a) Without CAS

(b) With CAS

Fig. 3.21 Magnitude of the control input in Scenario 2

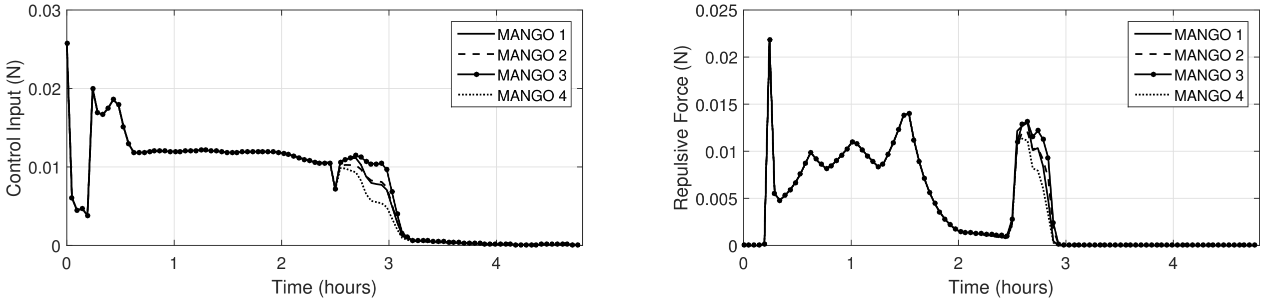

(a) (b)

Fig. 3.22 Components of the total control input with CAS in Scenario 2

As expected, the avoidance manoeuvres modify the results in terms of and fuel consumption, as seen in Table (3.8), where differences are shown between the values obtained with and without CAS; for example, Mango 4 increased its Δv and fuel consumption by approximately 1800%.

Table 3.8 Summary of results for Scenario 2

WITHOUT CAS	**MANGO 1**	**MANGO 2**	**MANGO 3**	**MANGO 4**	**TOTAL**
Δv (m/s)	0.071	0.071	0.071	0.071	0.284
Fuel consumption (g)	4.94	4.94	4.94	4.94	19.76
Max. Thrust (N)	0.025	0.025	0.025	0.025	0.1
Final Position Error (m)	0.001	0.001	0.001	0.001	0.004
Final Velocity Error (m/s)	0	0	0	0	0
WITH CAS	**MANGO 1**	**MANGO 2**	**MANGO 3**	**MANGO 4**	**TOTAL**
Δv (m/s)	1.32	1.32	1.35	1.28	5.27
Fuel consumption (g)	91.97	92.11	94.52	89.15	367.75
Max. Thrust (N)	0.02	0.02	0.02	0.02	0.08
Final Position Error (m)	0.13	0.14	0.15	0.11	0.53
Final Velocity Error (m/s)	0	0	0	0	0

3.5.3 Scenario 3

This scenario simulates the on-orbit transfer of two Mango satellites using a high-eccentricity reference orbit with an eccentricity value of 0.8, a perigee altitude of 450 km and a period of 17.5 hours. Once more, the scenario is simulated without the effects of the CAS and its results are compared to those obtained when the CAS is active. Also, the diagonal of the LQR gains are selected the same as in Scenario 1 and the CAS parameters are selected as $D = 5$ m, $\lambda = 1.0 \times 10^{-9}$ and $\sigma = 8$. In this scenario, two Mangos are located collinearly along the x axis of the $\mathcal{L}$ reference frame with initial and final conditions as indicated in Table (3.9).

Table 3.9 Initial and final conditions in Scenario 3

	MANGO 1	**MANGO 2**
Initial position (m)	$\begin{bmatrix} -10 & 0 & 0 \end{bmatrix}^T$	$\begin{bmatrix} 10 & 0 & 0 \end{bmatrix}^T$
Initial velocity (m/s)	$\begin{bmatrix} 0.015 & 0 & 0 \end{bmatrix}^T$	$\begin{bmatrix} -0.015 & 0 & 0 \end{bmatrix}^T$
Final position (m)	$\begin{bmatrix} 10 & 0 & 0 \end{bmatrix}^T$	$\begin{bmatrix} -10 & 0 & 0 \end{bmatrix}^T$
Final velocity (m/s)	$\begin{bmatrix} 0 & 0 & 0 \end{bmatrix}^T$	$\begin{bmatrix} 0 & 0 & 0 \end{bmatrix}^T$

The objective of this manoeuvre is to interchange the positions between the two satellites, while generating a collision threat during the movement. The manoeuvre in the $x - y$ plane of the $\mathcal{L}$ frame, with and without the effects of the CAS, is shown in Fig. (3.23). It is observed in Fig. (3.23b) that extra manoeuvring is generated due to collision avoidance action, in contrast with the movement in Fig. (3.23a) without CAS. The effects caused by these additional manoeuvres are visible in the behaviour of the separation distance in Fig. (3.24), where it is observed that without the CAS some spacecraft generate a collision threat in Fig (3.24a), which vanishes when the CAS is activated in Fig. (3.24b).

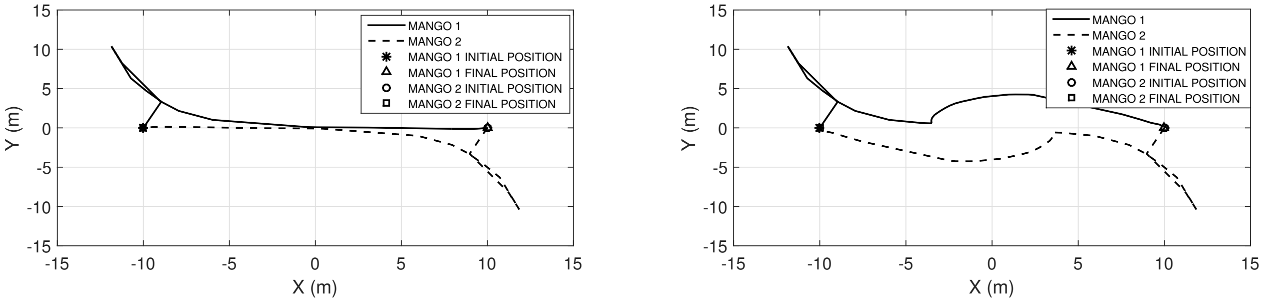

(a) Without CAS

(b) With CAS

Fig. 3.23 Manoeuvre trajectory in Scenario 3

These effects are also perceived in the error dynamics as indicated in Fig. (3.25a) and (3.25b), in the thrust behaviour as seen in Fig. (3.26) and in the components of the total thrust input in Fig (3.27). As in the previous scenarios, the avoidance manoeuvres generated by the CAS have influence in Δv and fuel consumption, as seen in Table (3.10), in contrast with those manoeuvres obtained without CAS; for example, Mango 2 increased its Δv and fuel consumption by approximately 43%.

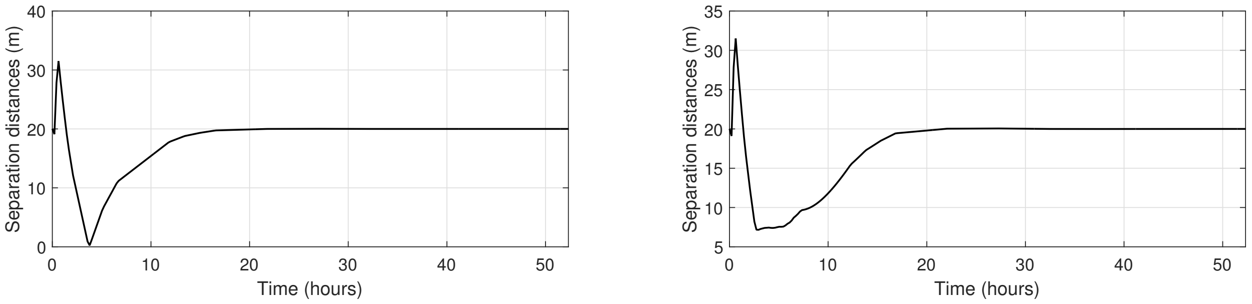

(a) Without CAS (b) With CAS

Fig. 3.24 Separation distance in Scenario 3

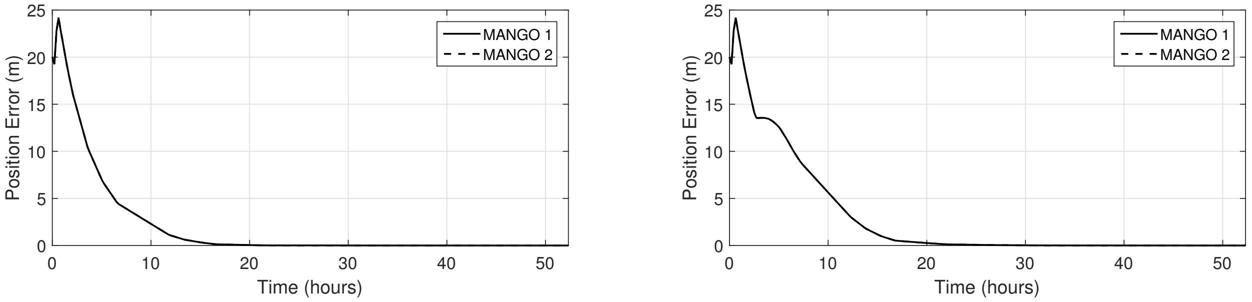

(a) Without CAS (b) With CAS

Fig. 3.25 Magnitude of the position error in Scenario 3

Table 3.10 Summary of results for Scenario 3

WITHOUT CAS	**MANGO 1**	**MANGO 2**	**TOTAL**
Δv (m/s)	0.094	0.094	0.188
Fuel consumption (g)	6.55	6.55	13.1
Max. Thrust (N)	0.009	0.009	0.018
Final Position Error (m)	0	0	0
Final Velocity Error (m/s)	0	0	0
WITH CAS	**MANGO 1**	**MANGO 2**	**TOTAL**
Δv (m/s)	0.13	0.13	0.26
Fuel consumption (g)	9.42	9.42	18.84
Max. Thrust (N)	0.009	0.009	0.018
Final Position Error (m)	0	0	0
Final Velocity Error (m/s)	0	0	0

3.6 Chapter Conclusions

A tracking controller with collision avoidance capabilities for formation flying in close proximity, using Riccati procedure and repulsive accelerations from an artificial potential field, in eccentric reference

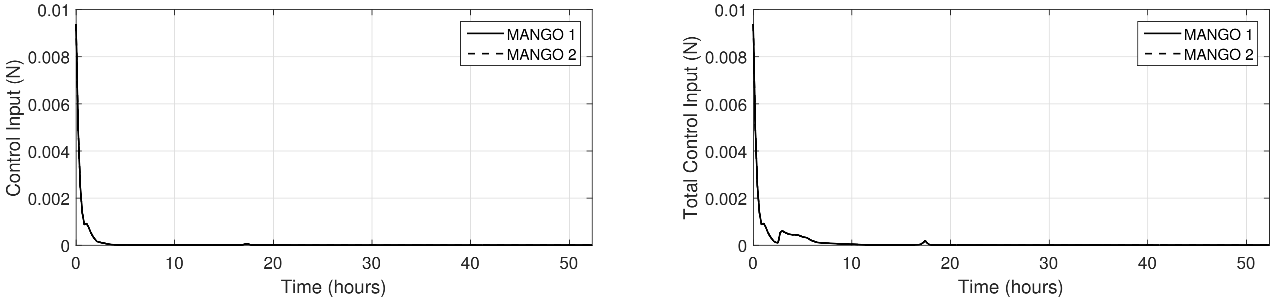

(a) Without CAS (b) With CAS

Fig. 3.26 Magnitude of the control input in Scenario 3

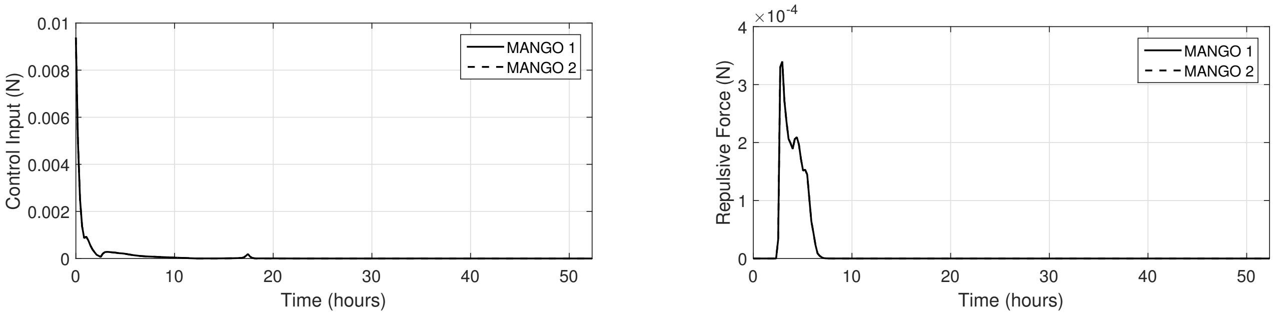

(a) (b)

Fig. 3.27 Components of the total control input with CAS in Scenario 3

orbits was presented. The controller was implemented in three scenarios for spacecraft formation reconfiguration and swapping, showing that the performance of the controllers, in terms of total manoeuvre Δv and fuel consumption, was affected by the selection of the weight matrices and CAS parameters. The scenarios also demonstrated that the controller allowed the spacecraft to effectively track the nominal trajectory with a final error close to zero, while showing an effective decrease of collision risk during the performance of the manoeuvre. When the manoeuver was carried out including the effects of the CAS, the final values of total Δv and fuel consumption were increased with respect to the same manoeuvre without CAS, although this increment was expected since the spacecraft with the effects of CAS required additional collision avoidance manoeuvres, especially in those spacecraft with higher collision risk. As mentioned in Table 1.1, the propellant tank included in the spacecraft Mango of PRISMA mission contains about 5.6 kg of usable fuel and gives approximately 60 m/s Δv over the mission. Averaging the LQR-CAS Δv per spacecraft per manoeuvre we obtain a value of 0.85 m/s, which would allow a follower with the same fuel tanks features as Mango, to perform up to 70 manoeuvres. The average MATLAB execution time for the backward integration of the Riccatti equations was 0.075 seconds, while for the integration of the dynamics was 0.240 seconds.

These two measurements add up to a total time of 0.315 seconds, which suggests that this algorithm may be suitable for current on-board satellite computational capacities. The simulations presented in this chapter assumed a perfect knowledge of the spacecraft state throughout the entire manoeuvre. In reality, the presence of uncertainty in the measuring and modelling of the state must be accounted. This is the main focus of the next chapter.

Chapter 4

Spacecraft Formation Flying Control via State Estimation and Artificial Potential Functions

The control laws developed in the previous chapter presented a fundamental limitation: an assumption of perfect knowledge of the spacecraft states. This assumption, required in many cases to obtain closed-form solutions, is not valid in a realistic scenario and the existence of noise in state measurements requires incorporating a state estimator in the control loop. Therefore, the contribution of this chapter is to apply, for the first time, the forward-in-time state estimation approach developed in (Damak et al., 2013) to close-manoeuvring control and collision-avoidance spacecraft in formation. The state estimator accounts for both model and measurement uncertainty in the control process and the separation principle allows the observer and the controller to be designed independently. The equations of motion used in the design of this controller consist of the linearised relative motion for both circular and eccentric reference orbits. This chapter starts by introducing state estimation theory in Section 4.1 presenting the concept of state observer and its optimal solution. The conditions for observability and the forward-in-time separation principle are then presented in Section 4.2 and 4.3, respectively. Next, the control strategy for spacecraft formation flying (SFF) is introduced in Section 4.4 while the way to account for model and sensor uncertainty is presented in Section 4.5. Simulated scenarios and chapters conclusions are presented in section 4.6 and 4.7. The information presented in this chapter may be complemented with references (Athans and Falb, 2006; Bryson and Ho, 1975; Geering, 2007; Kwakernaak and Sivan, 1972).

4.1 State Estimation

In the previous chapter, control strategies were obtained assuming the availability of information about the system state however, such assumptions do not agree with realistic scenarios where uncertainties can arise from both modelling errors and sensor/actuator noise. Here, the necessary control theory applied to a general dynamical system is presented. Then, in further sections, this is applied to formation flying. The most frequent situation involves a system:

$$\begin{aligned} \dot{\boldsymbol{x}}(t) &= \mathbf{A}(t)\boldsymbol{x}(t) + \mathbf{B}(t)\boldsymbol{u}(t) \\ \boldsymbol{y}(t) &= \mathbf{C}(t)\boldsymbol{x}(t) \end{aligned} \tag{4.1}$$

where only certain elements of the state, denoted by the observed variable $\boldsymbol{y}(t)$, can be measured and $\mathbf{C}(t)$ is a linearised sensor representation. State estimation is therefore a method that allows to approximately reconstruct the actual state vector $\boldsymbol{x}(t)$ form the observed variable $\boldsymbol{y}(t)$. The reconstructed state is a function of the past observations and does not depend on future observations. Once the actual state vector $\boldsymbol{x}(t)$ is reconstructed, we will be able to use the linear optimal control strategies presented in Chapter 3 by replacing the actual state with the reconstructed state. Feedback control on the other hand, is a control strategy that uses information obtained from sensor measurements to manipulate the state of a system in order to achieve a desired response. Specifically, when the observed variable $\boldsymbol{y}(t)$ serves as input to the controller, the control system is called output feedback control system (OFCS). In general within this thesis, OFCS will be called feedback control for simplicity. Feedback control by state estimation involves two stages: regulation and estimation. The first stage requires the design of a full state feedback controller using the state vector reconstructed by means of the estimator. The second stage requires the design of an additional dynamical system, called the estimator, to obtain the states which cannot be measured, in order to approximately reconstruct the full state vector. For this purpose, the $n-$dimensional system (Kwakernaak and Sivan, 1972; Lewis et al., 2012):

$$\dot{\hat{\boldsymbol{x}}}(t) = \mathbf{A}(t)\hat{\boldsymbol{x}}(t) + \mathbf{B}(t)\boldsymbol{u}(t) + \mathbf{L}(t)\left[\boldsymbol{y}(t) - \mathbf{C}(t)\hat{\boldsymbol{x}}(t)\right] \tag{4.2}$$

is a full-order Luenberger observer for the system in Eq (4.1) with $\mathbf{L}(t)$ as an arbitrary time-varying matrix, if the condition $\hat{\boldsymbol{x}}(0) = \boldsymbol{x}(0)$ implies $\hat{\boldsymbol{x}}(t) = \boldsymbol{x}(t)$ for all $t \geq t_0$. The matrix $\mathbf{L}(t)$ is known as the gain matrix of the observer and $\hat{\boldsymbol{x}}(t)$ is the estimation of the state. The design of an observer, therefore, involves the optimal determination of the gain matrix of the observer in such way that the reconstruction error $\boldsymbol{e}(t) = \boldsymbol{x}(t) - \hat{\boldsymbol{x}}(t)$, satisfies the differential equation (Lewis et al., 2012):

$$\dot{\boldsymbol{e}}(t) = [\mathbf{A}(t) - \mathbf{L}(t)\mathbf{C}(t)]\, \boldsymbol{e}(t) \tag{4.3}$$

and has the property $\boldsymbol{e}(t) \to \mathbf{0}$ as $t \to \infty$. To obtain a fast error convergence rate, the matrix $\mathbf{L}(t)$ must be selected in such way that the poles of the matrix $\mathbf{A}(t) - \mathbf{L}(t)\mathbf{C}(t)$ are located far down the left-half complex plane (Lewis et al., 2012). However, this usually leads to very large values for $\mathbf{L}(t)$ which makes the observer sensitive to observation noise added to the observed variable $\boldsymbol{y}(t)$. To meet the two contrasting requirements, a balance must therefore be found. In state estimation, a stochastic linear approach may be used by making specific assumptions in terms of disturbances and observation errors. In this case, it is assumed the actual system is defined as (Lewis et al., 2012):

$$\begin{aligned} \dot{\boldsymbol{x}}(t) &= \mathbf{A}(t)\boldsymbol{x}(t) + \mathbf{B}(t)\boldsymbol{u}(t) + \boldsymbol{w}_1(t) \\ \boldsymbol{y}(t) &= \mathbf{C}(t)\boldsymbol{x}(t) + \boldsymbol{w}_2(t) \end{aligned} \tag{4.4}$$

where the term $\boldsymbol{w}_1(t)$ is the state excitation noise and $\boldsymbol{w}_2(t)$ is the observation noise. Then, the problem of finding $\mathbf{L}(t)$ for $t_0 \leq t \leq t_f$ and $\hat{\boldsymbol{x}}(0)$ for Eq. (4.2) in order to minimize the mean square reconstruction error:

$$E\left\{\boldsymbol{e}(t)\mathbf{W}(t)\boldsymbol{e}(t)\right\} \tag{4.5}$$

is called the optimal observer problem, where $\mathbf{W}(t)$ is a positive-definite symmetric weight matrix and $\boldsymbol{e}(t) = \boldsymbol{x}(t) - \hat{\boldsymbol{x}}(t)$. In general, when the plant is linear and time-invariant, the matrix $\mathbf{L}$ may be obtained through a selective eigenvalue principle using, for example, Butterworth polynomials which are a common way to design low-pass filters (Franklin et al., 2001). When considering time-varying nonlinear plants, as in this thesis, more general procedures must be found in order to obtain the matrix $\mathbf{L}(t)$. One of these procedures, which is based on the forward-in-time separation principle (Damak et al., 2013; Palacios et al., 2014), is presented in Section 4.3. Nonetheless, the condition for observability is introduced first.

4.2 Conditions for Observability

A continuous-time system is observable if, for any initial state $\boldsymbol{x}(0)$ and any final time $t_f > 0$, the initial state $\boldsymbol{x}(0)$ can be uniquely determined by knowledge of the input $\boldsymbol{u}(t)$ and the output $\boldsymbol{y}(t)$ for all $t \in [0, t_f]$. In other words, if a system is observable then the initial state can be determined, and if the initial state can be determined then all states between the initial and final times can be determined (Simon, 2006). A dynamical system is completely observable if the observability Gramian (Bryson and Ho, 1975; Michal, 2008):

$$\mathbf{W}_o(t_0, t_f) = \int_{t_0}^{t_f} \mathbf{\Phi}(t_0, t_f)^T \mathbf{C}^T(t)\mathbf{C}(t)\mathbf{\Phi}(t_0, t_f)dt \tag{4.6}$$

is nonsingular for any $t > 0$ and $\mathbf{\Phi}(t_0, t_f)$ is the state transition matrix of Eq.(4.1) (Bryson and Ho, 1975).

4.3 The Forward-in-Time Separation Principle

Given the remarks from control theory included in the previous sections and the possibility of having a time-varying dynamical system, it is possible to construct the feedback control problem as a combination of an observer and a control law obtained as if the complete state was available for observation. On this regard, the separation principle states that an observer built for a known input can also be used to estimate the state of the system and then, to generate the control input (Kwakernaak and Sivan, 1972; Lewis et al., 2012). This statement allows us to design the observer and the feedback independently, with the assurance that the poles of the closed-loop system will be those selected for the feedback and those selected for the observer (Kwakernaak and Sivan, 1972). Consider the system in Eq. (4.1) and assume that the whole state is available for measure in order to obtain a control law of the form $\boldsymbol{u}(t) = \mathbf{K}(t)\boldsymbol{x}(t)$, where the Kalman gain is defined as $\mathbf{K}(t) = -\mathbf{R}^{-1}(t)\mathbf{B}^T(t)\mathbf{P}(t)$ as in Chapter 3. If the state is not available for measurements, then we could propose an observer as in Eq. (4.2) and then connect the control law with the partially reconstructed state $\hat{\boldsymbol{x}}(t)$ as:

$$\boldsymbol{u}(t) = \mathbf{K}(t)\hat{\boldsymbol{x}}(t) \tag{4.7}$$

in order to have the augmented system:

$$\begin{aligned} \dot{\hat{\boldsymbol{x}}}(t) &= \left[\mathbf{A} + \mathbf{B}(t)\mathbf{K}(t) - \mathbf{L}(t)\mathbf{C}(t)\right]\hat{\boldsymbol{x}}(t) + \mathbf{L}(t)\boldsymbol{y}(t) \\ \boldsymbol{u}(t) &= \mathbf{K}(t)\hat{\boldsymbol{x}}(t) \end{aligned} \tag{4.8}$$

After interconnecting the dynamics in Eq. (4.1) and the observer in Eq. (4.2) with the control law in Eq. (4.7), we obtain a closed-loop linear system described by (Lewis et al., 2012):

$$\left\{ \begin{array}{c} \dot{\boldsymbol{x}}(t) \\ \dot{\hat{\boldsymbol{x}}}(t) \end{array} \right\} = \left[\begin{array}{cc} \mathbf{A}(t) & -\mathbf{B}(t)\mathbf{K}(t) \\ \mathbf{L}(t)\mathbf{C}(t) & \mathbf{A} + \mathbf{B}(t)\mathbf{K}(t) - \mathbf{L}(t)\mathbf{C}(t) \end{array} \right] \left\{ \begin{array}{c} \boldsymbol{x}(t) \\ \hat{\boldsymbol{x}}(t) \end{array} \right\} \tag{4.9}$$

which in terms of stability and the reconstruction error $\dot{\boldsymbol{e}}(t) = \dot{\boldsymbol{x}}(t) - \dot{\hat{\boldsymbol{x}}}(t)$, takes the form of Eq. (4.3) and the state $\dot{\boldsymbol{x}}(t) = \dot{\boldsymbol{e}}(t) + \dot{\hat{\boldsymbol{x}}}(t)$ takes the form:

$$\dot{\boldsymbol{x}}(t) = \left[\mathbf{A} - \mathbf{B}(t)\mathbf{K}(t)\right]\boldsymbol{x}(t) + \mathbf{B}(t)\mathbf{K}(t)\boldsymbol{e}(t) \tag{4.10}$$

Thus, we observe in Eq. (4.3) that $\boldsymbol{e}(t)$ converges to zero if an appropriate selection of the $\mathbf{L}(t)$ matrix is made. Moreover, it is observed in Eq. (4.10) that if $\boldsymbol{e}(t)$ converges to zero and $\mathbf{B}(t)$ and $\mathbf{K}(t)$ are bounded, then $\boldsymbol{x}(t)$ will always converge to zero if the matrix $\mathbf{A}(t) - \mathbf{B}(t)\mathbf{K}(t)$ asymptotically tends to zero. Therefore, to achieve this, $\mathbf{K}(t)$ may be obtained by solving the backwards-in-time differential Riccati equation (DRE). In practice, a backwards-in-time solution procedure, such as the one presented in Chapter 3, has the significant drawback that the Riccatti equations must be solved first before the propagating the controller and dynamics, which implies the dynamics of the system and maybe the dynamics of the reference trajectory (in case tracking control is considered), must be known in advance (Weiss et al., 2012). For instance, consider Eq. (2.27) in Chapter 3. The matrix $\mathbf{A}(t)$ depends on the values of the true anomaly $\theta(t)$ and its rates, which is analytically known for circular and elliptical Keplerian orbits, as observed in Eq. (2.13) and (2.18). However, when external perturbations are considerer (such as the effects of $J2$) this analytical expressions are no longer valid and the true anomaly must be obtained from measurements at every current time step. Consequently, there is interest in forward-in-time solution procedures (Weiss et al., 2012). To avoid such problems, in this thesis, the forward-in-time state estimation approach presented in (Damak et al., 2013) is applied for the first time to formation flying, in order to propagate both, Riccatti equations and dynamics simultaneously from the initial conditions. This approach applies to time-varying systems and therefore can be applied to tracking problems. In order to define the control framework, the rest of the equations in this section were obtained from (Damak et al., 2013). First, the gain $\mathbf{K}(t)$ is defined as:

$$\mathbf{K}(t) = \mathbf{R}^{-1}(t)\bar{\mathbf{B}}^{T}(t)\mathbf{P}(t) \tag{4.11}$$

where $\mathbf{P}(t)$ is the solution of the forward-in-time DRE:

$$\dot{\mathbf{P}}(t) = -\bar{\mathbf{A}}^{T}(t)\mathbf{P}(t) - \mathbf{P}(t)\bar{\mathbf{A}}(t) - \mathbf{P}(t)\bar{\mathbf{B}}(t)\mathbf{R}^{-1}(t)\bar{\mathbf{B}}^{T}(t)\mathbf{P}(t) + \mathbf{Q}(t) \tag{4.12}$$

with matrices:

$$\begin{aligned} \mathbf{P}(t_0) &= \mathbf{P}_0 \\ \bar{\mathbf{A}}(t) &= -\mathbf{T}(\boldsymbol{x})\mathbf{A}(t)\mathbf{T}^{-1}(\boldsymbol{x}) \\ \bar{\mathbf{B}}(t) &= \mathbf{T}(\boldsymbol{x})\mathbf{B}(t) \\ \mathbf{T}(\boldsymbol{x}) &= \mathbf{I} - 2\frac{\boldsymbol{x}(t)\boldsymbol{x}^{T}(t)}{\boldsymbol{x}^{T}(t)\boldsymbol{x}(t)} \end{aligned} \tag{4.13}$$

and weight matrices:

$$\mathbf{Q}(t) \geq \mathbf{0} \in \mathbb{R}^{6\times 6} \quad \text{and} \quad \mathbf{R}(t) > \mathbf{0} \in \mathbb{R}^{3\times 3} \tag{4.14}$$

The gain $\mathbf{L}(t)$, which improves and/or speeds up the convergence of the error, is determined by solving the forward-in-time mean square construction error $\dot{\mathbf{V}}(t)$, which has the form of a DRE. These are defined as:

$$\mathbf{L}(t) = \mathbf{V}(t)\mathbf{C}^{T}(t)\mathbf{W}_2^{-1}(t) \tag{4.15}$$

$$\dot{\mathbf{V}}(t) = \mathbf{A}(t)\mathbf{V}(t) + \mathbf{V}(t)\mathbf{A}^{T}(t) - \mathbf{V}(t)\mathbf{C}^{T}(t)\mathbf{W}_2^{-1}(t)\mathbf{C}(t)\mathbf{V}(t) + \mathbf{W}_1(t) \tag{4.16}$$

with $\mathbf{V}(0) = \mathbf{V}_0 > 0 \in \mathbb{R}^{6\times 6}$ and the diagonal matrices $\mathbf{W}_1 > 0 \in \mathbb{R}^{6\times 6}$ and $\mathbf{W}_2 > 0 \in \mathbb{R}^{6\times 6}$ representing the weight matrices for model and sensor uncertainty respectively, which must be tuned up in such way that the elements of $\mathbf{L}(t)$ are as small as possible. Once the gains and the control input are obtained, the system comprising the observer and the dynamics is represented as:

$$\begin{Bmatrix} \dot{\boldsymbol{x}}(t) \\ \dot{\hat{\boldsymbol{x}}}(t) \end{Bmatrix} = \begin{bmatrix} \mathbf{A}(t) & -\mathbf{B}(t)\mathbf{K}(t) \\ \mathbf{L}(t)\mathbf{C}(t) & \mathbf{A}+\mathbf{B}(t)\mathbf{K}(t)-\mathbf{L}(t)\mathbf{C}(t) \end{bmatrix} \begin{Bmatrix} \boldsymbol{x}(t) \\ \hat{\boldsymbol{x}}(t) \end{Bmatrix} + \begin{Bmatrix} \mathbf{0} \\ \mathbf{L}(t)\boldsymbol{y}(t) \end{Bmatrix} \tag{4.17}$$

4.4 Control Strategy

Throughout the thesis, the formation flying controller composed by the forward-in-time estimation approach presented in the previous section, together with a collision avoidance scheme (CAS) through artificial potential functions, will be denoted as State Estimation by Separation Principle with CAS, or simply SESP-CAS (Palacios et al., 2014). The SESP-CAS controller is defined first as a regulator problem and then as an estimation problem. It comprises a dynamical system composed by the state-space representation of the linearised SFF equations of motion, plus a nonlinear term which corresponds to the repelling accelerations generated by the CAS as defined previously in Chapter 3. This equation is repeated here for convenience together with an output equation:

$$\begin{aligned} \delta\dot{\boldsymbol{x}}(t) &= \mathbf{A}(t)\delta\boldsymbol{x}(t)+\mathbf{B}(t)\left[\boldsymbol{u}(t)+\boldsymbol{a}_R(t)\right] \\ \delta\boldsymbol{y}(t) &= \mathbf{C}(t)\delta\boldsymbol{x}(t) \end{aligned} \tag{4.18}$$

In this equation, the nonlinear (but possibly linear) function $\boldsymbol{a}_R(t) \in \mathbb{R}^3$ must be continuous, locally Lipschitz (Khalil, 1996) in $\delta\boldsymbol{x}(t) \in \mathbb{R}^6$, and introduces model uncertainty in the control through the CAS as defined in Eq. (3.26) in the previous chapter by (McInnes, 1993):

$$\boldsymbol{a}_R(t,\boldsymbol{x}) = 2A\exp\left[-\frac{1}{\sigma}\|\boldsymbol{x}-\boldsymbol{x}_o\|^2\right](\boldsymbol{x}-\boldsymbol{x}_o) \tag{4.19}$$

with amplitude defined as:

$$A = \frac{2\varepsilon_R\left(D+\|\boldsymbol{x}_o\|-\|\boldsymbol{\varrho}_D\|\right)}{6\exp(-3D)} \tag{4.20}$$

The matrix $\mathbf{C}(t) \in \mathbb{R}^{6\times6}$ and the vector $\boldsymbol{y}(t) \in \mathbb{R}^6$ can be used to model an incomplete measurement of the system state $\delta\boldsymbol{x}(t)$, including possibly all or some of its components. A Luenberger observer is then designed using Eq. (4.2) in order to estimate the states as:

$$\delta\dot{\hat{\boldsymbol{x}}}(t) = \mathbf{A}(t)\delta\hat{\boldsymbol{x}}(t) + \mathbf{B}(t)\boldsymbol{u}(t) - \mathbf{L}(t)\left[\mathbf{C}(t)\delta\hat{\boldsymbol{x}}(t) - \delta\boldsymbol{y}(t)\right] + \mathbf{B}(t)\boldsymbol{a}_R(t, \hat{\boldsymbol{x}}) \tag{4.21}$$

Then, using the separation principle, the observer system is fed by a closed-loop linear feedback control input $\boldsymbol{u}(t) \in \mathbb{R}^3$ defined as:

$$\boldsymbol{u}(t) = \mathbf{K}(t)\delta\hat{\boldsymbol{x}}(t) \tag{4.22}$$

where the Kalman gain $\mathbf{K}(t) \in \mathbb{R}^{3\times 6}$ is defined as in Eq. (4.11). Next, the matrices $\mathbf{L}(t) \in \mathbb{R}^{6\times 6}$ and $\dot{\mathbf{V}}(t) \in \mathbb{R}^{6\times 6}$ are used to solve the optimal control problem using Eq. (4.12), (4.13), (4.15), (4.16) and the procedure described in the previous section. Finally, the augmented controlled system is defined as:

$$\begin{aligned} \begin{Bmatrix} \delta\dot{\boldsymbol{x}}(t) \\ \delta\dot{\hat{\boldsymbol{x}}}(t) \end{Bmatrix} &= \begin{bmatrix} \mathbf{A}(t) & -\mathbf{B}(t)\mathbf{K}(t) \\ \mathbf{L}(t)\mathbf{C}(t) & \mathbf{A} + \mathbf{B}(t)\mathbf{K}(t) - \mathbf{L}(t)\mathbf{C}(t) \end{bmatrix} \begin{Bmatrix} \delta\boldsymbol{x}(t) \\ \delta\hat{\boldsymbol{x}}(t) \end{Bmatrix} \\ &+ \begin{Bmatrix} \mathbf{B}(t)\boldsymbol{a}_R(t, \boldsymbol{x}) \\ \mathbf{B}(t)\boldsymbol{a}_R(t, \hat{\boldsymbol{x}}) \end{Bmatrix} \end{aligned} \tag{4.23}$$

The control approach presented in this chapter is summarised in the diagram in Fig. (4.1) where the index *i* represents the current spacecraft and the index *obs* represent the signal containing information about all the obstacle-spacecraft. The algorithm to implement the controller in a numerical simulation can be defined as follows. During the offline process (on-ground process whose outputs may be uploaded at later time) the time vector, the initial values of the weight matrices, the initial values of DREs and the parameters of the repelling acceleration signal are defined. Next, for every spacecraft in the formation, the desired trajectory and the initial state are selected. Later, during the online process, the signal of the control input and the repelling accelerations are calculated for every element in the formation. Finally, the state of every spacecraft and the DREs are integrated simultaneously using a numerical integrator such as *ode45* in MATLAB. This control algorithm is presented in Table (4.1).

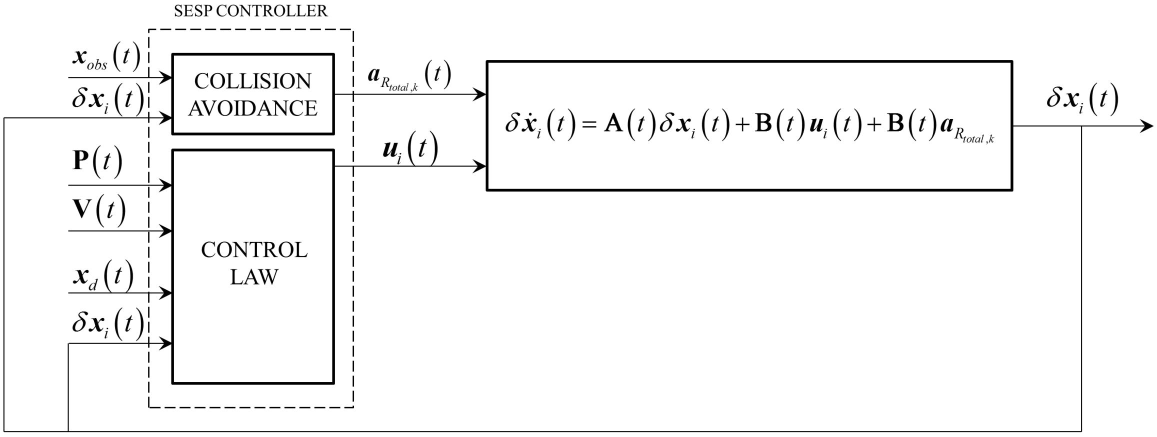

Fig. 4.1 Diagram of the control strategy

4.5 State and Model Uncertainty

In practice, in order to perform relative state estimation in formation flying, carrier-phase differential GPS (CDGPS) sensor measurements may be used. CDGPS techniques take the precise, but biased, Global Positioning System (GPS) carrier-phase measurements, resolve the biases through integer estimation techniques, and retain accurate information about the relative states of a pair of receivers. Despite CDGPS level of precision, the relative velocity measurements using this type of sensor are not accurate and, for example letting $\delta\boldsymbol{x}(t) = \begin{bmatrix} x & y & z & \dot{x} & \dot{y} & \dot{z} \end{bmatrix}^T$ in the $\mathcal{L}$ reference frame, even a small velocity measurement error in $\dot{y}(t)$ would result in considerable secular drift rates in the relative position, making fuel consumption an important consideration when sensor error is present during the manoeuvring (Gurfil, 2003). In this thesis, when using the SESP-CAS controller, we assume that velocity measurements of the state $\delta\boldsymbol{x}(t)$ are not available during the control process, simulating sensor uncertainty through the output matrix $\mathbf{C}(t)$ in Eq. (4.23) and tuning its influence on the system dynamics using the weight $\mathbf{W}_2(t)$.

On the other hand, model uncertainty is a function of the fidelity of the dynamical model used in the design of the controller (Alfriend et al., 2009). Despite the modelling of the space environment having reached considerably maturity, linear approximations are often used during control design in order to facilitate implementation and decrease computational load, and thus ignoring nonlinear terms, which may arise from perturbations such as gravity terms, atmospheric models, selection of thrust profiles, among others. Linearisation can, therefore, be an important source of model uncertainty in

Table 4.1 SESP-CAS control algorithm

```
OFFLLINE
1. Define the time vector $t$
2. Obtain the values of the weight matrices $\mathbf{Q}$, $\mathbf{R}$, $\mathbf{F}$, $\mathbf{W}_1$ and $\mathbf{W}_2$
3. Select the values of $\mathbf{P}(0)$ and $\mathbf{V}(0)$
4. Select the parameters of the repelling acceleration $\lambda$, $\sigma$ and $D$
5. For every spacecraft in the formation:
    a. Define the initial state and the desired trajectory
6. Incorporate each spacecraft state into a single state vector $\boldsymbol{x}(t)$
7. Incorporate each spacecraft desired state into a single desired state vector $\boldsymbol{x}_D(t)$
8. Obtain the state error vector $\delta\boldsymbol{x}(t)$
ONLINE
1. For every time step in the simulation and for every spacecraft in the formation:
    a. Obtain the signal of the repelling accelerations $\boldsymbol{a}_R(t)$
    b. Obtain the signal of the control input $\boldsymbol{u}(t)$
    c. Integrate, simultaneously, $\delta\dot{\boldsymbol{x}}(t)$, $\dot{\mathbf{P}}(t)$ and $\dot{\mathbf{V}}(t)$
```

state estimation. Given that Eq. (4.23) is composed by linear approximations and nonlinear terms to account for signals such as the ones generated by the CAS, model uncertainty is added during the control process and its influence during the dynamics process is adjusted through the weight $\mathbf{W}_1(t)$.

4.6 Simulations

To demonstrate the effectiveness of the SESP controller, three simulated scenarios are presented in the next subsections with the same features and parameters as the simulations carried out in Chapter 3. The proposed controller is implemented using the model in Eq. (4.23) together with the control law in Eq. (4.22) and the CAS in Eq. (4.19). It is assumed that no external perturbations, such as J_2 or atmospheric drag, affect the performance of the followers. Once more, the capabilities of the proposed controller are analysed in terms of values of total manoeuvre Δv and fuel consumption, calculated using Eq. (3.28) and (3.29) as defined in Chapter 3 with and without the effects of the CAS.

4.6.1 Scenario 1

This scenario simulates the on-orbit transfer of two Mango satellites with initial and final conditions as indicated in Table 4.2 and the reference orbit is defined as in Scenario 1 in Chapter 3.

Table 4.2 Initial and final conditions in Scenario 1

	MANGO 1	**MANGO 2**
Initial position (m)	$\begin{bmatrix} -15 & -50 & 0 \end{bmatrix}^T$	$\begin{bmatrix} 15 & -50 & 0 \end{bmatrix}^T$
Initial velocity (m/s)	$\begin{bmatrix} 0.35 & 0.35 & 0 \end{bmatrix}^T$	$\begin{bmatrix} -0.17 & 0.17 & 0 \end{bmatrix}^T$
Final position (m)	$\begin{bmatrix} -15 & 0 & 0 \end{bmatrix}^T$	$\begin{bmatrix} 15 & 0 & 0 \end{bmatrix}^T$
Final velocity (m/s)	$\begin{bmatrix} 0 & 0 & 0 \end{bmatrix}^T$	$\begin{bmatrix} 0 & 0 & 0 \end{bmatrix}^T$

In this scenario, the values of the controller gains are selected to be $\mathbf{Q} = \text{diag}[350]$, $\mathbf{R} = \text{diag}[1]$, $\mathbf{F} = \mathbf{Q}$, $\mathbf{W}_1 = \text{diag}[10]$ and $\mathbf{W}_2 = \text{diag}[250]$; $D = 5$ m and the nondimensional CAS parameters are chosen as $\lambda = -1 \times 10^{-4}$ and $\sigma = 1$. Moreover, the initial conditions for the DREs are selected as $\mathbf{P}(0) = \mathbf{V}(0) = \text{diag}[1]$ and the matrix $\mathbf{C}(t)$ is defined as:

$$\mathbf{C}(t) = \begin{bmatrix} \mathbf{1}_{3\times3} & \mathbf{0}_{3\times3} \\ \mathbf{0}_{3\times3} & \mathbf{0}_{3\times3} \end{bmatrix} \tag{4.24}$$

in order to assume the velocity is not available for measurement during the control process with and without CAS (whose influence is adjusted through the weight $\mathbf{W}_2$). The planar manoeuvre carried out by both satellites in the $x - y$ plane of the $\mathcal{L}$ frame with and without the CAS is shown in Fig. (4.2).

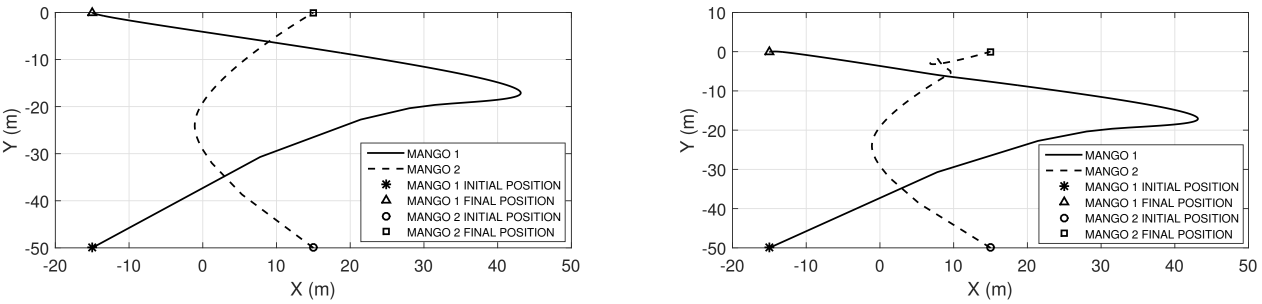

(a) Without CAS

(b) With CAS

Fig. 4.2 Manoeuvre trajectory in Scenario 1

The manoeuvre without the effects of the CAS is observed in Fig. (4.2a) where the follower trajectories approach each other until they generate a collision threat between them. When the CAS is active, as shown in Fig. (4.2b) with its corresponding selected parameters collision is avoided. It appears that their trajectories intersect again, however this occurs at different times and planes, as confirmed in Figure (4.3b), where the separation distance between the followers is shifted upwards, removing a potential collision risk during the manoeuvre, in contrast with Fig. (4.3a). This shift is also perceived in the error dynamics as indicated in Fig. (4.4a) in contrast with Fig. (4.4b), where the additional manoeuvring to avoid collision can be observed. Figure (4.5) shows the estimated error dynamics, influenced by the choice of $\mathbf{W}_1$ and $\mathbf{W}_2$, which displays a similar behaviour to the one previously obtained in Fig. (4.4).

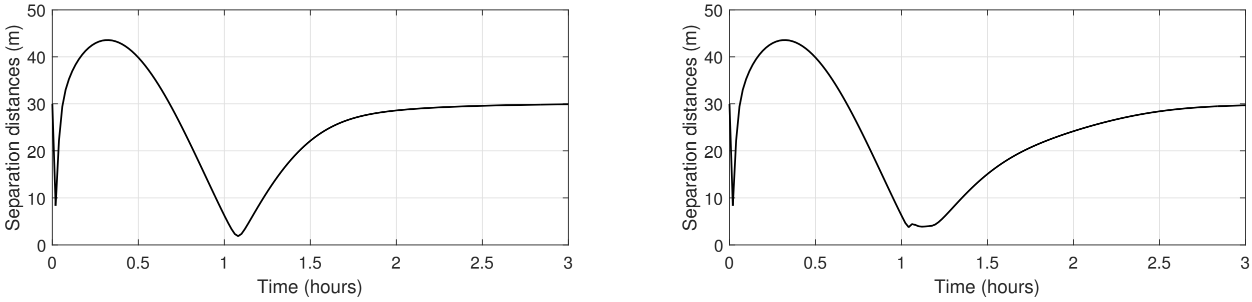

(a) Without CAS

(b) With CAS

Fig. 4.3 Separation distance in Scenario 1

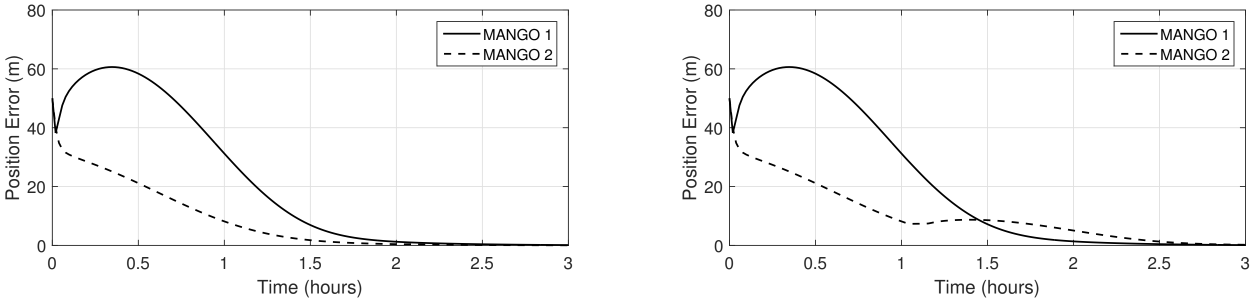

(a) Without CAS

(b) With CAS

Fig. 4.4 Magnitude of the position error in Scenario 1

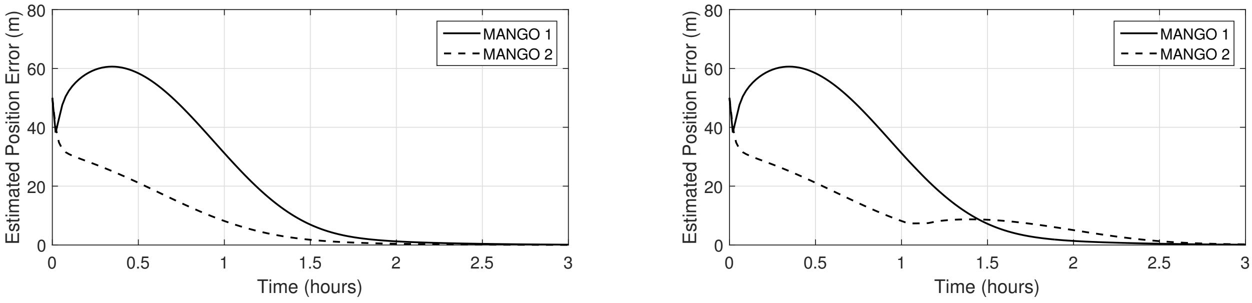

(a) Without CAS

(b) With CAS

Fig. 4.5 Magnitude of the estimated position error in Scenario 1

The similarity between these two error metrics indicates the estimation made by the SESP-CAS controller was satisfactory in terms of the performance obtained as if the whole state were available during the control process. The effects of spacecraft manoeuvring is likewise observable in the thrust profile as seen in Fig. (4.6), where an additional amount of thrust is required to perform the avoidance movement and the components of the total control input with CAS are depicted in Fig. (4.7).

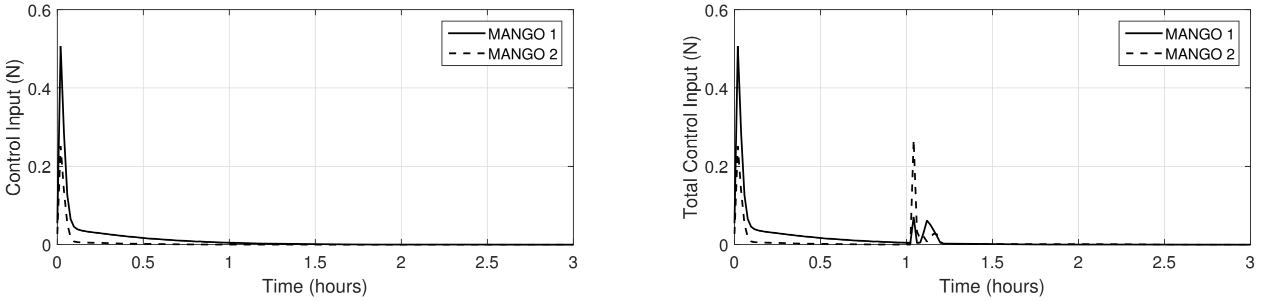

(a) Without CAS (b) With CAS

Fig. 4.6 Magnitude of the control input in Scenario 1

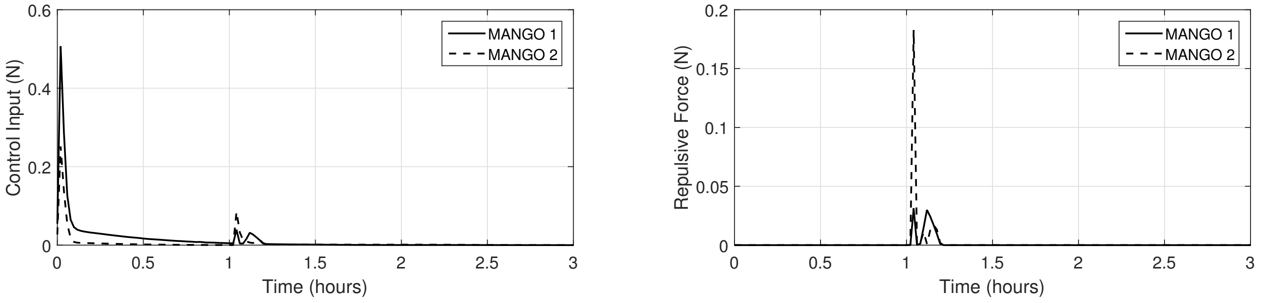

(a) (b)

Fig. 4.7 Components of the total control input with CAS in Scenario 1

As previously mentioned, the manoeuvring carried out by the followers also affect Δv and fuel consumption, as observed in Table (4.3), where different results are obtained with and without CAS. For instance, Mango 1 increases its total manoeuvre Δv and fuel consumption by 13%. The selection of the CAS parameters affects the performance of the controller. Considering the manoeuvre and results presented in this scenario, the tuning of the value of the parameter D and σ would produce a change in Δv and fuel consumption, as previously explained in Scenario 1 in Chapter 3. For instance, selecting a value of $D = 7$ decreases Δv and fuel consumption in Mango 1 by almost 5% and increases those parameters in Mango 2 by 2%, as observed in Table (4.4), while relevant plots are depicted in Fig (4.8). The selection of the parameter σ would also modify Δv and fuel consumption, for example, after selecting a value of $\sigma = 0.8$, Table (4.4) shows that Δv and fuel consumption in Mango 1 and 2 decrease by almost 8%, while pertinent plots to this σ value are presented in Fig (4.9).

Table 4.3 Summary of results for Scenario 1

	MANGO 1	**MANGO 2**	**TOTAL**
WITHOUT CAS			
Δv (m/s)	0.9	0.27	1.17
Fuel consumption (g)	62.86	19.00	81.86
Max. Thrust (N)	0.50	0.25	0.75
Final Position Error (m)	0	0	0
Final Velocity Error (m/s)	0	0	0
	MANGO 1	**MANGO 2**	**TOTAL**
WITH CAS			
Δv (m/s)	1.02	0.50	1.52
Fuel consumption (g)	71.24	35.15	106.39
Max. Thrust (N)	0.50	0.25	0.75
Final Position Error (m)	0	0	0
Final Velocity Error (m/s)	0	0	0
WITH CAS AND $\mathbf{C} = \text{diag}[1]$			
Δv (m/s)	1.01	0.49	1.5
Fuel consumption (g)	70.73	34.30	105.03
Max. Thrust (N)	0.50	0.25	0.75
Final Position Error (m)	0	0.01	0.01
Final Velocity Error (m/s)	0	0	0

Table 4.4 CAS parameters tune-up and corresponding Δv and fuel consumption. Each row represents a test case where the named parameter is set as specified, while the others are those defined in Scenario 1

	Δv (m/s)		**Fuel Consumption (g)**	
Parameter	**Mango 1**	**Mango 2**	**Mango 1**	**Mango 2**
$D = 7$ m	0.97	0.51	67.49	35.55
$\sigma = 2.5$	0.94	0.45	65.42	31.42

The selection of the weight matrices $\mathbf{W}_1(t)$ and $\mathbf{W}_2(t)$ also affects Δv and fuel consumption. In general, higher values of these weights allow the controller to better cope with model and sensor uncertainty, although at the expense of a higher control input $\boldsymbol{u}(t)$. For example, after selecting

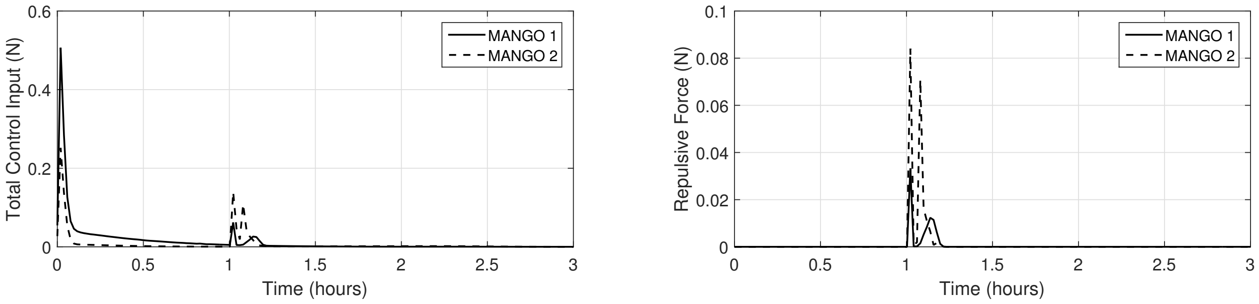

Fig. 4.8 Relevant plots with $D = 7$m in Scenario 1

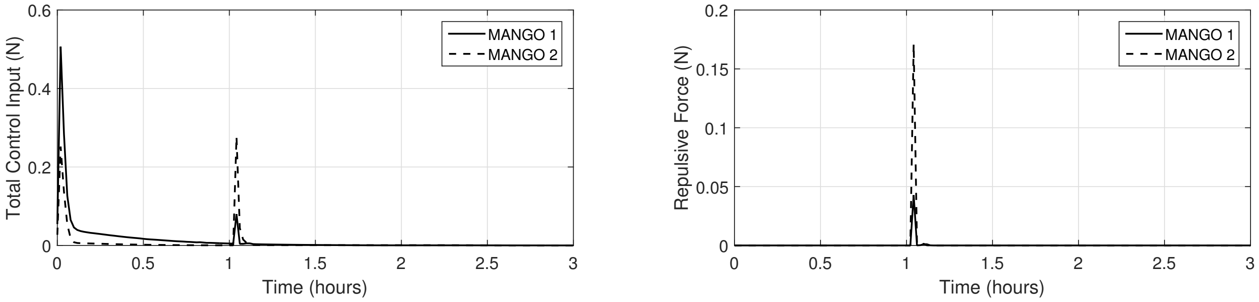

Fig. 4.9 Relevant plots with $\sigma = 0.8$ in Scenario 1

weight values of $\mathbf{W}_1(t) = \text{diag}[80]$ and $\mathbf{W}_2(t) = \text{diag}[350]$, Mango 1 and Mango 2 increase and fuel consumption by 3% and 12% respectively, as shown in Table (4.5).

Table 4.5 Weight matrices $\mathbf{W}_1(t)$ and $\mathbf{W}_2(t)$ tune-up and corresponding Δv and fuel consumption. Each row represents a test case where the named parameter is set as specified, while the others are those defined in Scenario 1

	Δv (m/s)		**Fuel Consumption (g)**	
Parameter	**Mango 1**	**Mango 2**	**Mango 1**	**Mango 2**
$\mathbf{W}_1(t) = \text{diag}[80]$ and $\mathbf{W}_2(t) = \text{diag}[350]$	1.05	0.56	73.03	39.05

One of the main differences between the controller presented in Chapter 3 and the SESP-CAS is that the later allows the spacecraft to follow a nominal trajectory in the presence of sensor uncertainty. This advantage allows the SESP-CAS to be applied to more realistic scenarios. In order to show the differences in terms of performance when assuming full state availability (FSA) and partial state availability (PSA), the same scenario with CAS is simulated once more but now assuming all states can be measured, with $\mathbf{C} = \text{diag}[1]$. The manoeuver execution using FSA is quite similar to that obtained with PSA with $\mathbf{C}$ as in Eq. (4.24), however, there are noticeable differences in terms of Δv

and fuel consumption. For instance, as observed in Table (4.3), the results obtained using FSA in terms of Δv and fuel consumption were 1% lower in comparison to those obtained with PSA. This decrease is expected since PSA-based controllers would require additional control input in order to carry out the estimation process.

4.6.2 Scenario 2

In this scenario, a manoeuvre with four Mango satellites, each located at one vertex of an imaginary square with side length of 20 m in the $y - z$ plane and centred at the origin of the $\mathcal{L}$ reference frame, with initial and final states as observed in Table (4.6), is simulated.

Table 4.6 Initial and final conditions in Scenario 2

	MANGO 1	**MANGO 2**	**MANGO 3**	**MANGO 4**
Initial position (m)	$\begin{bmatrix} 0 & -10 & 10 \end{bmatrix}^T$	$\begin{bmatrix} 0 & 10 & 10 \end{bmatrix}^T$	$\begin{bmatrix} 0 & 10 & -10 \end{bmatrix}^T$	$\begin{bmatrix} 0 & -10 & -10 \end{bmatrix}^T$
Initial velocity (m/s)	$\begin{bmatrix} 0 & 0 & 0 \end{bmatrix}^T$	$\begin{bmatrix} 0 & 0 & 0 \end{bmatrix}^T$	$\begin{bmatrix} 0 & 0 & 0 \end{bmatrix}^T$	$\begin{bmatrix} 0 & 0 & 0 \end{bmatrix}^T$
Final position (m)	$\begin{bmatrix} 0 & 10 & -10 \end{bmatrix}^T$	$\begin{bmatrix} 0 & -10 & -10 \end{bmatrix}^T$	$\begin{bmatrix} 0 & -10 & 10 \end{bmatrix}^T$	$\begin{bmatrix} 0 & 10 & 10 \end{bmatrix}^T$
Final velocity (m/s)	$\begin{bmatrix} 0 & 0 & 0 \end{bmatrix}^T$	$\begin{bmatrix} 0 & 0 & 0 \end{bmatrix}^T$	$\begin{bmatrix} 0 & 0 & 0 \end{bmatrix}^T$	$\begin{bmatrix} 0 & 0 & 0 \end{bmatrix}^T$

The objective of this manoeuvre, as in the previous chapter, is to swap positions diagonally while avoiding collision between the elements of the formation. The weight matrices are chosen as $\mathbf{Q} = \text{diag}[150]$, $\mathbf{R} = \text{diag}[1]$, $\mathbf{F} = \mathbf{Q}$, $\mathbf{W}_1 = \text{diag}[500]$ and $\mathbf{W}_2 = \text{diag}[650]$ with CAS parameters chosen as $D = 5$ m, $\lambda = -1.833 \times 10^{-9}$ and $\sigma = 2.5$ for all the spacecraft, while $\mathbf{C}(t)$ is defined as in Eq. (4.24) in order to demand full controller performance. The 3D manoeuvre is shown in Fig. (4.10).

When a collision avoidance action is taken, extra manoeuvring is observed, as in Fig. (4.10b), in contrast with the movement observed in Fig. (4.10a) without CAS. These avoidance actions affect other parameters. For instance, in Fig. (4.11), the separation distance between each spacecraft is plotted.

In Fig. (4.11a), it is also observed that without the CAS some spacecraft generate a collision threat, which vanishes when the CAS is activated as observed in Fig. (4.11b). These effects are also perceived in the error dynamics as indicated in Fig. (4.12), the estimated error dynamics in Fig. (4.13) and in the thrust behaviour as seen in Fig. (4.14). The components of the total thrust input obtained with the CAS, control input and repulsive force, are also observed in Fig. (4.15). The effects caused by the actions of the CAS are also perceived in Δv and fuel consumption, as seen in Table

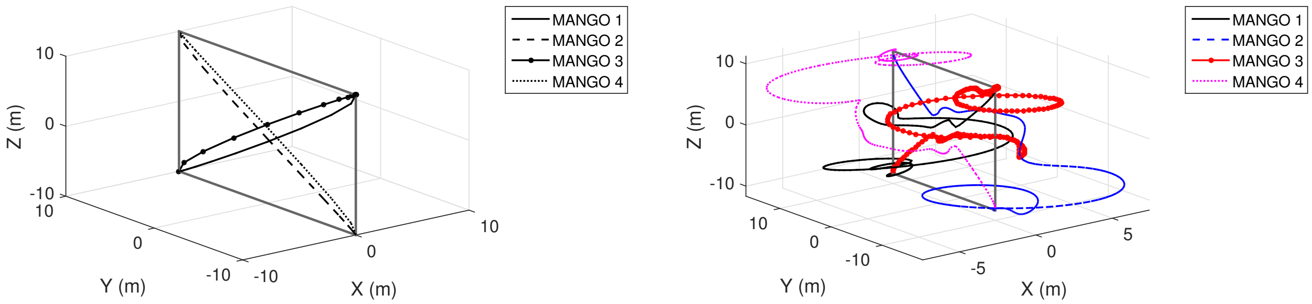

(a) Without CAS (b) With CAS

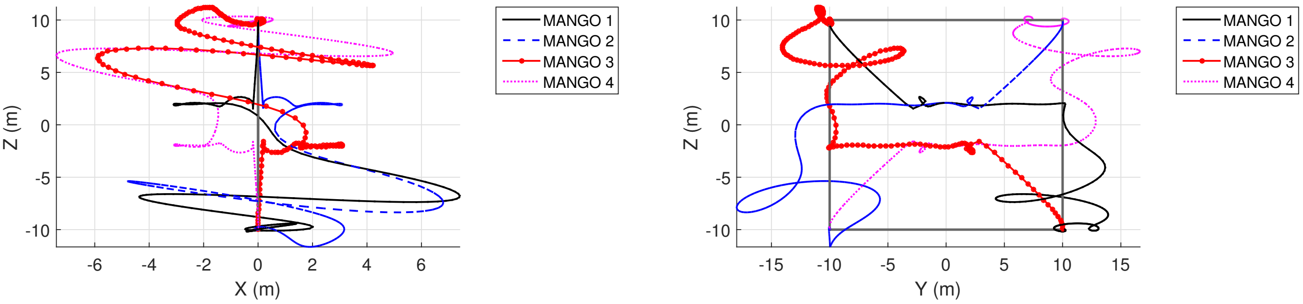

(c) X-Z Projection with CAS (d) Y-Z Projection with CAS

Fig. 4.10 Manoeuvre trajectory in Scenario 2

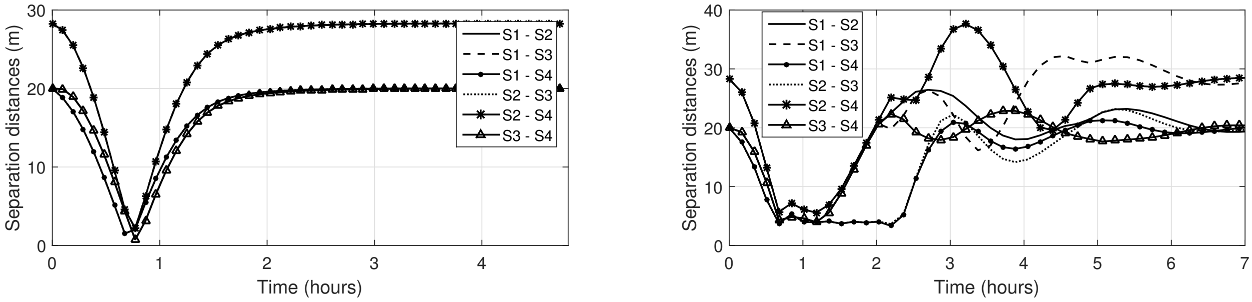

(a) Without CAS (b) With CAS

Fig. 4.11 Separation distance in Scenario 2

(4.7), for example, it can be seen that Mango 4 increased its Δv and fuel consumption 23 times with respect to those results obtained without the CAS.

4.6.3 Scenario 3

This scenario simulates a high-eccentricity on-orbit transfer of two Mango satellites using a reference orbit with an eccentricity value of 0.8, perigee altitude of 450 km and a period of 17.5 hours. The diagonal of the LQR gains are the same as in Scenario 1 and the CAS parameters are selected as $D = 5$m, $\lambda = 1.0 \times 10^{-9}$ and $\sigma = 8$, while $\mathbf{C}(t)$ is defined as in Eq. (4.24). Once more, the scenario is

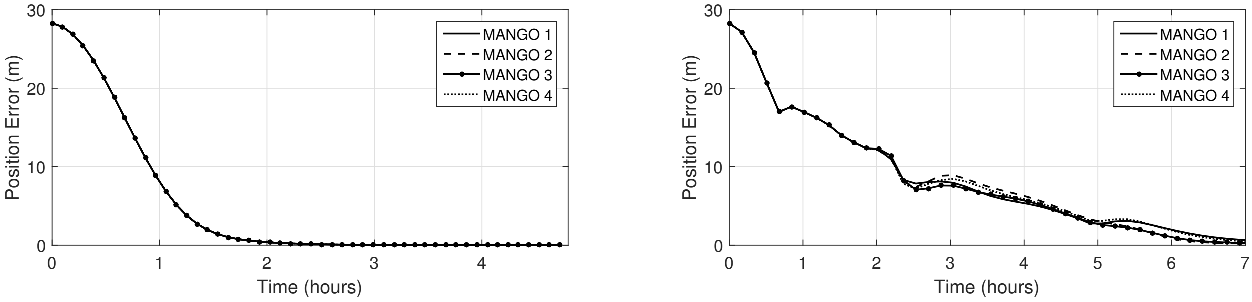

(a) Without CAS (b) With CAS

Fig. 4.12 Magnitude of the position error in Scenario 2

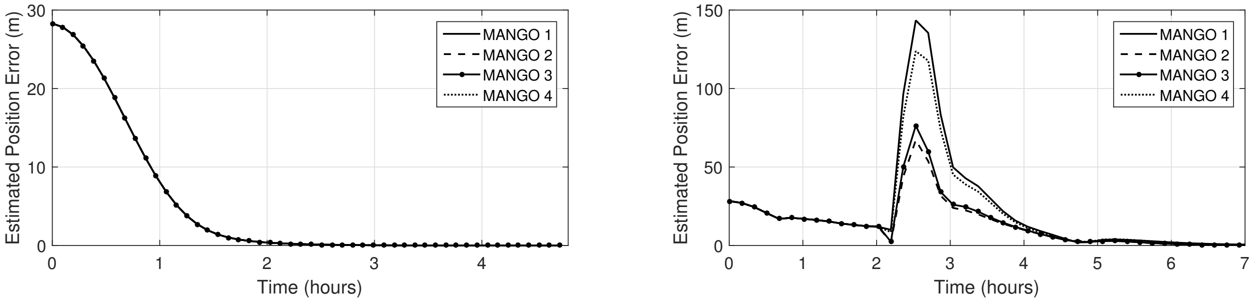

(a) Without CAS (b) With CAS

Fig. 4.13 Estimated magnitude of the position error in Scenario 2

simulated with and without the effects of the CAS and its results are then compared. The initial and final conditions are indicated in Table (4.8).

However, the final configuration is the same and the spacecraft have to interchange positions while generating a collision threat during the movement. The $x - y$ plane manoeuvre in the $\mathcal{L}$ frame is presented in Fig. (4.16) and it is observed in Fig. (4.16b) that extra manoeuvring is generated due to collision avoidance action, in contrast with the movement in Fig. (4.16a) obtained without the effects of the CAS.

These manoeuvring features caused by the CAS can also be observed in other measured parameters, for example, the separation distance is showed in Fig (4.17), where it is observed that some spacecraft generate a collision threat in Fig (4.17a), which vanishes when the CAS is activated in Fig. (4.17b).

Other parameters are the error dynamics in Fig (4.18), the estimated error dynamics in Fig (4.19), the thrust behaviour as seen in Fig (4.20) and the components of the total thrust input in Fig (4.21). The influence of the CAS in Δv and fuel consumption is observed in the results presented in Table (4.9) where, for example, it can be noticed that Mango 2 increased its Δv and fuel consumption 1.71 times with respect to the movement without CAS.

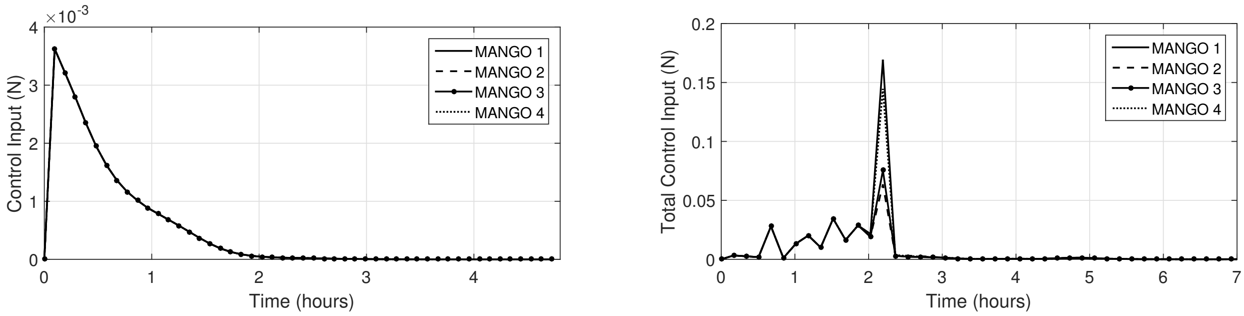

(a) Without CAS (b) With CAS

Fig. 4.14 Magnitude of the control input in Scenario 2

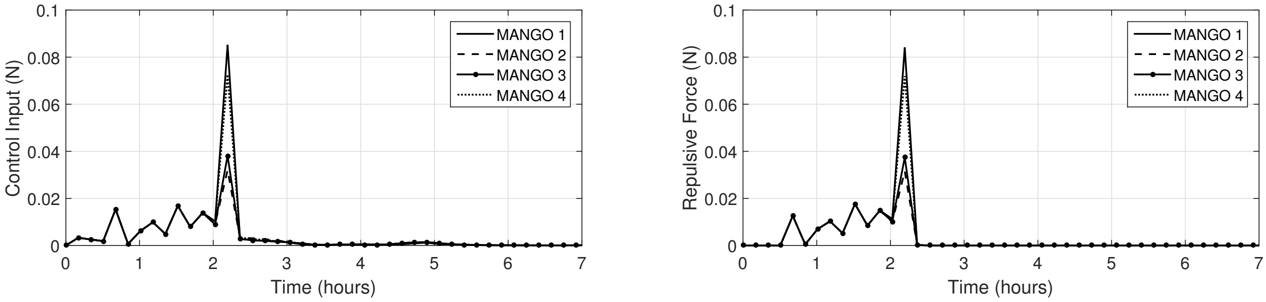

(a) (b)

Fig. 4.15 Components of the total control input with CAS in Scenario 2

4.7 Chapter Conclusions

In this chapter a control technique (SESP-CAS) involving guidance and collision avoidance for spacecraft formation flying, was designed using a state estimator based on the forward-in-time separation principle, and a collision avoidance scheme (CAS) from a Gaussian artificial potential function. The controller was implemented in several scenarios involving transfer manoeuvres and position swapping for spacecraft formation flying that included model and sensor uncertainty. In these scenarios, it was shown that the controller effectively tracked different nominal trajectories while model and sensor uncertainty was accounted for during the control process. Moreover, the CAS allowed to reduce the risk of collision between the followers during close-proximity manoeuvers. Total manoeuvre Δv and fuel consumption were also affected by the selection of the control weights and CAS parameters. For instance, in the cases where the CAS was active, an increase in these quantities was detected however, these increments were expected since the spacecraft required additional manoeuvring to perform collision avoidance, especially in those manoeuvers with higher collision risk. The accuracy in the error estimation capacities of the SESP-CAS depends on the appropriate selection of the values

Table 4.7 Summary of results for Scenario 2

WITHOUT CAS	**MANGO 1**	**MANGO 2**	**MANGO 3**	**MANGO 4**	**TOTAL**
Δv (m/s)	0.05	0.05	0.05	0.05	0.1
Fuel consumption (g)	4.02	4.02	4.02	4.02	16.08
Max. Thrust (N)	0.003	0.003	0.003	0.003	0.012
Final Position Error (m)	0	0	0	0	0
Final Velocity Error (m/s)	0	0	0	0	0
WITH CAS	**MANGO 1**	**MANGO 2**	**MANGO 3**	**MANGO 4**	**TOTAL**
Δv (m/s)	1.59	1.15	1.19	1.15	5.08
Fuel consumption (g)	110.88	80.58	83.31	80.58	355.35
Max. Thrust (N)	0.1	0.05	0.05	0.08	0.28
Final Position Error (m)	0.01	0.02	0.04	0.09	0.16
Final Velocity Error (m/s)	0	0	0	0	0

Table 4.8 Initial and final conditions in Scenario 3

	MANGO 1	**MANGO 2**
Initial position (m)	$\begin{bmatrix} -10 & 0 & 0 \end{bmatrix}^T$	$\begin{bmatrix} 10 & 0 & 0 \end{bmatrix}^T$
Initial velocity (m/s)	$\begin{bmatrix} 0.015 & 0 & 0 \end{bmatrix}^T$	$\begin{bmatrix} -0.015 & 0 & 0 \end{bmatrix}^T$
Final position (m)	$\begin{bmatrix} 10 & 0 & 0 \end{bmatrix}^T$	$\begin{bmatrix} -10 & 0 & 0 \end{bmatrix}^T$
Final velocity (m/s)	$\begin{bmatrix} 0 & 0 & 0 \end{bmatrix}^T$	$\begin{bmatrix} 0 & 0 & 0 \end{bmatrix}^T$

Table 4.9 Summary of results for Scenario 3

WITHOUT CAS	**MANGO 1**	**MANGO 2**	**TOTAL**
Δv (m/s)	0.1	0.14	0.188
Fuel consumption (g)	7.25	10.04	13.1
Max. Thrust (N)	0.01	0.01	0.02
Final Position Error (m)	0.01	0	0.01
Final Velocity Error (m/s)	0	0	0
WITH CAS	**MANGO 1**	**MANGO 2**	**TOTAL**
Δv (m/s)	0.32	0.24	0.56
Fuel consumption (g)	22.44	17.29	39.73
Max. Thrust (N)	0.01	0.01	0.02
Final Position Error (m)	0.03	0.04	0.07
Final Velocity Error (m/s)	0	0	0

of the weight matrices before the control process start. The average MATLAB simulation execution time per spacecraft for the forward integration of the Riccatti equations and the dynamics was 3.77 seconds with CAS and full sensor uncertainty. These time measurements suggests that this algorithm may be suitable for current on-board satellite computational capacities. As mentioned in Table 1.1,

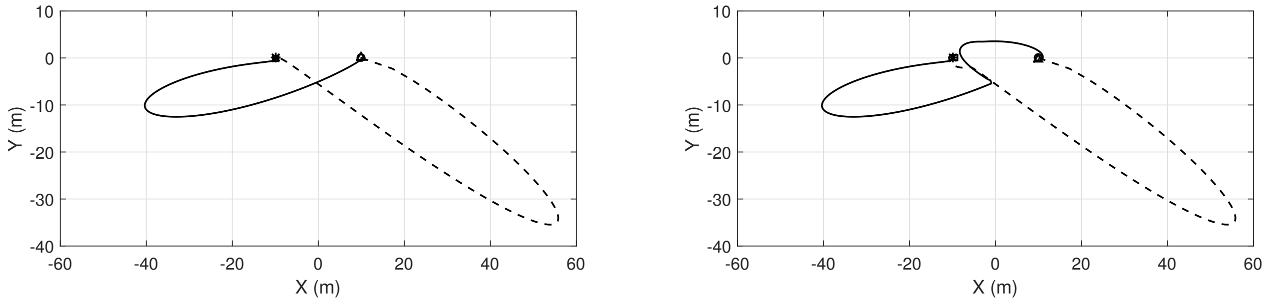

(a) Without CAS (b) With CAS

Fig. 4.16 Manoeuvre trajectory in Scenario 3

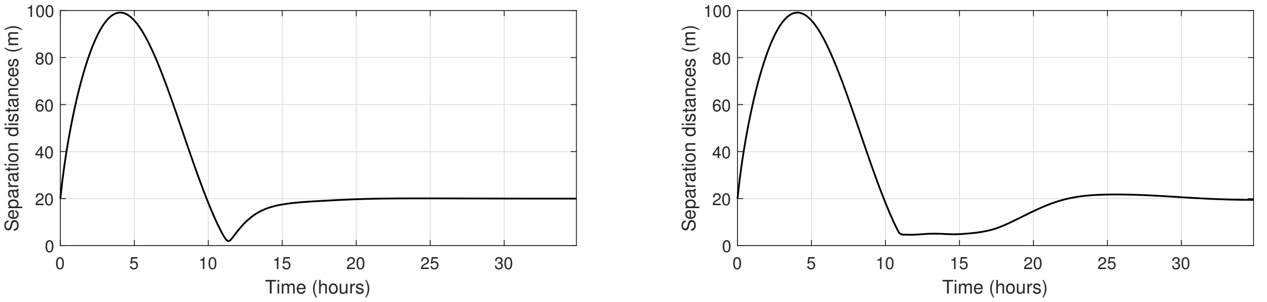

(a) Without CAS (b) With CAS

Fig. 4.17 Separation distance in Scenario 3

the propellant tank included in the spacecraft Mango of PRISMA mission contains about 5.6 kg of usable fuel and gives approximately 60 m/s Δv over the mission. Averaging the SESP-CAS Δv per spacecraft per manoeuvre we obtain a value of 0.95 m/s, which would allow a follower with the same fuel tanks features as Mango, to perform up to 63 manoeuvres. Strategies for online weights and dynamics parameters adaptation are not included in its framework. The capacity of a controller to automatically adjust system parameters could lead to improved performance and functionality, therefore, the next chapter presents a novel non-certainty equivalent adaptive control solution for spacecraft formation flying based on Immersion and Invariance paradigm.

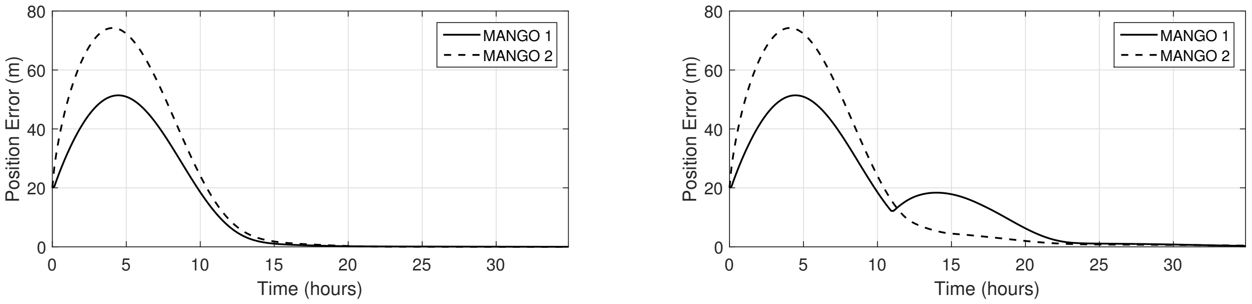

(a) Without CAS (b) With CAS

Fig. 4.18 Magnitude of the position error in Scenario 3

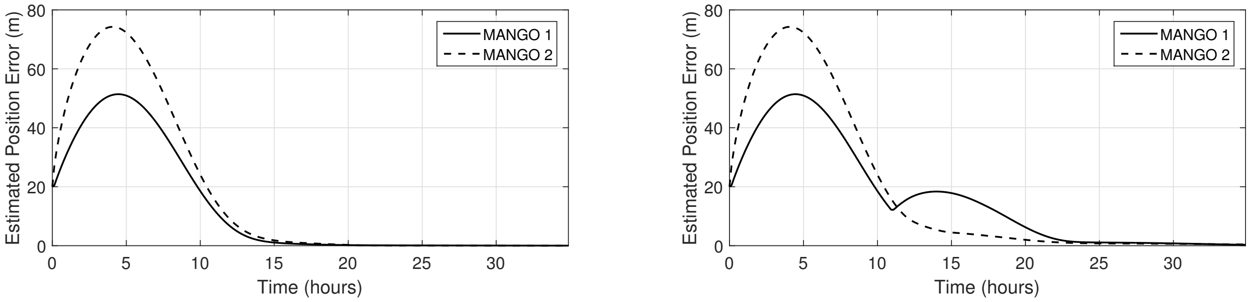

(a) Without CAS (b) With CAS

Fig. 4.19 Magnitude of the estimated position error in Scenario 3

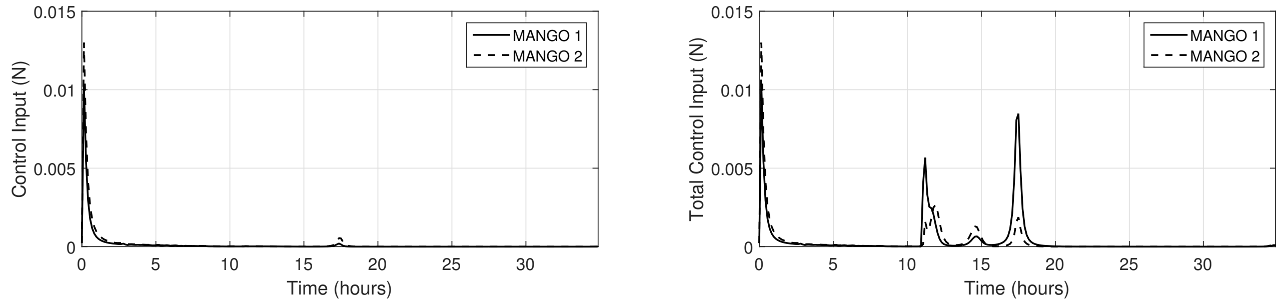

(a) Without CAS (b) With CAS

Fig. 4.20 Magnitude of the control input in Scenario 3

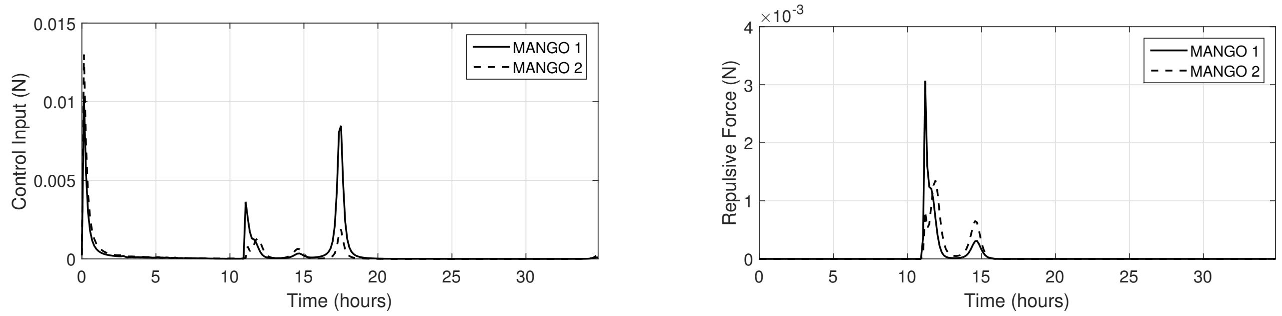

(a) (b)

Fig. 4.21 Components of the total control input with CAS in Scenario 3

Chapter 5

Spacecraft Formation Flying Control via Immersion and Invariance and Artificial Potential Functions

The contribution of this chapter is to apply, for the first time, the Immersion and Invariance adaptive approach developed in (Astolfi et al., 2008a) and (Seo and Akella, 2008) to close-manoeuvring control and collision-avoidance of spacecraft in formation (Palacios et al., 2015b). In general terms, this controller commands the dynamical performance of a follower with respect to a leader, by asymptotically tracking a time-varying nominal trajectory, while uncertainty in the modelling of perturbation forces is present and the risk of collision between the elements is eliminated. The performance of the controller is proven stable via a Lyapunov-based analysis and Barbalat's lemma. Simulated scenarios are presented in order to evaluate the performance of the controller and to show results in terms of Δv and fuel consumption, during close-proximity on-orbit transfer manoeuvres. This chapter starts by introducing the theory of Immersion and Invariance for nonlinear dynamical models in Section 5.1 as provided in (Astolfi et al., 2008a), which leads to the development of Immersion and Invariance adaptive tracking control for spacecraft formation flying from the mathematical framework developed in (Seo and Akella, 2008). The I&I theory presented in this section may be complemented with references (Astolfi and Ortega, 2003; Astolfi et al., 2008a). Section 5.2 and 5.3 present the design of the control strategy for spacecraft formation flying and its corresponding stability analysis. Finally, the performance of the proposed controller is evaluated in the simulated scenarios in Section 5.4 and conclusions are shown in Section 5.5.

5.1 Immersion and Invariance

The majority of current adaptive control frameworks are based on the certainty-equivalence (CE) principle (Lavretsky and Wise, 2013) however, CE adaptive controllers performance may be unacceptable in terms of the transient response of the closed-loop system because of the adaptation law in the parameter-estimation process, which acts like an additive disturbance imposed to the deterministic closed-loop control dynamics, wasting control effort and increasing fuel costs (Seo and Akella, 2008). The challenge is then to design an adaptive control law capable of delivering superior closed-loop performance when compared to current CE-based adaptive controllers. In this section, a novel method to design non-CE adaptive controllers for uncertain nonlinear systems is presented using the notions of system immersion and manifold invariance (Astolfi et al., 2008a). This control scheme known as Immersion and Invariance (Astolfi and Ortega, 2003) achieves stabilisation by immersing the plant dynamics into a target dynamical system (or manifold) that captures the desired dynamical behaviour. When uncertain parameters exist, the stabilisation approach is extended in order to add an adaptation law and this is called Immersion and Invariance Adaptive Control. The I&I methodology provides control laws that account for the effects of uncertain parameters, both internal and external, by adopting a robustness perspective. Its key feature is to add to the classical CE control approach a new term that, in conjunction with the parameter update law, is designed to achieve adaptive stabilisation. This parameter, called $\boldsymbol{\beta}(t)$ in this thesis, has the task of shaping the manifold into which the adaptive system is immersed (Astolfi et al., 2008b). In this section, the necessary control theory applied to a general dynamical system is presented. Then, in further sections, this is applied to formation flying. The I&I adaptive control problem is defined in general as follows (Astolfi and Ortega, 2003). Consider the general nonlinear dynamical system:

$$\dot{\boldsymbol{x}} = \boldsymbol{f}(\boldsymbol{x}) + \boldsymbol{g}(\boldsymbol{x})\boldsymbol{u}(t) \tag{5.1}$$

with $\boldsymbol{x}(t) \in \mathbb{R}^n$, the nominal trajectory $\boldsymbol{x}_D(t)$ to be stabilised, the generic dynamics function $\boldsymbol{f}(\boldsymbol{x})$ and the generic control matrix $\boldsymbol{g}(\boldsymbol{x})$ (notice that linear matrices such as $\mathbf{A}(t)$ and $\mathbf{B}(t)$ are not considered in this approach), which also depends on an uncertain or unknown parameter vector $\boldsymbol{\varepsilon} \in \mathbb{R}^q$ and the problem of finding, whenever possible, an adaptive state feedback control law $\boldsymbol{u}(t)$ of the form

(Astolfi et al., 2008a):

$$\begin{aligned} \dot{\hat{\boldsymbol{\varepsilon}}} &= \boldsymbol{w}\left(\boldsymbol{x}, \hat{\boldsymbol{\varepsilon}}\right) \\ \boldsymbol{u} &= \boldsymbol{\nu}\left(\boldsymbol{x}, \hat{\boldsymbol{\varepsilon}}\right) \end{aligned} \tag{5.2}$$

where $\hat{\boldsymbol{\varepsilon}}(t)$ is the estimation of $\boldsymbol{\varepsilon}$, such that all trajectories of the closed loop system in Eq. (5.1) and (5.2) are bounded and the $\lim_{t\to\infty} \boldsymbol{x}(t) = \boldsymbol{x}_D(t)$. For this purpose, it is usual to assume that a specific control law is known. For example, assume there is a function $\boldsymbol{\nu}\left(\boldsymbol{x}, \boldsymbol{\varepsilon}\right)$ such that the system:

$$\dot{\boldsymbol{x}} = \boldsymbol{f}(\boldsymbol{x}) + \boldsymbol{g}(\boldsymbol{x})\boldsymbol{\nu}\left(\boldsymbol{x}, \boldsymbol{\varepsilon}\right) \tag{5.3}$$

has a globally asymptotically stable equilibrium at $\boldsymbol{x}(t) = \boldsymbol{x}_D(t)$. Then, the I&I adaptive tracking control problem is defined as follows. The system in Eq. (5.1), considering the previous assumption on the control law, is said to be adaptively I&I stabilisable if there exist two functions $\boldsymbol{\beta}(\boldsymbol{x})$ and $\boldsymbol{w}\left(\boldsymbol{x}, \hat{\boldsymbol{\varepsilon}}\right)$ such that all trajectories of the extended system (Astolfi et al., 2008a):

$$\begin{aligned} \dot{\boldsymbol{x}} &= \boldsymbol{f}(\boldsymbol{x}) + \boldsymbol{g}(\boldsymbol{x})\boldsymbol{\nu}\left[\boldsymbol{x}, \hat{\boldsymbol{\varepsilon}} + \boldsymbol{\beta}(\boldsymbol{x})\right] \\ \dot{\hat{\boldsymbol{\varepsilon}}} &= \boldsymbol{w}\left(\boldsymbol{x}, \hat{\boldsymbol{\varepsilon}}\right) \end{aligned} \tag{5.4}$$

are bounded and satisfy (Astolfi et al., 2008a):

$$\lim_{t\to\infty} \left\{\boldsymbol{g}\left[\boldsymbol{x}(t)\right]\boldsymbol{\nu}\left[\boldsymbol{x}(t), \hat{\boldsymbol{\varepsilon}}(t) + \boldsymbol{\beta}(\boldsymbol{x})\right] - \boldsymbol{g}\left[\boldsymbol{x}(t)\right]\boldsymbol{\nu}\left[\boldsymbol{x}(t), \boldsymbol{\varepsilon}\right]\right\} = \boldsymbol{0} \tag{5.5}$$

Observe that for all trajectories staying on the manifold:

$$\mathcal{M} = \left\{(\boldsymbol{x}, \hat{\boldsymbol{\varepsilon}}) \in \mathbb{R}^n \times \mathbb{R}^q | \hat{\boldsymbol{\varepsilon}} - \boldsymbol{\varepsilon} + \boldsymbol{\beta}(\boldsymbol{x}) = \boldsymbol{0}\right\} \tag{5.6}$$

the condition in Eq. (5.5) holds. Moreover, adaptive I&I stabilisability (Astolfi and Ortega, 2003) implies that $\lim_{t\to\infty} \boldsymbol{x}(t) = \boldsymbol{x}_D(t)$. It is important to mention that, in general, the vector function $\boldsymbol{f}(\boldsymbol{x})$ and maybe $\boldsymbol{g}(\boldsymbol{x})$ depend on $\boldsymbol{\varepsilon}$ and, therefore, it is not necessary to require that $\hat{\boldsymbol{\varepsilon}}(t)$ converge to any particular equilibrium value.

5.2 Control Strategy

Throughout the thesis, the Immersion and Invariance adaptive control approach, as presented in (Seo and Akella, 2008), is applied to spacecraft formation flying for the first time, together with a collision avoidance scheme (CAS) through artificial potential functions. This new controller will be denoted as I&I-CAS (Palacios et al., 2015b). The I&I-CAS controller make use of the linearised SFF equations of motion (2.20) presented in Chapter 2, but multiplied by the mass of the follower $\mathbf{M} \in \mathbb{R}^{3\times3}$ in order to obtain force equations, plus the nonlinear terms corresponding to the effects of Earth oblateness $\boldsymbol{a}_J(t,\boldsymbol{x}) \in \mathbb{R}^3$, atmospheric drag $\boldsymbol{a}_D(t,\boldsymbol{x}) \in \mathbb{R}^3$ and repelling accelerations generated by the CAS $\boldsymbol{a}_R(t,\boldsymbol{x}) \in \mathbb{R}^3$. Next, this equation is presented using the tracking error approach as in Eq. (2.27) in Chapter 2:

$$\mathbf{M}\delta\ddot{\boldsymbol{x}}(t) = \mathbf{M}\mathbf{G}(t)\delta\dot{\boldsymbol{x}}(t) + \mathbf{M}\mathbf{H}(t)\delta\boldsymbol{x}(t) + \mathbf{M}\boldsymbol{u}(t) + \mathbf{M}\boldsymbol{a}_T(t,\boldsymbol{x}) \tag{5.7}$$

where $\boldsymbol{a}_T(t,\boldsymbol{x}) = \boldsymbol{a}_J(t,\boldsymbol{x}) + \boldsymbol{a}_D(t,\boldsymbol{x}) + \boldsymbol{a}_R(t,\boldsymbol{x})$. Next, a regression matrix $\mathbf{W}(t) \in \mathbb{R}^{3\times4}$ and a constant and unknown estimated parameter $\boldsymbol{\varepsilon} \in \mathbb{R}^4$ are defined as (Seo and Akella, 2008):

$$\mathbf{W}(t)\boldsymbol{\varepsilon} = \mathbf{M}\mathbf{G}(t)\delta\dot{\boldsymbol{x}}(t) + \mathbf{M}\mathbf{H}(t)\delta\boldsymbol{x}(t) + \mathbf{M}\boldsymbol{a}_T(t,\boldsymbol{x}) + \mathbf{M}\left[\alpha\kappa\delta\boldsymbol{x}(t) + \kappa\delta\dot{\boldsymbol{x}}(t)\right] \tag{5.8}$$

$$\boldsymbol{\varepsilon} = \begin{bmatrix} \varepsilon_M & \varepsilon_J & \varepsilon_D & \varepsilon_R \end{bmatrix}^T \tag{5.9}$$

where the estimated parameters correspond to the mass of the follower and the amplitude of the force signals for J_2, atmospheric drag and CAS, respectively. The meaning of the term $\alpha\kappa\delta\boldsymbol{x}(t) + \kappa\delta\dot{\boldsymbol{x}}(t)$ will be shown later during the development of the controller and the constant control parameters $\kappa \in \mathbb{R}$ and $\alpha \in \mathbb{R}$ are used to control the convergence rate of the position and velocity errors $\delta\boldsymbol{x}(t)$ and $\delta\dot{\boldsymbol{x}}(t)$. The system dynamics is, therefore, defined as:

$$\begin{aligned} \mathbf{M}\delta\ddot{\boldsymbol{x}}(t) \quad = \quad & \mathbf{M}\mathbf{G}(t)\delta\dot{\boldsymbol{x}}(t) + \mathbf{M}\mathbf{H}(t)\delta\boldsymbol{x}(t) + \mathbf{M}\boldsymbol{u}(t) + \mathbf{M}\boldsymbol{a}_T(t,\boldsymbol{x}) \\ & + \mathbf{M}\left[\alpha\kappa\delta\boldsymbol{x}(t) + \kappa\delta\dot{\boldsymbol{x}}(t)\right] - \mathbf{M}\left[\alpha\kappa\delta\boldsymbol{x}(t) + \kappa\delta\dot{\boldsymbol{x}}(t)\right] \end{aligned} \tag{5.10}$$

$$\delta\ddot{\boldsymbol{x}}(t) = \mathbf{M}^{-1}\left[\mathbf{W}(t)\boldsymbol{\varepsilon} + \mathbf{M}\boldsymbol{u}(t)\right] - \left[\alpha\kappa\delta\boldsymbol{x}(t) + \kappa\delta\dot{\boldsymbol{x}}(t)\right] \tag{5.11}$$

Linear filters are defined next for the control input, the state and the regression matrix as presented in (Seo and Akella, 2008):

$$\dot{\boldsymbol{u}}_f(t) = -\alpha \boldsymbol{u}_f(t) + \boldsymbol{u}(t) \in \mathbb{R}^3 \tag{5.12}$$

$$\dot{\boldsymbol{x}}_f(t) = -\alpha \boldsymbol{x}_f(t) + \delta\dot{\boldsymbol{x}}(t) \in \mathbb{R}^3 \tag{5.13}$$

$$\dot{\mathbf{W}}_f(t) = -\alpha \mathbf{W}_f(t) + \mathbf{W}(t) \in \mathbb{R}^{3\times 4} \tag{5.14}$$

After differentiating Eq. (5.13) with respect to time and substituting Eq. (5.11), the use of term $\alpha\kappa\delta\boldsymbol{x}(t) + \kappa\delta\dot{\boldsymbol{x}}(t)$ in Eq. (5.8) now results evident (Seo and Akella, 2008):

$$\begin{aligned} \delta\ddot{\boldsymbol{x}}_f(t) \quad = \quad & -\alpha\dot{\boldsymbol{x}}_f(t) + \mathbf{M}^{-1}\left[\dot{\mathbf{W}}_f(t) + \alpha\mathbf{W}_f(t)\right]\boldsymbol{\varepsilon} - \left[\alpha\kappa\delta\boldsymbol{x}(t) + \kappa\delta\dot{\boldsymbol{x}}(t)\right] \\ & + \mathbf{M}^{-1}\left[\dot{\boldsymbol{u}}_f(t) + \alpha\boldsymbol{u}_f(t)\right] \end{aligned} \tag{5.15}$$

This expression may be arranged as (Seo and Akella, 2008):

$$\begin{aligned} & \frac{d}{dt}\left[\dot{\boldsymbol{x}}_f(t) - \mathbf{M}^{-1}\mathbf{W}_f(t)\boldsymbol{\varepsilon} + \kappa\delta\boldsymbol{x}(t) - \mathbf{M}^{-1}\boldsymbol{u}_f(t)\right] \quad = \\ & -\alpha\left[\dot{\boldsymbol{x}}_f(t) - \mathbf{M}^{-1}\mathbf{W}_f(t)\boldsymbol{\varepsilon} + \kappa\delta\boldsymbol{x}(t) - \mathbf{M}^{-1}\boldsymbol{u}_f(t)\right] \end{aligned} \tag{5.16}$$

which is equivalent to the scalar expression:

$$\frac{d}{dt}\epsilon = -\alpha\epsilon \tag{5.17}$$

the integration of which leads to the result:

$$\epsilon = \epsilon_0 \exp\left(-\alpha t\right) \tag{5.18}$$

Therefore the rate of change of the state filter can be defined as:

$$\dot{\boldsymbol{x}}_f(t) = \mathbf{M}^{-1}\mathbf{W}_f(t)\boldsymbol{\varepsilon} - \kappa\delta\boldsymbol{x}(t) + \mathbf{M}^{-1}\boldsymbol{u}_f(t) + \boldsymbol{\epsilon}_0(t) exp\left(-\alpha t\right) \tag{5.19}$$

with:

$$\boldsymbol{\epsilon}(t_0) = \dot{\boldsymbol{x}}_f(t_0) - \mathbf{M}^{-1}\mathbf{W}_f(t_0)\boldsymbol{\varepsilon} + \kappa\delta\boldsymbol{x}(t_0) - \mathbf{M}^{-1}\boldsymbol{u}_f(t_0) \tag{5.20}$$

Next, it is assumed the filtered control signal $\boldsymbol{u}_f(t)$ and the estimation error $\boldsymbol{z}(t) \in \mathbb{R}^4$ are defined as (Seo and Akella, 2008):

$$\boldsymbol{u}_f(t) = -\mathbf{W}_f(t)\left[\boldsymbol{\varepsilon} + \boldsymbol{\beta}(t)\right] \tag{5.21}$$

$$\boldsymbol{z}(t) = \hat{\boldsymbol{\varepsilon}}(t) - \boldsymbol{\varepsilon} + \boldsymbol{\beta}(t) \tag{5.22}$$

where $\boldsymbol{\beta}(t) \in \mathbb{R}^4$ is defined as (Astolfi et al., 2008a; Seo and Akella, 2008):

$$\boldsymbol{\beta}(t) = \Gamma\mathbf{W}_f^T(t)\boldsymbol{x}_f(t) \tag{5.23}$$

and $\Gamma \in \mathbb{R}$ is a positive constant design parameter controlling its weight on the control process. In order to define the task of $\boldsymbol{\beta}(t)$, it is necessary first to obtain the following development. For the controller to perform appropriately, it is required that the closed-loop estimated error dynamics $\dot{\boldsymbol{z}}(t) \to \mathbf{0}$ as $t \to \infty$, therefore:

$$\begin{aligned}\dot{\boldsymbol{\beta}}(t) \;\; = \;\; & -\Gamma\mathbf{W}_f^T(t)\left[\alpha\boldsymbol{x}_f(t) + \mathbf{M}^{-1}\mathbf{W}_f(t)\boldsymbol{z}(t) + \kappa\delta\boldsymbol{x}(t) - \boldsymbol{\epsilon}_0(t)\exp\left(-\alpha t\right)\right] \\ & +\Gamma\mathbf{W}^T(t)\boldsymbol{x}_f(t)\end{aligned} \tag{5.24}$$

$$\dot{\hat{\boldsymbol{\varepsilon}}}(t) = \Gamma\mathbf{W}_f^T(t)\left[\alpha\boldsymbol{x}_f(t) + \kappa\delta\boldsymbol{x}(t)\right] - \Gamma\mathbf{W}^T(t)\boldsymbol{x}_f(t) \tag{5.25}$$

$$\dot{\boldsymbol{z}}(t) = -\Gamma\mathbf{W}_f^T(t)\left[\mathbf{M}^{-1}\mathbf{W}_f(t)\boldsymbol{z}(t) - \boldsymbol{\epsilon}_0(t)\exp\left(-\alpha t\right)\right] \tag{5.26}$$

where $\hat{\boldsymbol{\varepsilon}}(t) \in \mathbb{R}^4$. Now, the control input $\boldsymbol{u}(t) \in \mathbb{R}^3$ is defined using Eq. (5.12), (5.23), (5.24) and (5.25) as:

$$\boldsymbol{u}(t) = -\mathbf{W}(t)\left[\hat{\boldsymbol{\varepsilon}}(t) + \boldsymbol{\beta}(t)\right] - \Gamma\mathbf{W}_f(t)\mathbf{W}_f^T(t)\left[\kappa\delta\boldsymbol{x}(t) - \alpha\boldsymbol{x}_f(t) + \delta\dot{\boldsymbol{x}}(t)\right] \tag{5.27}$$

The term $\boldsymbol{\beta}(t)$ renders the closed-loop system composed by the Eq. (5.11), (5.25) and (5.27) input-to-state stable with respect to $\hat{\boldsymbol{\varepsilon}}(t) - \boldsymbol{\varepsilon}$ (Astolfi et al., 2008b). Implementing the I&I-CAS control scheme results in the control strategy formed by Eq. (5.8), (5.11), (5.25) and (5.27) together with the expressions for perturbations for J_2 $\boldsymbol{a}_J(t,\boldsymbol{x})$, atmospheric drag $\boldsymbol{a}_D(t,\boldsymbol{x})$ and the collision avoidance system (CAS) $\boldsymbol{a}_R(t,\boldsymbol{x})$, as defined in detail in Chapter 2 and 3. These perturbations and the CAS are presented here once more for convenience. The expression for $\boldsymbol{a}_J(t,\boldsymbol{x})$ is defined as:

$$\boldsymbol{a}_J(t,\boldsymbol{x}) = -\frac{\mu J_2 r_E^2}{2\|\boldsymbol{r}_F\|^5}\left\{6\left(\boldsymbol{r}_F\cdot\boldsymbol{k}\right)\boldsymbol{k} + \left[3 - \frac{15}{\|\boldsymbol{r}_F\|^2}\left(\boldsymbol{r}_F\cdot\boldsymbol{k}\right)^2\right]\boldsymbol{r}_F\right\} \tag{5.28}$$

where the vectors $\boldsymbol{r}(t)\in\mathbb{R}^3$ and $\boldsymbol{k}(t)\in\mathbb{R}^3$ may be expressed in $\boldsymbol{\mathcal{L}}$ coordinates as:

$$\boldsymbol{r}_F^{\mathcal{L}} = \begin{bmatrix}(r+x)\\ y\\ z\end{bmatrix} \quad \text{and} \quad \boldsymbol{k}^{\mathcal{L}} = \begin{bmatrix}s_\theta s_i\\ c_\theta s_i\\ c_i\end{bmatrix} \tag{5.29}$$

The expression for $\boldsymbol{a}_D(t,\boldsymbol{x})$ is represented as:

$$\boldsymbol{a}_D(t,\boldsymbol{x}) = -\frac{1}{2}\frac{C_D S\rho}{m_F}\left(\boldsymbol{v}-\boldsymbol{v}_{atm}\right)\|\boldsymbol{v}-\boldsymbol{v}_{atm}\| \tag{5.30}$$

with:

$$\boldsymbol{v}-\boldsymbol{v}_{atm} = \begin{bmatrix}\dot{r}+\dot{x}-y\omega-z\omega_E c_\theta s_i + y\omega_E c_i\\ r\omega+\dot{y}+x\omega-(r+x)\omega_E c_i + z\omega_E s_\theta s_i\\ \dot{z}-y\omega_E s_\theta s_i+(r+x)\omega_E c_\theta s_i\end{bmatrix} \tag{5.31}$$

and the expression for $\boldsymbol{a}_R(t,\boldsymbol{x})$ is:

$$\boldsymbol{a}_R(t,\boldsymbol{x}) = -\frac{\varepsilon_R\left(D+\|\boldsymbol{x}_o\|-\|\boldsymbol{\varrho}_D\|\right)}{6\exp(-3D)}\exp\left[-\frac{1}{\sigma}\|\boldsymbol{x}-\boldsymbol{x}_o\|^2\right]\left(\boldsymbol{x}-\boldsymbol{x}_o\right) \tag{5.32}$$

with amplitude:

$$A = \frac{\varepsilon_R\left(D+\|\boldsymbol{x}_o\|-\|\boldsymbol{\varrho}_D\|\right)}{6\exp(-3D)} \tag{5.33}$$

The I&I-CAS strategy is also illustrated in the diagram in Figure (5.1) and its corresponding implementation algorithm is summarized in Table (5.1). First, offline (on-ground process whose outputs may be uploaded at later time), define the time vector, the weight matrices and CAS parameters. Next, for every spacecraft in the formation, define the initial state and the desired trajectory. Determine the state error for every spacecraft and then incorporate them into a single state vector. During the online process, obtain the signal of the CAS and the control input for every spacecraft. The integration of the estimation state and the error state is then carried out simultaneously for all the spacecraft in the formation. Every spacecraft must have access to the position of the rest of the elements in the formation and its corresponding desired relative trajectory.

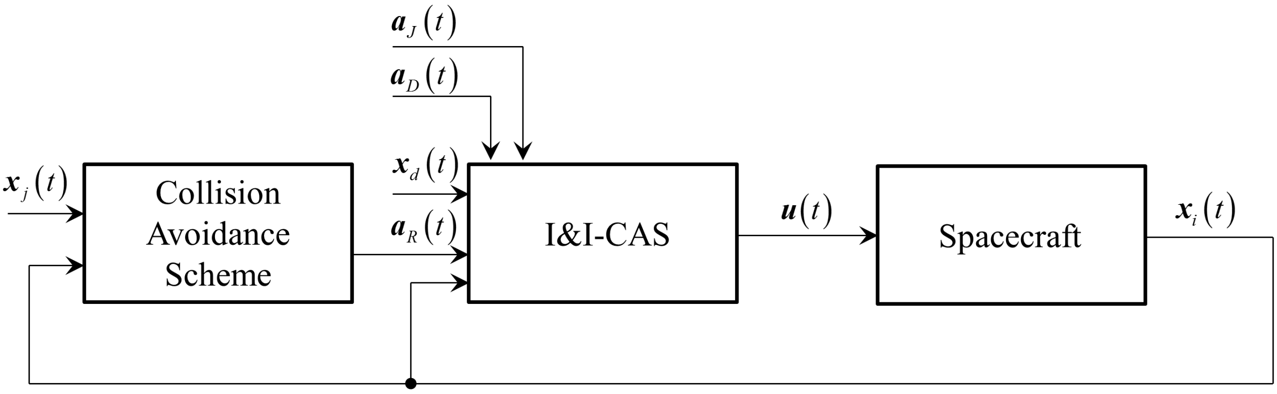

Fig. 5.1 Diagram of the control strategy

Table 5.1 I&I-CAS control algorithm

```
OFFLLINE
1. Define the time vector $t$
2. Obtain the values of the weight matrices $\alpha$, $\kappa$, $\Gamma$
3. Select the parameters of the repelling acceleration $\sigma$ and $D$
4. For every spacecraft in the formation:
    a. Define the initial state $\boldsymbol{x}(0)$ and the desired trajectory $\boldsymbol{x}_D(0)$
    b. Define the unknown parameter vector $\boldsymbol{\varepsilon}$
5. Incorporate each spacecraft state into a single state vector $\boldsymbol{x}(t)$
6. Incorporate each spacecraft desired state into a single desired state vector $\boldsymbol{x}_D(t)$
7. Obtain the state error vector $\delta\boldsymbol{x}(t)$
ONLINE
1. For every time step in the simulation and for every spacecraft in the formation:
    a. Obtain the signal of the repelling accelerations $\boldsymbol{a}_R(t)$
    b. Obtain the signal of the control input $\boldsymbol{u}(t)$
    c. Integrate, simultaneously, $\delta\dot{\boldsymbol{x}}(t)$ and $\dot{\hat{\boldsymbol{\varepsilon}}}(t)$
```

5.3 Stability Analysis of the Controller

The closed loop dynamics represented by Eq. (5.11) with the proposed control input in Eq. (5.27) and the adaptive estimation law in Eq. (5.25) ensure that the tracking error $\delta\boldsymbol{x}(t)$ is asymptotically stable. To prove this statement each one of the closed-loop signals affecting the control process will be analysed in terms of stability. First, consider the signal $\boldsymbol{\eta}(t) = \boldsymbol{\epsilon}(t)\exp(-\alpha t)$ and the Lyapunov function:

$$V(t) = \frac{1}{2}\boldsymbol{\eta}^T\boldsymbol{\eta} \tag{5.34}$$

for which the time derivative is:

$$\dot{V}(t) = \boldsymbol{\eta}^T\dot{\boldsymbol{\eta}} = -\alpha\|\boldsymbol{\eta}\|^2 \leq \mathbf{0} \tag{5.35}$$

Then, from Eq. (5.34) and (5.35) we can conclude that $\dot{V}(t)$ is negative semi-definite and therefore, $V(t)$ is monotonically decreasing and the signal $\boldsymbol{\eta}(t)$ is an $\mathscr{L}_2-$stable signal, or in other words, an asymptotically stable signal within the space of square-integrable Lebesgue measurable functions on $[0,\infty)$ (Haddad and Chellaboina, 2008; Marquez, 2003). The same analysis can be performed for the closed-loop signals $\boldsymbol{x}_f(t)$ and $\boldsymbol{z}(t)$. For instance, the following Lyapunov function is proposed for the filter $\boldsymbol{x}_f(t)$:

$$V(t) = \frac{1}{2}\boldsymbol{x}_f^T\boldsymbol{x}_f \quad \text{with} \quad \dot{V}(t) = -\boldsymbol{x}_f^T\left[\mathbf{M}^{-1}\mathbf{W}_f(t)\boldsymbol{z}(t) + \kappa\delta\boldsymbol{x}(t) - \boldsymbol{\eta}\right] \tag{5.36}$$

and for the estimated error $\boldsymbol{z}(t)$ the Lyapunov function is:

$$V(t) = \frac{1}{2}\boldsymbol{z}^T\boldsymbol{z} \quad \text{with} \quad \dot{V}(t) = -\boldsymbol{z}\Gamma\mathbf{W}_f^T(t)\left[\mathbf{M}^{-1}\mathbf{W}_f(t)\boldsymbol{z}(t) - \boldsymbol{\eta}\right] \tag{5.37}$$

Moreover, we can conclude by Barbalat's lemma (Haddad and Chellaboina, 2008; Khalil, 1996) that:

$$\lim_{t\to\infty}(\boldsymbol{\eta}, \boldsymbol{x}_f, \boldsymbol{z}) = \mathbf{0} \tag{5.38}$$

hence, from Eq. (5.13), the condition $\lim_{t\to\infty}\delta\boldsymbol{x}(t) = \mathbf{0}$ holds, which concludes the proof.

5.4 Simulations

To demonstrate the effectiveness of the I&I-CAS controller, three simulated scenarios are presented in the next subsections with similar features and parameters as in the previous chapters. The proposed controller is implemented using the model in Eq. (5.11) together with the control law in Eq. (5.27) and the perturbations in Eq. (5.28), (5.30) and (5.32). The capabilities of the proposed controller are analysed in terms of values of total manoeuvre Δv and fuel consumption, calculated using Eq. (3.28) and (3.29) as defined in Chapter 3, with and without the effects of the CAS and by selecting different values for the gain matrices of the controller.

5.4.1 Scenario 1

This scenario simulates the on-orbit transfer of two Mango satellites with initial and final conditions as indicated in Table (5.2).

Table 5.2 Initial and final conditions in Scenario 1

	MANGO 1	**MANGO 2**
Initial position (m)	$\begin{bmatrix} -15 & -50 & 0 \end{bmatrix}^T$	$\begin{bmatrix} 15 & -50 & 0 \end{bmatrix}^T$
Initial velocity (m/s)	$\begin{bmatrix} 0.35 & 0.35 & 0 \end{bmatrix}^T$	$\begin{bmatrix} -0.35 & 0.35 & 0 \end{bmatrix}^T$
Final position (m)	$\begin{bmatrix} 15 & 0 & 0 \end{bmatrix}^T$	$\begin{bmatrix} -15 & 0 & 0 \end{bmatrix}^T$
Final velocity (m/s)	$\begin{bmatrix} 0 & 0 & 0 \end{bmatrix}^T$	$\begin{bmatrix} 0 & 0 & 0 \end{bmatrix}^T$

The two Mango followers are initially located in the $x - y$ plane of the $\mathcal{L}$ reference frame and their initial velocities are chosen in such way that a collision threat is intentionally produced during the movement. The reference orbit has an eccentricity of 0.25, a perigee altitude of 450 km and the final simulation time is set to one orbital period of 2.4 hours. First, the scenario is simulated without the effects of the collision avoidance system (CAS) and its results in terms of Δv and fuel consumption are compared to those obtained when the CAS is active. Next, these results are obtained and compared once more using different values of the controller gains. The simulations are carried out selecting the control parameters as $\Gamma = 1$, $\kappa = 5$ and $\alpha = 10$ while the CAS parameters are selected to be $D = 5$ and $\sigma = 1$. In this scenario, it is assumed that there are uncertainties in the values the mass of the follower m_F and in factors included in the perturbations expressions, such as the multiplication of the elements $\mu J_2 r_E^2$ included in the expression of the acceleration $\boldsymbol{a}_J(t, \boldsymbol{x})$, the value obtained after multiplying the drag coefficient of the follower, the atmospheric pressure at the altitude of the reference orbit, the area of the follower $C_D S \rho$ included in the expression of the acceleration $\boldsymbol{a}_D(t, \boldsymbol{x})$ and the amplitude ε_R of the repelling acceleration $\boldsymbol{a}_R(t, \boldsymbol{x})$. Therefore, the components of the uncertain parameter vector are selected as:

$$\boldsymbol{\varepsilon} = \begin{bmatrix} \varepsilon_M & \varepsilon_J & \varepsilon_D & \varepsilon_R \end{bmatrix}^T = \begin{bmatrix} m_F & \mu J_2 r_E^2 & C_D S \rho & \varepsilon_R \end{bmatrix}^T \tag{5.39}$$

The numerical values for $m_F = 150$ kg, $S = 2.75$ m^2 and $C_D = 2.5$ of the follower are obtained from Table (1.1) in Chapter 1. The rest of the elements are selected as $r_E = 6378$ km, $J_2 = 1.08263 \times 10^{-3}$, $\mu = 398,600$ km^3/s^2, $\rho = 1 \times 10^{-12}$ kg/m^3 and $\varepsilon_R = 1 \times 10^{-6}$ is obtained from previous simulations (Palacios et al., 2014, 2015a), while the initial value of the estimation vector is selected as half of the uncertain vector $\hat{\boldsymbol{\varepsilon}}(0) = 1/2\boldsymbol{\varepsilon}$. The planar manoeuvres, without the effects of the CAS, are observed in Figure (5.2a) where the followers' trajectories approach each other until, eventually, they intersect generating a collision.

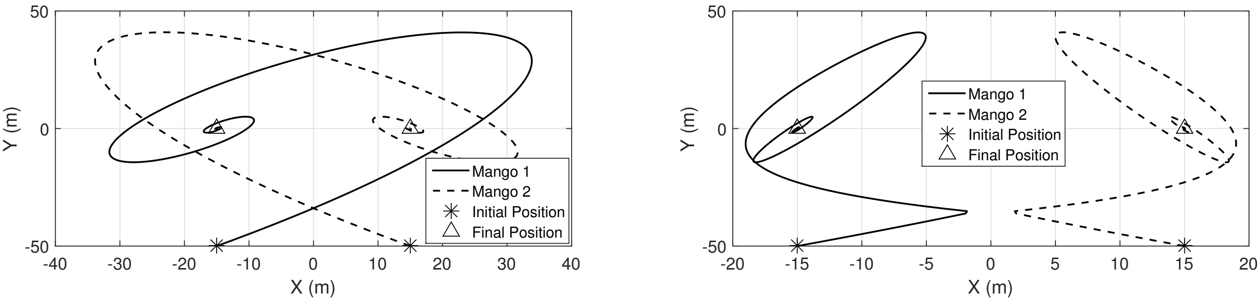

(a) Without CAS (b) With CAS

Fig. 5.2 Manoeuvre trajectory in Scenario 1

This is not the case when the CAS is acting on them; as can be seen in Figure (5.2b), where the trajectories initially approach each other and then are repelled by the effects of the CAS and this repelling manoeuvre is confirmed in Figure (5.3), where the separation distance between the followers is presented.

In Figure (5.3a) the collision threat can be noticed since the separation distance between the followers decrease to almost zero during the first instants of the movement, while in Figure (5.3b) the CAS effectively shifts this collision threat upwards. In both cases, with and without CAS, the

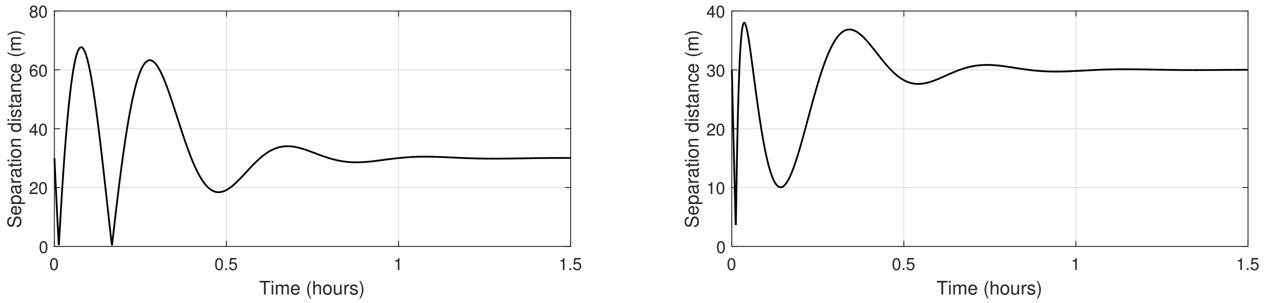

(a) Without CAS (b) With CAS

Fig. 5.3 Separation distance in Scenario 1

proposed controller effectively guide the followers toward the desired final positions and velocities. The position tracking error of the followers without the effects of the CAS is observed in Figure (5.4a) where the final position is reached in approximately 1 hour.

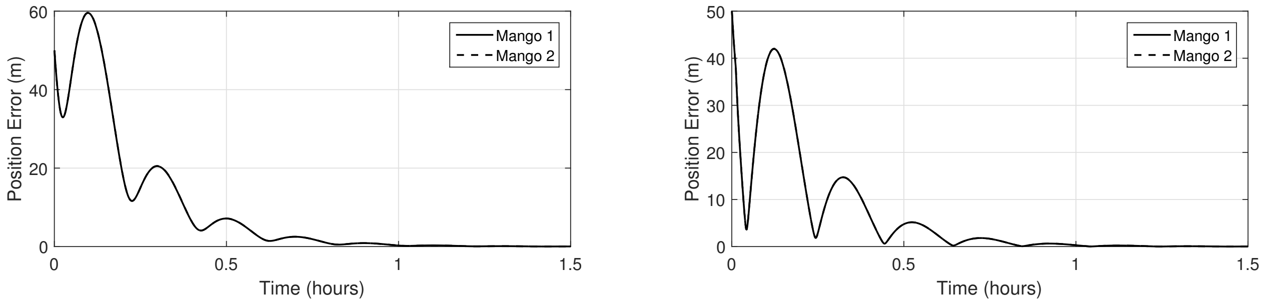

(a) Without CAS (b) With CAS

Fig. 5.4 Magnitude of the position error in Scenario 1

On the other hand, in Figure (5.4b), the position tracking error norm is presented including the effects of the CAS showing additional manoeuvring carried out by the followers, compared to that without CAS, in order to avoid collision between each other. Figure (5.5) shows the norm of the control input provided by the controller with and without collision avoidance.

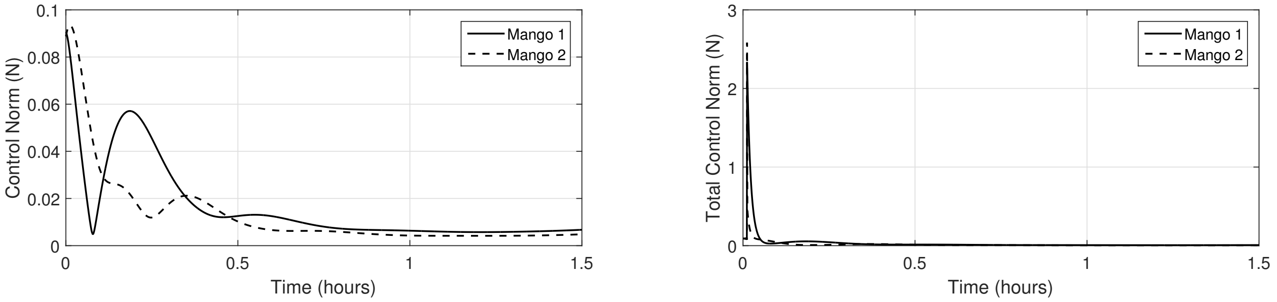

(a) Without CAS (b) With CAS

Fig. 5.5 Magnitude of the control input in Scenario 1

It is observed, in Figure (5.5a), that a maximum control force value of 0.09 N is provided during the transient response of the manoeuvre by both followers, until a constant value is reached during the steady state. When the CAS is active, the maximum control input value, corresponding now to Mango 2, increases to 2.58 N during the transient response, as seen in Fig. (5.5b), showing that additional control input is required by both followers during the avoidance actions. Also, as observed in Fig. (5.6), the total control input with CAS has two components, the control input used to track the desired trajectory and the repulsive force used for collision avoidance.

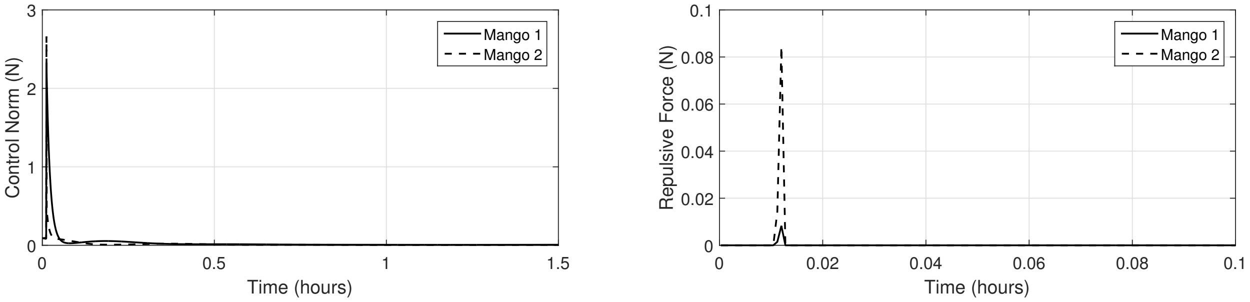

(a) (b)

Fig. 5.6 Components of the total control input with CAS in Scenario 1

During the simulation without CAS, the controller estimated only the values of the uncertain parameters ε_M, ε_J and ε_D. It can be noticed that these parameters show an adaptive behaviour, starting from their initial value and passing through the transient response, until stable constant values are found by the controller in the steady state, as observed in Fig. (5.7). Also observe in this Figure that the differences in the non-dimensional parameters is due to the estimation process, which also depends on the signal of the reference trajectory, which is different for every follower. When the CAS is active, the four uncertain parameters are now estimated for both Mango satellites, as observed in Figure (5.8).

As in the case without CAS, the estimated parameters also showcase an adaptive behaviour during the first instants of the manoeuvre, until the controller finally finds steady final values. It can also be noticed that the parameters converged at similar times for both spacecraft. The collision avoidance manoeuvres performed by the followers have an effect on Δv and fuel consumption, as observed in Table (5.3). For instance, Mango 2 increases its total manoeuvre Δv and fuel consumption by 20%. Additionally, the tuning the CAS parameters also has implications in the performance of the

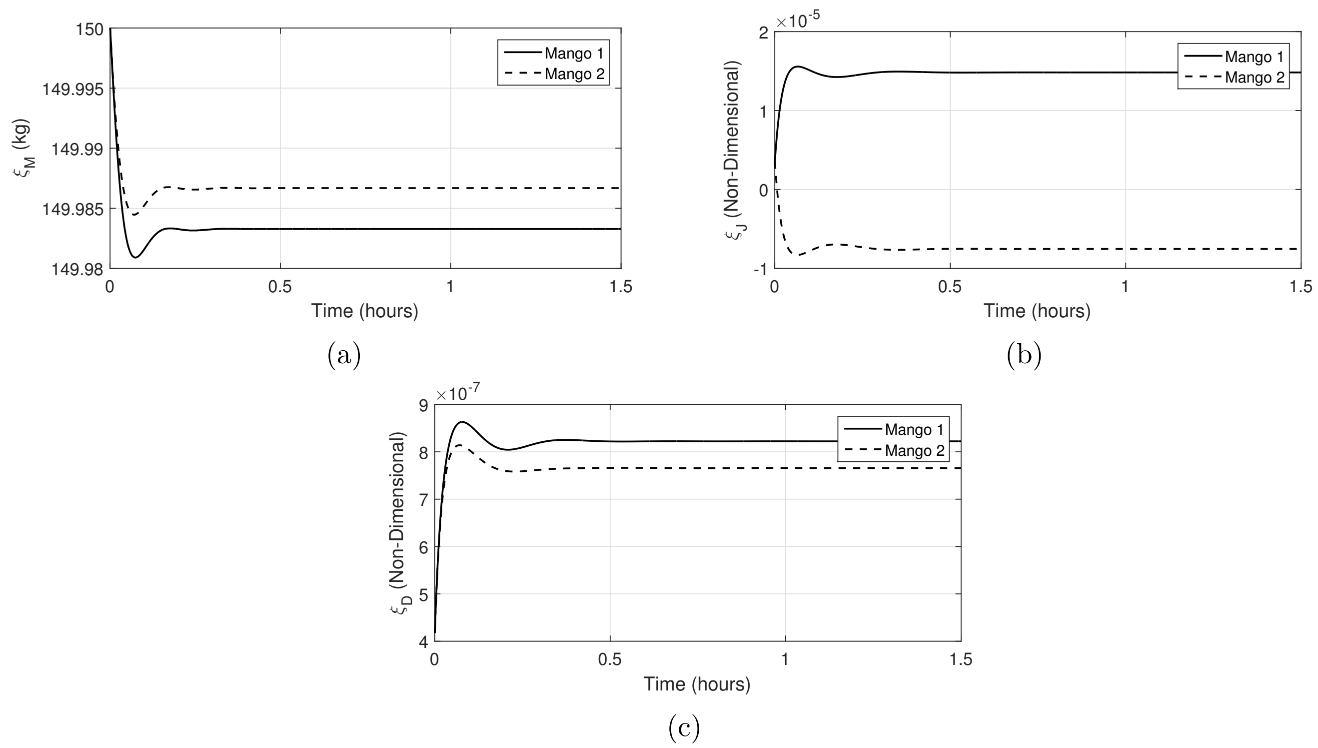

(a) (b) (c)

Fig. 5.7 Estimated parameters without CAS in Scenario 1

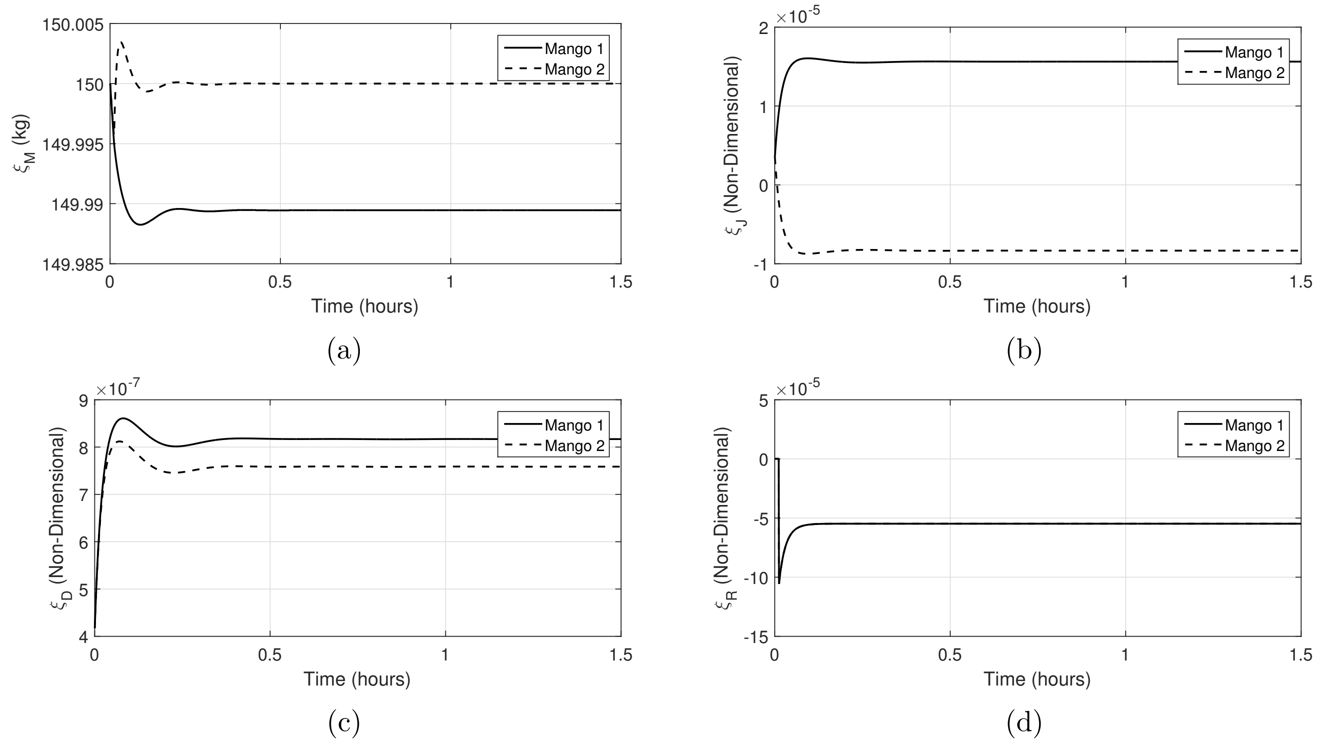

(a) (b) (c) (d)

Fig. 5.8 Estimated parameters with CAS in Scenario 1

spacecraft. For instance, selecting a value of $D = 6$ m increases Δv and fuel consumption in Mango 1 by almost 1% as observed in Table (5.4), while relevant plots are depicted in Fig (5.9).

Table 5.3 Summary of results for Scenario 1

WITHOUT CAS	**MANGO 1**	**MANGO 2**	**TOTAL**
Δv (m/s)	0.58	0.47	1.05
Fuel consumption (g)	40.81	32.72	73.53
Max. Thrust (N)	0.09	0.09	0.18
Final Position Error (m)	0.02	0.02	0.04
Final Velocity Error (m/s)	0	0	0
WITH CAS	**MANGO 1**	**MANGO 2**	**TOTAL**
Δv (m/s)	1.17	0.57	1.74
Fuel consumption (g)	81.81	40.29	122.1
Max. Thrust (N)	2.33	2.58	4.91
Final Position Error (m)	0.02	0.02	0.04
Final Velocity Error (m/s)	0	0	0

Table 5.4 CAS parameters tune-up and corresponding Δv and fuel consumption. Each row represents a test case where the named parameter is set as specified, while the others are those defined in Scenario 1

	Δv (m/s)		**Fuel Consumption (g)**	
Parameter	**Mango 1**	**Mango 2**	**Mango 1**	**Mango 2**
$D = 6$ m	1.18	0.57	82.02	39.68
$\sigma = 6$	1.39	0.93	97.18	65.26

Also, after selecting a value of $\sigma = 6$ it can be noticed in Table (5.4) that Δv and fuel consumption in Mango 1 increase by 18%, while pertinent plots to this σ value are presented in Fig (5.10). The selection of the parameters Γ, κ and α also affects Δv and fuel consumption. In general, higher values of these weights allow the error dynamics to converge faster toward zero, although at the expense of a higher control input $\boldsymbol{u}(t)$. The parameter Γ allows to tune the convergence rate toward the desired trajectory and larger values of this parameter will make this convergence faster. For example, after selecting $\Gamma = 10$, the error position plot in Fig (5.11) and a faster convergence to zero is observed compared to the error position plot obtained with $\Gamma = 1$. The selection of Γ also affects Δv and fuel consumption as noticed in Table (5.5) where, for example, Δv is four times larger than the simulation with $\Gamma = 1$ for Mango 1. The parameter κ also affects the performance of the followers, for instance, after selecting $\kappa = 10$, Δv in Mango 2 increases by 20%, as observed in Table (5.5). The same applies

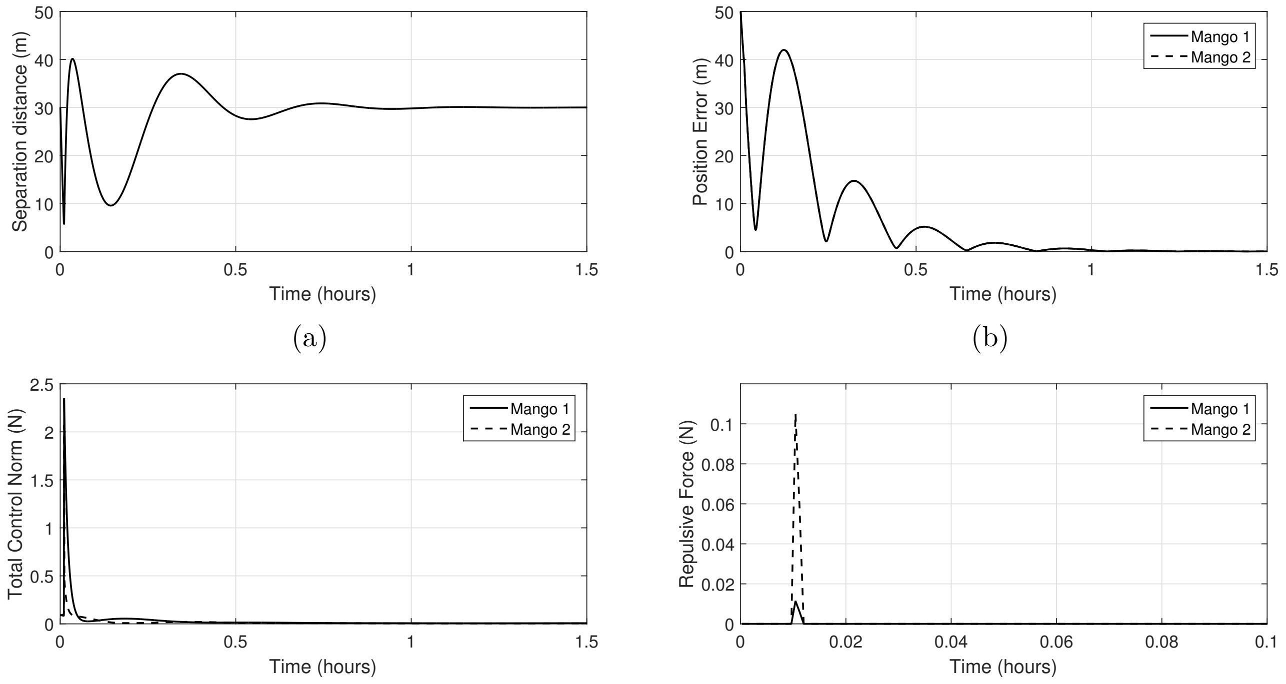

(a) (b)

(c) (d)

Fig. 5.9 Relevant plots with $D = 6$ m in Scenario 1

to the parameter α and after selecting $\alpha = 15$, a decrease in Δv of 5% is perceived in Mango 2, as observed in Table (5.5).

Table 5.5 Weight matrices tune-up and corresponding Δv and fuel consumption. Each row represents a test case where the named parameter is set as specified, while the others are those defined in Scenario 1

	Δv (m/s)		**Fuel Consumption (g)**		**Max. Thrust (N)**	
Parameter	**Mango 1**	**Mango 2**	**Mango 1**	**Mango 2**	**Mango 1**	**Mango 2**
$\Gamma = 10$	4.69	4.46	326.16	310.13	0.38	0.36
$\kappa = 10$	0.86	0.69	60.25	48.53	1.25	12.24
$\alpha = 15$	1.03	0.54	72.04	37.96	3.38	7.79

5.4.2 Scenario 2

In this scenario, a manoeuvre with four Mango satellites, each located at one vertex of an imaginary square with side length of 20 m in the $y - z$ plane and centred at the origin of the $\mathcal{L}$ reference frame, with initial and final states as observed in Table (5.6) is simulated.

The objective of this scenario, as in previous chapters, is to swap positions diagonally while avoiding collisions between the elements of the formation. The control parameters are chosen as

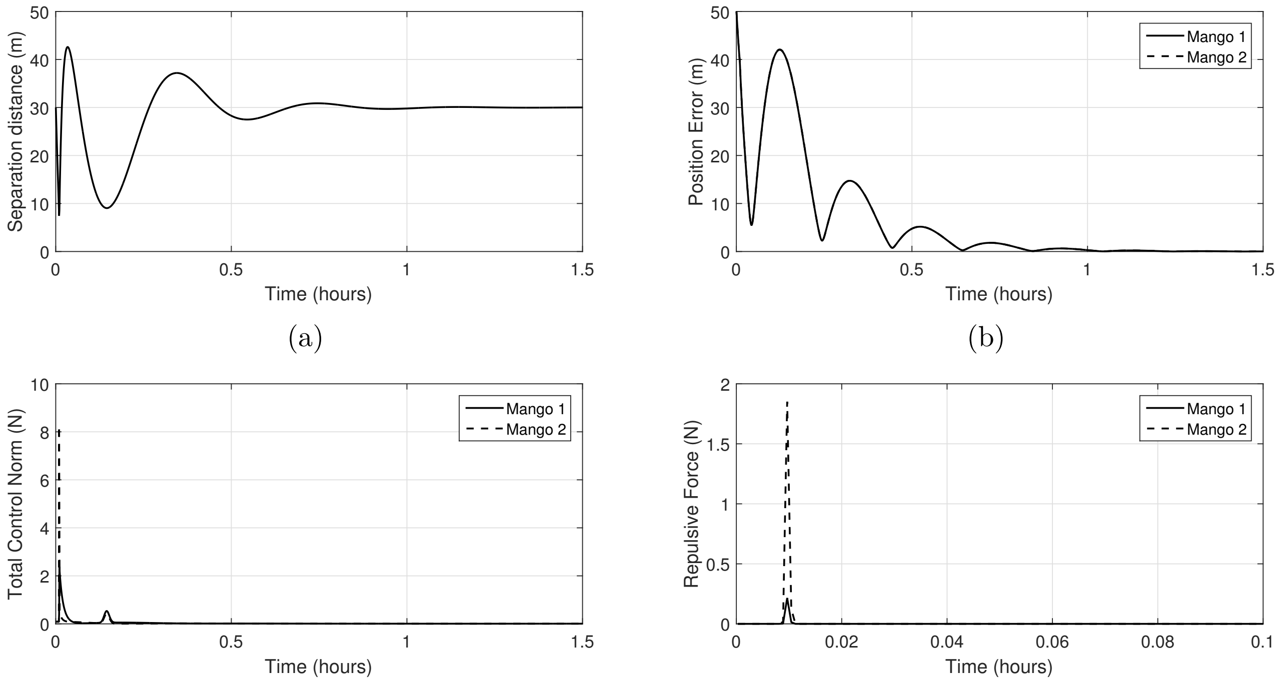

(a) (b)

(c) (d)

Fig. 5.10 Relevant plots with $\sigma = 6$ in Scenario 1

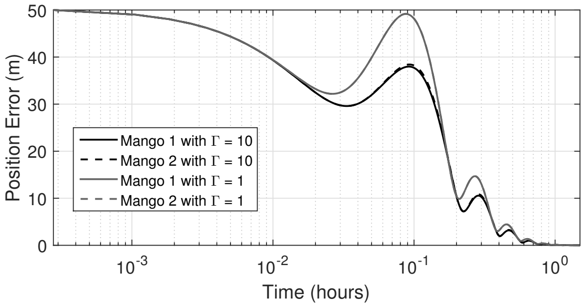

Fig. 5.11 Relevant plots with $\Gamma = 10$ in Scenario 1

$\Gamma = 1$, $\kappa = 5$ and $\alpha = 10$ with CAS parameters selected as $D = 5$ m and $\sigma = 1$, for all the spacecraft. The 3D manoeuvre is shown in Fig. (5.12).

When a collision avoidance action is taken, extra manoeuvring is observed, as in Fig. (5.12b), in contrast with the movement observed in Fig. (5.12a) without CAS. These avoidance actions have an effect on the performance parameters. For instance, in Fig. (5.13), the separation distance between each spacecraft is plotted.

In Fig. (5.13a), it is also observed that without the CAS some spacecraft generate collisions, but this threat is removed when the CAS is activated as observed in Fig. (5.13b). These effects are also perceived in the error dynamics as indicated in Fig. (5.14) and in the thrust behaviour as seen in Fig.

Table 5.6 Initial and final conditions in Scenario 2

	MANGO 1	**MANGO 2**	**MANGO 3**	**MANGO 4**
Initial position (m)	$\begin{bmatrix} 0 & -10 & 10 \end{bmatrix}^T$	$\begin{bmatrix} 0 & 10 & 10 \end{bmatrix}^T$	$\begin{bmatrix} 0 & 10 & -10 \end{bmatrix}^T$	$\begin{bmatrix} 0 & -10 & -10 \end{bmatrix}^T$
Initial velocity (m/s)	$\begin{bmatrix} 0 & 0 & 0 \end{bmatrix}^T$	$\begin{bmatrix} 0 & 0 & 0 \end{bmatrix}^T$	$\begin{bmatrix} 0 & 0 & 0 \end{bmatrix}^T$	$\begin{bmatrix} 0 & 0 & 0 \end{bmatrix}^T$
Final position (m)	$\begin{bmatrix} 0 & 10 & -10 \end{bmatrix}^T$	$\begin{bmatrix} 0 & -10 & -10 \end{bmatrix}^T$	$\begin{bmatrix} 0 & -10 & 10 \end{bmatrix}^T$	$\begin{bmatrix} 0 & 10 & 10 \end{bmatrix}^T$
Final velocity (m/s)	$\begin{bmatrix} 0 & 0 & 0 \end{bmatrix}^T$	$\begin{bmatrix} 0 & 0 & 0 \end{bmatrix}^T$	$\begin{bmatrix} 0 & 0 & 0 \end{bmatrix}^T$	$\begin{bmatrix} 0 & 0 & 0 \end{bmatrix}^T$

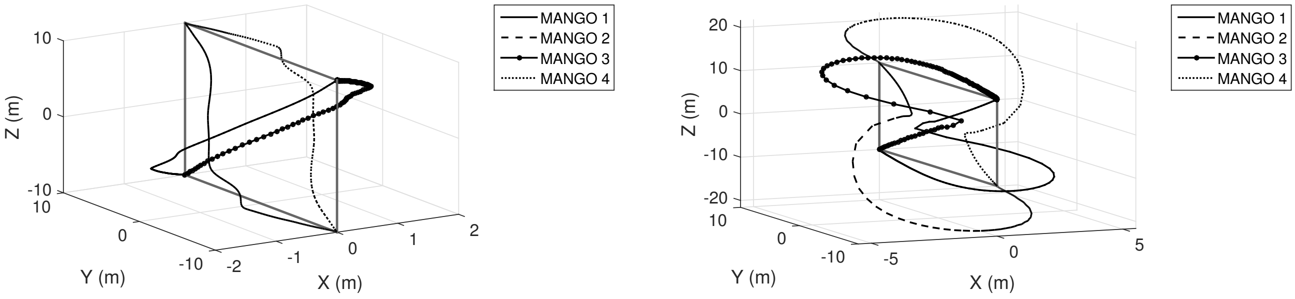

(a) Without CAS

(b) With CAS

Fig. 5.12 Manoeuvre trajectory in Scenario 2

(5.15). The components of the total thrust input obtained with the CAS, control input and repulsive force, are also observed in Fig (5.16).

The controller first estimates the values of the uncertain parameters ε_M, ε_J and ε_D. It can be noticed that these parameters show an adaptive behaviour, starting from their initial value, passing through the transient response, until stable constant values are found by the controller in the steady state, as observed in Figure (5.17).

When the CAS is active, the four uncertain parameters are estimated for both followers, as observed in Fig. (5.18). As in the case without CAS, the estimated parameters also show adaptive behaviour during the first instants of the manoeuvre, until the controller finally finds steady final values. The effects caused by the actions of the CAS are also noticeable in Δv and fuel consumption, as seen in Table (5.7), for example, it can be seen that Mango 2 increases its Δv and fuel consumption 8 times with respect to the results obtained without the CAS.

5.4.3 Scenario 3

This scenario simulates a high-eccentricity on-orbit transfer of two Mango satellites using a reference orbit with an eccentricity value of 0.8, a perigee altitude of 450 km and a period of 17.5 hours. The control parameters are chosen as $\Gamma = 1$, $\kappa = 20$ and $\alpha = 150$ with CAS parameters selected as $D = 5$

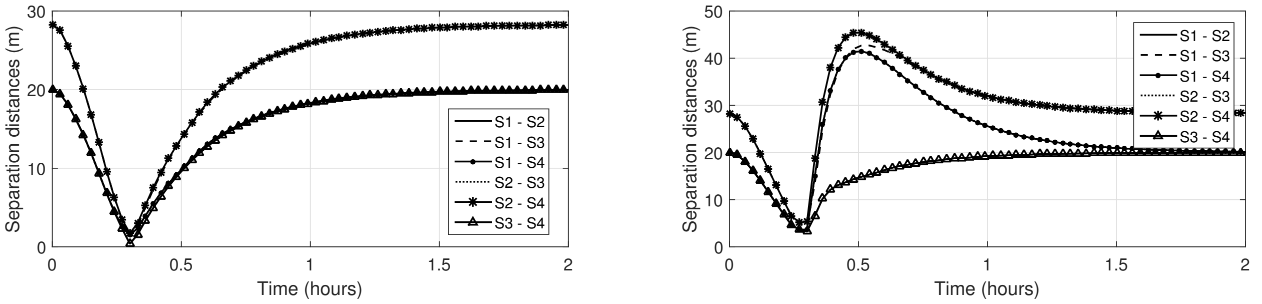

(a) Without CAS (b) With CAS

Fig. 5.13 Separation distance in Scenario 2

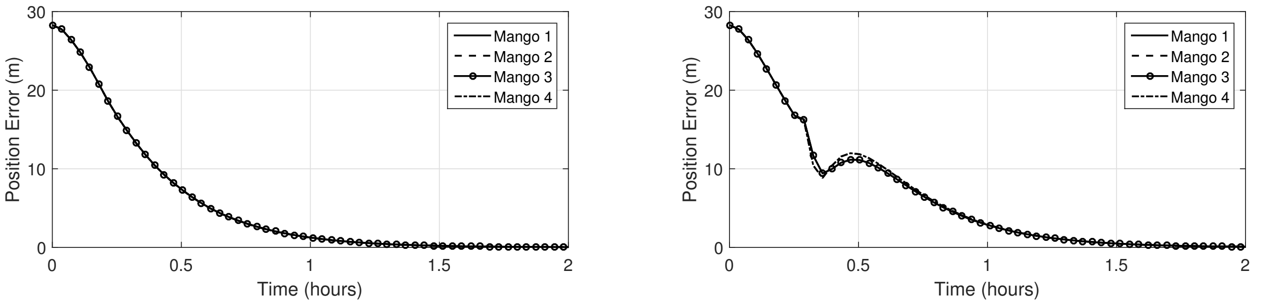

(a) Without CAS (b) With CAS

Fig. 5.14 Magnitude of the position error in Scenario 2

m and $\sigma = 3$, for all spacecraft. Once again, the scenario is simulated with and without the effects of the CAS and its results are then compared. The initial and final conditions for this scenario are indicated in Table (5.8) and the objective is to interchange positions between spacecraft while generating a collision threat during the movement.

The $x - y$ plane manoeuvre in the $\mathcal{L}$ frame is presented in Fig. (5.19) and it is observed in Fig. (5.19b) that extra manoeuvring is generated due to collision avoidance action, in contrast with the movement in Fig. (5.19a) obtained without the effects of the CAS.

These dynamical features caused by the CAS can also be observed in other measured parameters, for example, the separation distance is shown in Fig. (5.20), where it is observed that some spacecraft collide in Fig (5.20a), while this threat vanishes when the CAS is activated as indicated in Fig. (5.20b).

Other parameters considered in this scenario are the error dynamics in Fig. (5.21), the thrust behaviour as seen in Fig. (5.22) and the components of the total thrust input in Fig (5.23).

The estimation of the uncertain parameters ε_M, ε_J and ε_D, when the CAS is inactive, show a changing behaviour during the transient response, until stable constant values are found by the

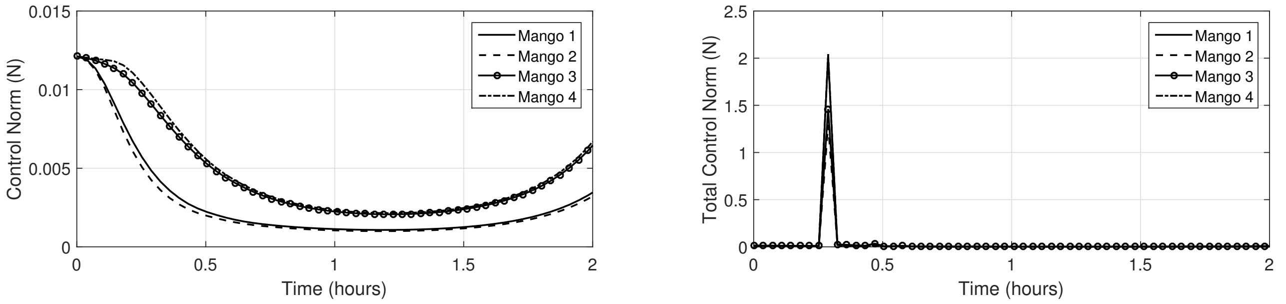

(a) Without CAS (b) With CAS

Fig. 5.15 Magnitude of the control input in Scenario 2

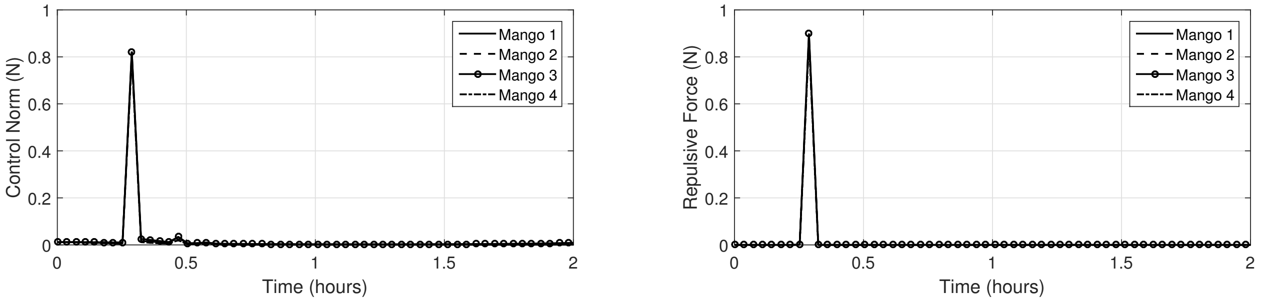

(a) (b)

Fig. 5.16 Components of the total control input with CAS in Scenario 2

controller in the steady state, as observed in Figure (5.24). On the other hand, when the CAS is active, the four uncertain parameters ε_M, ε_J, ε_D and ε_R are now estimated, as observed in Figure (5.25). The estimation process for these parameters also shows a changing behaviour during the transient response until final values are reached at steady state. The influence of the CAS in Δv and fuel consumption is observed in the results presented in Table (5.9) where, for example, it can be noticed that Mango 1 increases its fuel consumption 15 times with respect to the manoeuvre without CAS.

5.5 Chapter Conclusions

In this chapter a noncertainty-equivalence analytically-oriented adaptive tracking control law for spacecraft formation flying, applicable to both circular and eccentric reference orbits, was developed via Immersion and Invariance methodology. The controller allows a follower spacecraft to track a time-varying reference trajectory, while uncertainty in the modelling of the perturbation forces is

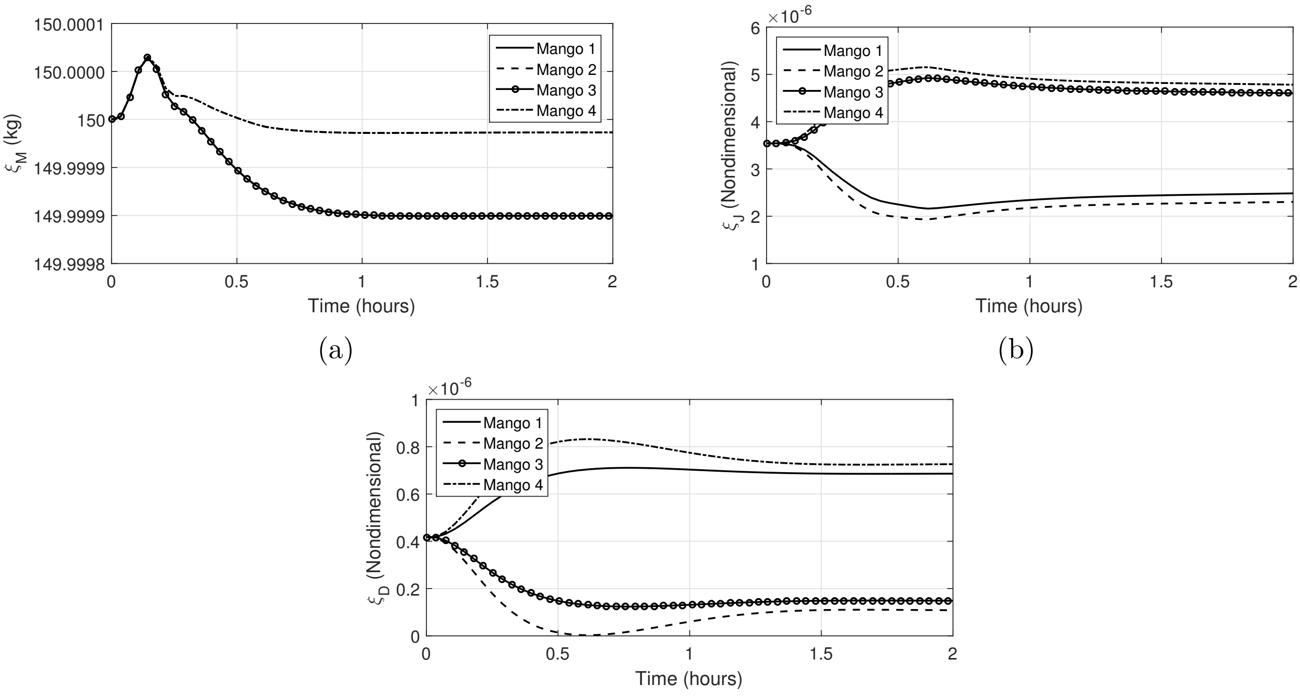

(a) (b)

(c)

Fig. 5.17 Estimated parameters without CAS in Scenario 2

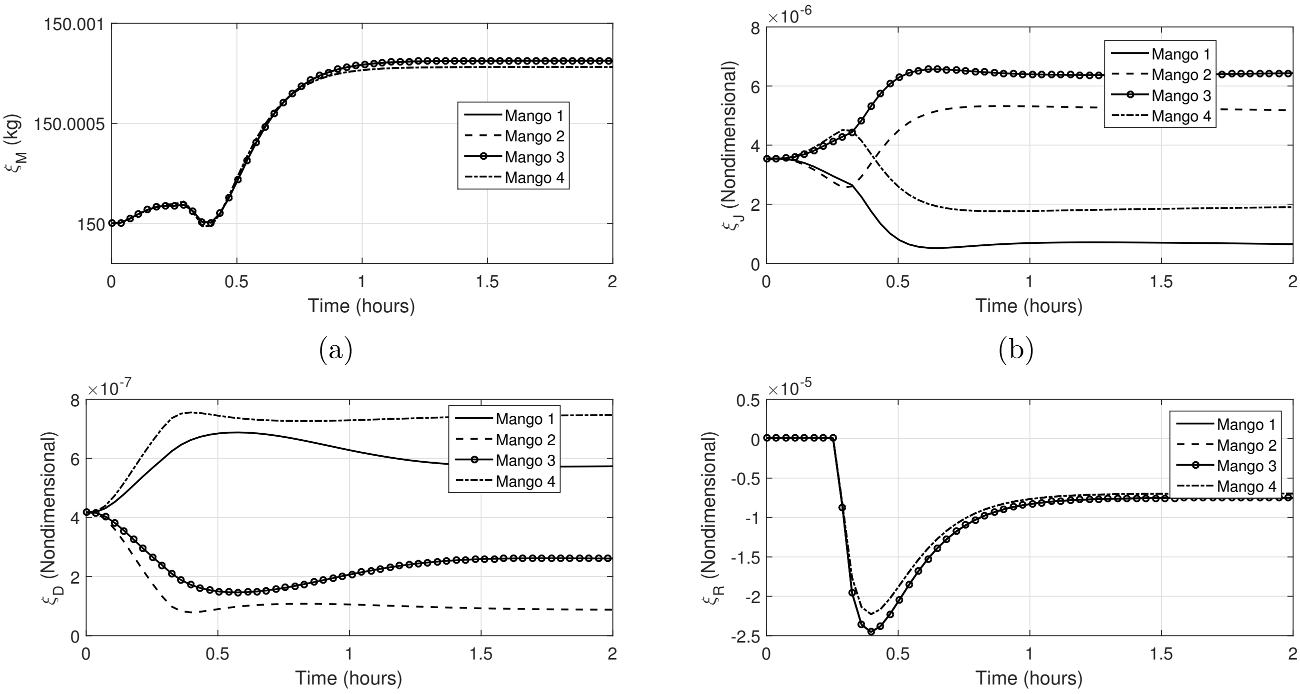

(a) (b)

(c) (d)

Fig. 5.18 Estimated parameters with CAS in Scenario 2

present. The main attribute of this methodology is the addition of a new term to the classical CE control approach which, simultaneously with the parameter update law, is developed to achieve

Table 5.7 Summary of results for Scenario 2

WITHOUT CAS	**MANGO 1**	**MANGO 2**	**MANGO 3**	**MANGO 4**	**TOTAL**
Δv (m/s)	0.19	0.18	0.33	0.34	1.04
Fuel consumption (g)	13.47	12.57	23.21	24.11	73.36
Max. Thrust (N)	0.012	0.012	0.015	0.016	0.055
Final Position Error (m)	0.013	0.014	0.013	0.014	0.054
Final Velocity Error (m/s)	0	0	0	0	0
WITH CAS	**MANGO 1**	**MANGO 2**	**MANGO 3**	**MANGO 4**	**TOTAL**
Δv (m/s)	1.79	1.45	1.69	1.78	6.71
Fuel consumption (g)	124.94	101.05	117.55	123.9	467.44
Max. Thrust (N)	3.03	2.05	2.09	2.84	10.01
Final Position Error (m)	0.02	0.02	0.02	0.02	0.08
Final Velocity Error (m/s)	0	0	0	0	0

Table 5.8 Initial and final conditions in Scenario 3

	MANGO 1	**MANGO 2**
Initial position (m)	$\begin{bmatrix} 10 & 0 & 0 \end{bmatrix}^T$	$\begin{bmatrix} -10 & 0 & 0 \end{bmatrix}^T$
Initial velocity (m/s)	$\begin{bmatrix} 0 & 0 & 0 \end{bmatrix}^T$	$\begin{bmatrix} 0 & 0 & 0 \end{bmatrix}^T$
Final position (m)	$\begin{bmatrix} -10 & 0 & 0 \end{bmatrix}^T$	$\begin{bmatrix} 10 & 0 & 0 \end{bmatrix}^T$
Final velocity (m/s)	$\begin{bmatrix} 0 & 0 & 0 \end{bmatrix}^T$	$\begin{bmatrix} 0 & 0 & 0 \end{bmatrix}^T$

Table 5.9 Summary of results for Scenario 3

WITHOUT CAS	**MANGO 1**	**MANGO 2**	**TOTAL**
Δv (m/s)	0.24	0.12	0.36
Fuel consumption (g)	16.98	8.94	25.92
Max. Thrust (N)	0.04	0.04	0.08
Final Position Error (m)	0	0	0
Final Velocity Error (m/s)	0	0	0
WITH CAS	**MANGO 1**	**MANGO 2**	**TOTAL**
Δv (m/s)	3.62	2.87	6.49
Fuel consumption (g)	251.51	199.86	451.37
Max. Thrust (N)	9.33	7.16	16.49
Final Position Error (m)	0	0	0
Final Velocity Error (m/s)	0	0	0

adaptive stabilisation. This parameter has the objective of shaping the manifold into which the adaptive system is immersed. The stability of the proposed control law was proven using Lyapunov stability theory and Barbalat's lemma. The controller performance and capabilities were analysed in three simulated scenarios showing effective tracking of the nominal trajectory and estimation of uncertain parameters, while eliminating the risk of collision during close proximity manoeuvres.

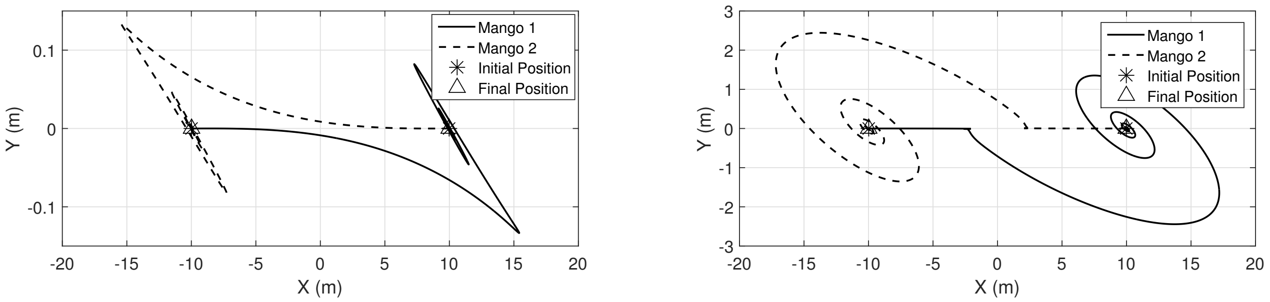

(a) Without CAS (b) With CAS

Fig. 5.19 Manoeuvre trajectory in Scenario 3

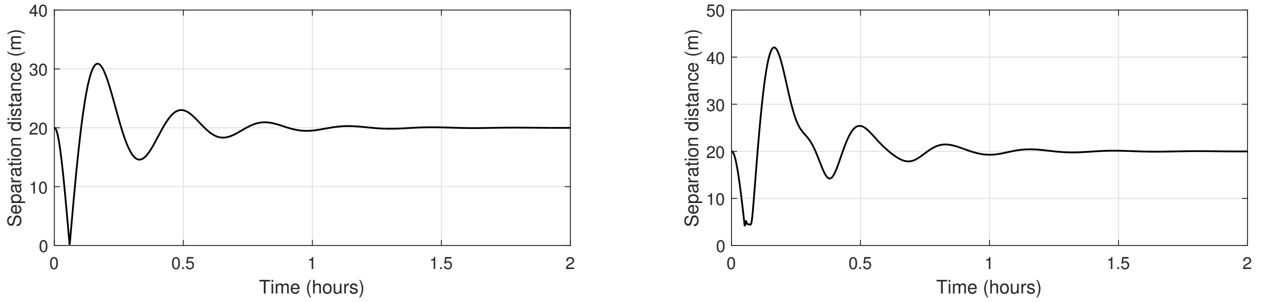

(a) Without CAS (b) With CAS

Fig. 5.20 Separation distance in Scenario 3

The same simulations also showed increments in total Δv and fuel consumption with respect to the same manoeuvre without CAS, although this increment was expected, since the followers require additional manoeuvring in order to avoid collision. As mentioned in Table 1.1, the propellant tank included in the spacecraft Mango of PRISMA mission contains about 5.6 kg of usable fuel and gives approximately 60 m/s Δv over the mission. Averaging the Δv per spacecraft per manoeuvre we obtain a value of 2.3 m/s, which would allow a follower with the same fuel tanks features as Mango, to perform up to 26 manoeuvres. The average simulation execution time per spacecraft in MATLAB was 0.268 seconds, including external perturbations and CAS. This time measurement (the best of all three control approaches presented in this thesis) suggests that this algorithm may be suitable for current on-board satellite computational capacities.

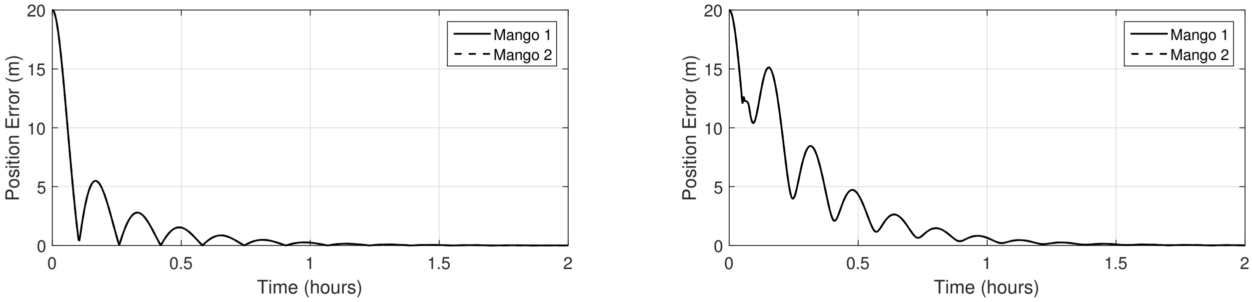

(a) Without CAS (b) With CAS

Fig. 5.21 Magnitude of the position error in Scenario 3

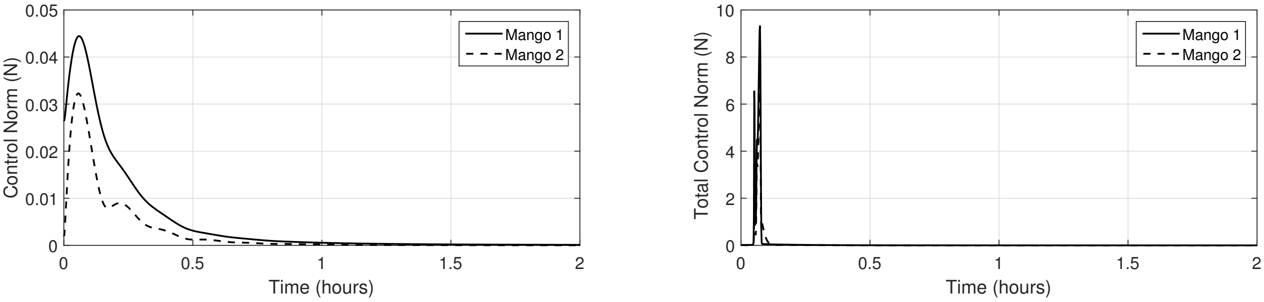

(a) Without CAS (b) With CAS

Fig. 5.22 Magnitude of the control input in Scenario 3

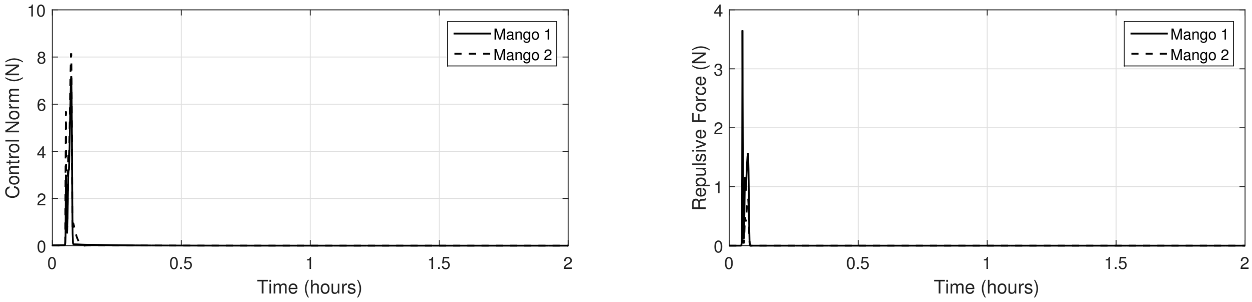

(a) (b)

Fig. 5.23 Components of the total control input with CAS in Scenario 3

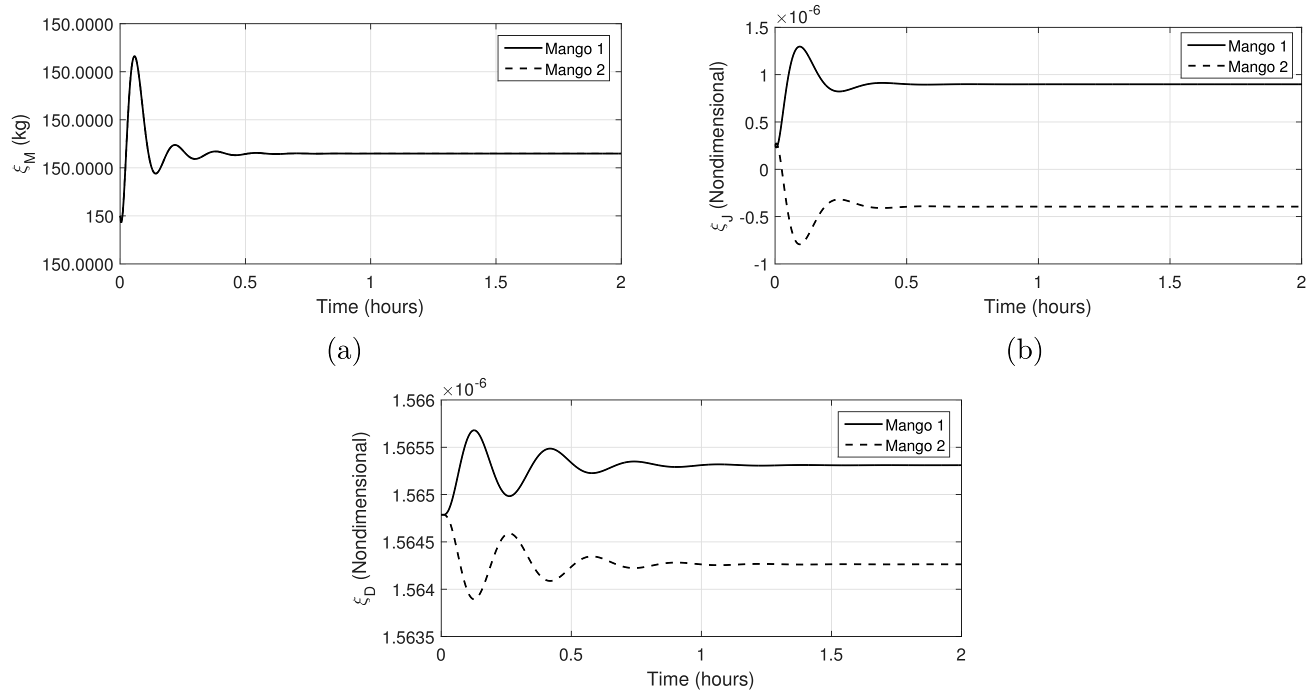

(a) (b)

(c)

Fig. 5.24 Estimated parameters without CAS in Scenario 3

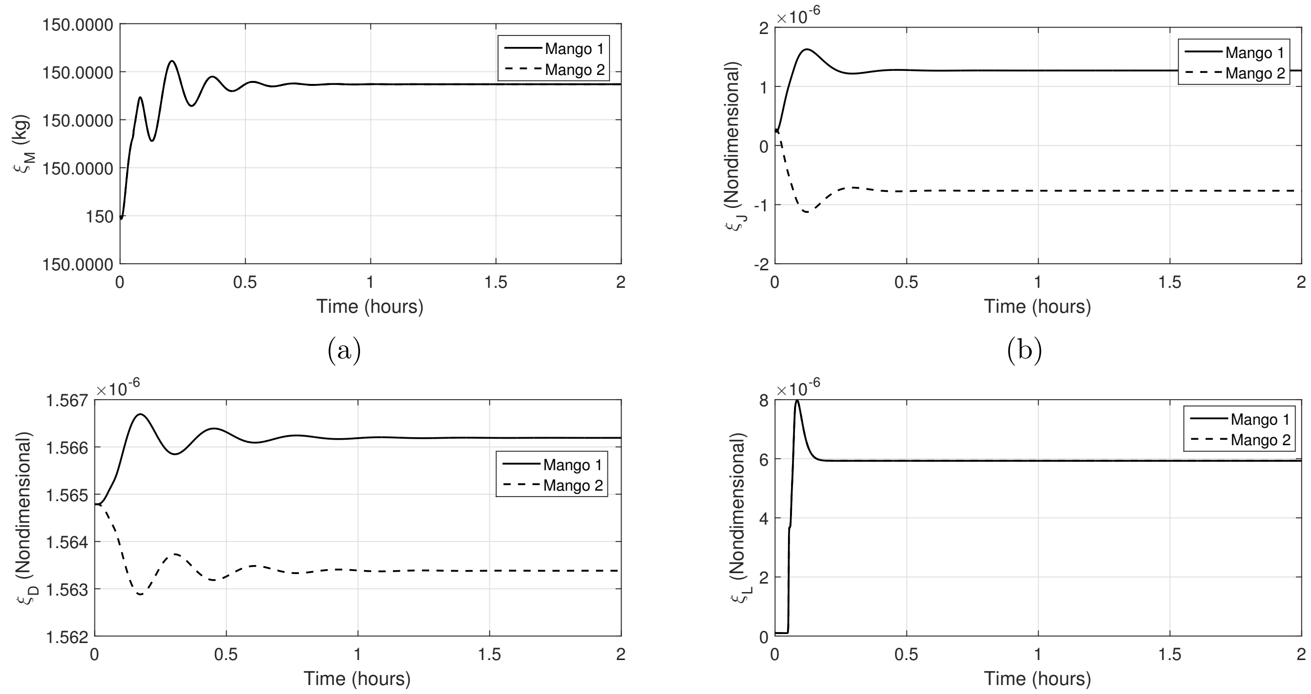

(a) (b)

(c) (d)

Fig. 5.25 Estimated parameters with CAS in Scenario 3

Chapter 6

Conclusions and Future Work

6.1 Conclusions

The objective of this thesis is to introduce new control methods to allow spacecraft in formation, with circular/elliptical reference orbits, to efficiently execute safe autonomous manoeuvres. These controllers distinguish from the bulk of literature in that they merge guidance laws never applied before to spacecraft formation flying and collision avoidance capacities into a single control strategy. The proposed control schemes are linear optimal tracking (LQR-APF) in Chapter 3, forward-in-time linear optimal estimation (SESP-CAS) in Chapter 4 and Immersion and Invariance adaptive control (I&I-CAS) in Chapter 5. All controllers incorporate a collision avoidance scheme (CAS) based on a Gaussian artificial potential. In general terms, the proposed control approaches command the dynamical performance of one or several followers, with respect to a leader, to asymptotically track a time-varying nominal trajectory, while the threat of collision between the followers is eliminated by means of repelling accelerations generated by the CAS.

In Chapter 3, the theory of linear quadratic regulators (LQR) and artificial potentials (APF) are used to design a new mixed LQR-APF tracking control approach for close-manoeuvring spacecraft in formation. This approach differs from other formation flying control strategies in that it merges the advantages of guidance control with the artificial potential functions to provide a more complete control strategy. Moreover, it provides a more general framework with capacity to deal with both circular and elliptical reference orbits. In general terms, the controller allow the followers within a formation to track a desired relative trajectory while fuel consumption is optimized. It also incorporates nonlinear repulsive accelerations from an artificial potential field, in order to perform collision avoidance during proximity operations. The controller was implemented in three scenarios for spacecraft formation reconfiguration and swapping and its performance was analysed with and without the implementation of the CAS. The results obtained from the numerical simulations show that the LQR-CAS controller successfully fulfils the thesis objective. First, the controller has the ability to effectively guide the spacecraft towards a time-varying desired trajectory, in reference orbits with low or high eccentricity, with a very low convergence error. Secondly, the performance of the controller with the CAS during collision threats demonstrates its feasibility for applications where safe close-proximity manoeuvers are required. However, the autonomy objective is only partially accomplished since weight matrices and CAS parameters must be tuned manually until an adequate manoeuver is found. Nevertheless, the application of this controller could provide solid advantages during the first design stages of more complex and sophisticated controllers for spacecraft formation flying. Additional results also showed that the performance of the controller, in terms of total manoeuvre Δv and fuel consumption, was affected by the selection of the weight matrices and CAS parameters. Those manoeuvers where the CAS was active showed increments in total Δv and fuel consumption with respect to the same manoeuvre without CAS, although this increment was expected, since the spacecraft required additional collision avoidance manoeuvres, especially in those spacecraft with higher collision risk. Moreover, fuel consumption remained low, allowing the followers to perform up to 70 manoeuvres if fuel tank conditions are considered as in Mango spacecraft. The average MATLAB total execution time remain around the 0.315 seconds mark, making this controller computationally light and suitable for on-orbit applications.

The LQR-CAS controller assumes the spacecraft state is fully available during the control process. In reality this is not the case and, therefore, in Chapter 4, a new control approach named SESP-CAS, which is based on the forward-in-time state estimation approach developed in (Damak et al., 2013), is applied for the first time to close-manoeuvring control and collision-avoidance spacecraft in formation. In general terms, the SESP-CAS allows the followers within a formation to track a time-varying reference trajectory, while uncertainty in the modelling of the dynamics and sensor measurement is present. A collision avoidance scheme is also included as in the previous chapter. The controller was implemented in the same previous scenarios and, with regards to the thesis objective, can effectively track different nominal trajectories in reference orbits with low and high eccentricity, despite model and sensor uncertainty being present during the control process. Safe manoeuvring was also accounted for by means of the CAS, during close-proximity operations, decreasing the risk of collision between the followers and showing, once more, that the use of artificial potentials is an adequate approach for collision avoidance. On the other hand, the autonomy objective was again not completely accomplished since, as in the previous control approach, weight matrices and CAS parameters must be tuned manually until the desired performance is found. Nevertheless, the SESP-CAS control approach outperforms the LQR-CAS since it allows to obtain controlled manoeuvres while accounting for uncertainties in the dynamical model and sensor measurements. The simulated scenarios also showed that total manoeuvre Δv and fuel consumption was also affected by the selection of the control weights, parameters and the estimation process. For instance, in the cases where the CAS was active, an increase in these quantities was detected, however, these increments were expected since the followers required extra manoeuvring to perform collision avoidance. Additionally, fuel consumption remained relatively low, allowing the followers to perform up to 63 manoeuvres if fuel tank conditions are considered as in Mango spacecraft in PRIMSA mission. The average MATLAB total execution time remain around 3.77 seconds (higher among the controller presented in this thesis). Its capacity to handle uncertainties in optimal manner makes this controller also suitable for on-orbit realistic applications.

The control approaches presented in previous chapters present complications in order to fulfil the autonomy objective in this thesis, since they rely on weight and parameter tuning. Moreover, they do not have the ability to self-adapt to cope with uncertainties present during the control process. To this aim, the contribution in Chapter 5 is to apply, for the first time, the Immersion and Invariance adaptive approach developed in (Astolfi et al., 2008a) and (Seo and Akella, 2008) to close-manoeuvring control and collision-avoidance of spacecraft in formation. The controller allows a follower spacecraft to track a time-varying reference trajectory, while it self-adapts in order to cope with uncertainty in the modelling of the perturbation forces and CAS. The controller presented measurements that show an effective capacity to deal with tracking manoeuvring as observed in the simulated scenarios, proving also an asymptotic behaviour toward the desired trajectories. One of the main features of the proposed approach is its ability to deal with uncertain parameters. During the execution of the simulations, the controller also determined, autonomously, the estimation of uncertain parameters. Also, different error convergence rates were obtained using three different tuning parameters, although, faster convergence rates usually lead to higher control input demands. Safe manoeuvring was also accomplished by the control scheme and the CAS. When close-proximity manoeuvers were executed, the CAS proved to be an effective way to decrease the collision risk between the followers and although the use of CAS showed increments in total Δv and fuel consumption with respect to the same manoeuvre without CAS, this behaviour was expected since further manoeuvring was required by the followers in order to avoid collision. Autonomy was accounted by the self-adapting nature of the control methodology. As mentioned before, the control approach has the capacity to automatically adapt uncertain parameters in response to the dynamics of the plant and error convergence rate, although, error convergence rate parameters must be tuned up manually until a desired behaviour was shown. Moreover, fuel consumption remained high among the controllers presented in this thesis, allowing the followers to perform up to 26 manoeuvres if fuel tank conditions are considered as in Mango spacecraft. However, the average MATLAB total execution time remain around 0.268 seconds, making this controller computationally lighter than the rest of the control approaches in this thesis. These features and the capacity to deal with perturbations make this control scheme suitable for on-orbit applications. Given the aforementioned features and that Immersing and Invariance also provides a natural framework for observer design for general nonlinear systems, it is concluded that the I& I-CAS control approach is the most adequate of the three control approaches presented in this thesis for spacecraft formation flying.

6.2 Limitations of the work

Despite the amount of positive results presented in this thesis, the proposed control schemes also present some limitations. For instance, regarding the LQR-CAS controller:

- The scheme is based on linearized relative dynamics, therefore, it is only valid when the relative distance of the follower with respect to the centre of formation is small in comparison with its inertial orbital position.
- Although the scheme presents optimisation features, these broke as nonlinearities are added to the model, turning the controller suboptimal.
- It is necessary to manually tune-in the weight matrices.

- It does not contemplate the rotational movement of the follower.

Regarding the SESP-CAS scheme, the limitations are:

- All the limitations presented in the previous controller also apply to this scheme.
- As the complexity of the representation of the sensor grows, also the computational effort required to estimate the correct state.

The I&I-CAS also presents limitations. For example:

- There is no standard procedure to select the initial values of the estimation law.
- The convergence parameters must be tune-in manually.
- The scheme does not contemplate the rotational movement of the followers.

6.3 Future work

In this section, a few avenues for future work regarding the tuning of the control parameters, the use of orbital perturbations and long-time horizons, code design in order to handle large numbers of spacecraft and the implementation of more realistic simulations are proposed.

6.3.1 Tuning of Control Parameters

There is still room for improvement regarding the design of procedures for the tuning of controller parameters. In the case of the LQR-CAS and SESP-CAS frameworks, further studies are yet be done to design an automatic procedure that determines optimal values of the CAS parameters and the weight matrices. On the other hand, the I&I-CAS controller partially fulfil the issue of determine values of the CAS parameters, given that it performs an adaptive estimation of the amplitude of the repelling acceleration. However, convergence rate parameters are yet required to be selected manually. The development of a control scheme that performs without the need of weights and parameters would be preferable.

6.3.2 Orbital Perturbations and Long-Time Horizons

Several test cases were used to validate the the I&I-CAS controller in low Earth orbits using orbital perturbations like J_2 and atmospheric drag, however, it would be interesting to test the performance and the scope of the LQR-CAS and SESP-CAS controllers in scenarios including these perturbations. Also, it would be important to add more orbital perturbations, like sun pressure and third body effects, in order to create a more complete and realistic simulation. Moreover, interesting dynamical features may appear during performance of all the three controllers while implementing simulated scenarios with long-time horizons.

6.3.3 More Realistic Simulations

Further improvements could be made in the simulations by adding more realistic features to the simulations, for instance, by including more accurate actuator and sensor uncertainty models. Additionally, future research could focus on the extension of the work done in this thesis to six-degree-of-freedom dynamical systems and contemplating additional nonlinear perturbations in the dynamics. Advancements could also be done in computational coding in order to create a methodology that systematically allows to add large numbers of spacecraft to the simulations. Finally, the controllers may be implemented in a Hardware-In-the-Loop-Simulation to carry out real-time experiments in order to effectively illustrate and evaluate its performance.

References

Kyle Alfriend, Srinivas Rao Vadali, Pini Gurfil, Jonathan How, and Louis Breger. *Spacecraft Formation Flying: Dynamics, Control, and Navigation*. Butterworth-Heinemann, 2009. ISBN 0080559654.

P.J. Antsaklis, K.M. Passino, and S.J. Wang. An introduction to autonomous control systems. *IEEE Control Systems*, 11(4):5–13, 1991. ISSN 1066-033X. doi: 10.1109/37.88585.

Jean Sébastien Ardaens, Simone D'Amico, and A. Cropp. GPS-based relative navigation for the Proba-3 formation flying mission. *Acta Astronautica*, 91:341–355, 2013. ISSN 00945765. doi: 10.1016/j.actaastro.2013.06.025.

JS Ardaens, R Kahle, and D Schulze. In–flight performance validation of the TanDEM–X autonomous formation flying system. *International Journal of Space Science and Engineering*, (1):1–11, 2014. doi: 10.1504/IJSPACESE.2014.060596.

Alessandro Astolfi and Romeo Ortega. Immersion and invariance: A new tool for stabilization and adaptive control of nonlinear systems. *IEEE Transactions on Automatic Control*, 48(4):590–606, 2003. ISSN 00189286. doi: 10.1109/TAC.2003.809820.

Alessandro Astolfi, Dimitrios Karagiannis, and Romeo Ortega. *Nonlinear And Adaptive Control With Applications*. Springer-Verlag, 2008a. ISBN 978-1-84800-065-0. doi: 10.1007/978-1-84800-066-7.

Alessandro Astolfi, Dimitrios Karagiannis, and Romeo Ortega. *Nonlinear and Adaptive Control with Applications*. Springer, 2008b. ISBN 0178-5354. doi: 10.1007/978-1-84800-066-7.

Michael Athans and Peter L. Falb. *Optimal Control: An Introduction to the Theory and Its Applications*. Dover Publications, 2006. ISBN 0486453286.

Ahmed Badawy and Colin R. McInnes. On-Orbit Assembly Using Superquadric Potential Fields. *Journal of Guidance, Control, and Dynamics*, 31(1):30–43, 2008. ISSN 0731-5090. doi: 10.2514/1.28865.

Ahmed Badawy and Colin R. McInnes. Small spacecraft formation using potential functions. *Acta Astronautica*, 65(11-12):1783–1788, 12 2009. ISSN 00945765. doi: 10.1016/j.actaastro.2009.05.002.

Jonghee Bae and Youdan Kim. Formation Pattern Analysis of Follower Spacecraft for Elliptic Reference Orbits. *The Journal of the Astronautical Sciences*, 60(2):167–185, 6 2013. ISSN 0021-9142. doi: 10.1007/s40295-015-0040-6.

Peter M. Bainum, Avaine Strong, Zhaozhi Tan, and Pedro a. Capó-Lugo. Techniques for deploying elliptically orbiting constellations in along-track formation. *Acta Astronautica*, 57(9):685–697, 11 2005. ISSN 00945765. doi: 10.1016/j.actaastro.2005.03.065.

Mai Bando and Akira Ichikawa. Active Formation Flying Along an Elliptic Orbit. *Journal of Guidance, Control, and Dynamics*, 36(1):324–332, 1 2012. ISSN 0731-5090. doi: 10.2514/1.57703.

Saptarshi Bandyopadhyay, Rebecca Foust, Giri P. Subramanian, Soon-Jo Chung, and Fred Y. Hadaegh. Review of Formation Flying and Constellation Missions Using Nanosatellites. *Journal of Spacecraft and Rockets*, pages 1–12, 2016. ISSN 0022-4650. doi: 10.2514/1.A33291.

B. Bastida Virgili, J.C. Dolado, H.G. Lewis, J. Radtke, H. Krag, B. Revelin, C. Cazaux, C. Colombo, R. Crowther, and M. Metz. Risk to space sustainability from large constellations of satellites. *Acta Astronautica*, 126:154–162, 2016. ISSN 00945765. doi: 10.1016/j.actaastro.2016.03.034.

R. RR Bate, D. DD Mueller, and JE White. *Fundamentals of Astrodynamics*. Dover Publications Inc., New York, 1971. ISBN 0486600610.

RH Battin. *An introduction to the mathematics and methods of astrodynamics*. AIAA, 1999. ISBN 1563473429.

Ohad Ben-Yaacov and Pini Gurfil. Long-Term Cluster Flight of Multiple Satellites Using Differential Drag. *Journal of Guidance, Control, and Dynamics*, 36(6):1731–1740, 11 2013. ISSN 07315090. doi: 10.2514/1.61496.

Derek J. Bennet and Colin R. McInnes. Pattern transition in spacecraft formation flying via the artificial potential field method and bifurcation theory. In *European Space Agency, (Special Publication) ESA SP*, number 654 SP, 2008. ISBN 9789292212186.

Derek J. Bennet and Colin R. McInnes. Distributed control of multi-robot systems using bifurcating potential fields. *Robotics and Autonomous Systems*, 58(3):256–264, 3 2010. ISSN 09218890. doi: 10.1016/j.robot.2009.08.004.

L. Breger, J. How, and A. Richards. Model predictive control of spacecraft formations with sensing noise. In *American Control Conference*, pages 2385–2390. Ieee, 2005. ISBN 0-7803-9098-9. doi: 10.1109/ACC.2005.1470323.

Arthur Earl Bryson and Yu-Chi Ho. *Applied Optimal Control: Optimization, Estimation, and Control*. Taylor & Francis, 1975. ISBN 0891162283.

Pedro Capó-Lugo and Peter Bainum. Active control schemes based on the linearized Tschauner–Hempel equations to maintain the separation distance constraints for the NASA benchmark Tetrahedron Constellation. *Journal of Mechanics of Materials and Structures*, 2(October):1541–1559, 2007. ISSN 1559-3959. doi: 10.2140/jomms.2007.2.1541.

W. H. Clohessy and R. S. Wiltshire. Terminal Guidance System for Satellite Rendezvous. *Journal of the Aerospace Sciences*, 27(9):653–658, 1960. ISSN 1936-9999. doi: 10.2514/8.8704.

CSA. RADARSAT Constellation, 2015. URL http://www.asc-csa.gc.ca/eng/satellites/radarsat/.

H. Damak, I. Ellouze, and M.A. Hammami. A separation principle of time-varying nonlinear dynamical systems. *Differential Equations and Control Processes*, 1, 2013.

S D'Amico, J S Ardaens, and R Larsson. Spaceborne Autonomous Formation-Flying Experiment on the PRISMA Mission. *Journal of Guidance Control and Dynamics*, 35(3):834–850, 2012. ISSN 0731-5090. doi: Doi10.2514/1.55638.

Simone D'Amico, Jean-Sebastien Ardaens, and Sergio De Florio. Autonomous formation flying based on GPS — PRISMA flight results. *Acta Astronautica*, 82(1):69–79, 1 2013. ISSN 00945765. doi: 10.1016/j.actaastro.2012.04.033.

S. De Florio, S. D'Amico, and G. Radice. Flight Results of Precise Autonomous Orbit Keeping Experiment on PRISMA Mission. *Journal of Spacecraft and Rockets*, 50(3):662–674, 5 2013. ISSN 0022-4650. doi: 10.2514/1.A32347.

S. De Florio, S. D'Amico, and G. Radice. Virtual Formation Method for Precise Autonomous Absolute Orbit Control. *Journal of Guidance, Control, and Dynamics*, 37(2):425–438, 3 2014. ISSN 0731-5090. doi: 10.2514/1.61575.

Marcio S. De Queiroz, Vikram Kapila, and Qiguo Yan. Adaptive Nonlinear Control of Multiple Spacecraft Formation Flying. *Journal of Guidance, Control, and Dynamics*, 23(3):385–390, 2000. ISSN 0731-5090. doi: 10.2514/2.4549.

Marco D'Errico, editor. *Distributed Space Missions for Earth System Monitoring.* Springer, 2013. ISBN 978-1-4614-4540-1. doi: 10.1007/978-1-4614-4541-8.

ESA. Sentinel 1 to 6, 2015. URL http://www.esa.int/Our{_}Activities/Observing{_}the{_}Earth/Copernicus/Overview4.

Gene F Franklin, David J Powell, and Abbas Emami-Naeini. *Feedback Control of Dynamic Systems.* Prentice Hall, 7th edition, 2001. ISBN 0130323934.

Hans Peter Geering. *Optimal Control with Engineering Applications.* Springer, 2007. ISBN 3540694374.

P Gurfil, M Idan, and NJ Kasdin. Adaptive neural control of deep-space formation flying. *Journal of guidance, control, and dynamics*, 26(3):491–501, 2003. doi: http://dx.doi.org/10.2514/2.5072.

Pini Gurfil. *Modern Astrodynamics.* Butterworth-Heinemann, 2003. ISBN 0080973701.

Wassim M. Haddad and VijaySekhar Chellaboina. *Nonlinear Dynamical Systems and Control: A Lyapunov-Based Approach.* Princeton University Press, 2008. ISBN 9780691133294.

Jean-Francois Hamel and Jean De Lafontaine. Linearized Dynamics of Formation Flying Spacecraft on a J2-Perturbed Elliptical Orbit. *Journal of Guidance, Control, and Dynamics*, 30(6):1649–1658, 11 2007. ISSN 0731-5090. doi: 10.2514/1.29438.

Henry Helvajian. *Microengineering Aerospace Systems.* AIAA, 1999. ISBN 1884989039.

Erik A. Hogan and Hanspeter Schaub. Collinear invariant shapes for three-spacecraft Coulomb formations. *Acta Astronautica*, 72:78–89, 2012. ISSN 00945765. doi: 10.1016/j.actaastro.2011.10.020.

Xu Huang, Ye Yan, and Yang Zhou. Optimal spacecraft formation establishment and reconfiguration propelled by the geomagnetic Lorentz force. *Advances in Space Research*, 54(11):2318–2335, 2014. ISSN 0273-1177. doi: 10.1016/j.asr.2014.08.010.

Gökhan Inalhan, Michael Tillerson, and Jonathan P How. Relative Dynamics and Control of Spacecraft Introduction. *Journal of Guidance, Control, and Dynamics*, 25(1):48–59, 2002. ISSN 0731-5090. doi: 10.2514/2.4874.

Rudolf Emil Kalman. Contributions to the Theory of Optimal Control. *Bol. Soc. Mat. Mexicana vol. 5*, 5:102–119, 1960. ISSN 00160032. doi: 10.1016/0016-0032(63)90689-6.

Thomas R. Kane, Peter W. Likins, and David A. Levinson. *Spacecraft Dynamics.* McGraw Hill Inc., first edition, 1983. ISBN 0070378436.

N. Jeremy Kasdin, Pini Gurfil, and Egemen Kolemen. Canonical modelling of relative spacecraft motion via epicyclic orbital elements. *Celestial Mechanics and Dynamical Astronomy*, 92:337–370, 2005. ISSN 09232958. doi: 10.1007/s10569-004-6441-7.

Hassan K. Khalil. *Nonlinear Systems.* Prentice Hall, third edition, 1996. ISBN 0132280248.

Huibert Kwakernaak and Raphel Sivan. *Linear Optimal Control Systems.* Wiley-Blackwell, 1972. ISBN 0471511102.

Eugene Lavretsky and Kevin a. Wise. *Robust and Adaptive Control.* Springer, 2013. ISBN 978-1-4471-4395-6.

Daero Lee, Amit K. Sanyal, and Eric a. Butcher. Asymptotic Tracking Control for Spacecraft Formation Flying with Decentralized Collision Avoidance. *Journal of Guidance, Control, and Dynamics*, 38(4):587–600, 2015. ISSN 0731-5090. doi: 10.2514/1.G000101.

Frank L. Lewis, Draguna Vrabie, and Vassilis L. Syrmos. *Optimal Control*. John Wiley & Sons, 2012. ISBN 1118122704.

Yong Li, Jianchang Liu, and Yu Wang. Design approach of weighting matrices for LQR based on multi-objective evolution algorithm. *2008 International Conference on Information and Automation*, (2):1188–1192, 6 2008. doi: 10.1109/ICINFA.2008.4608180.

Ismael Lopez and Colin R. McInnes. Autonomous rendezvous using artificial potential function guidance. *Journal of Guidance, Control, and Dynamics*, 18(2):237–241, 3 1995. ISSN 0731-5090. doi: 10.2514/3.21375.

Horacio J. Marquez. *Nonlinear Control Systems: Analysis and Design*. Wiley, first edition, 2003.

Leonel Mazal and Pini Gurfil. Cluster Flight Algorithms for Disaggregated Satellites. *Journal of Guidance, Control, and Dynamics*, 36(1):124–135, 1 2013. ISSN 0731-5090. doi: 10.2514/1.57180.

Leonel Mazal and Pini Gurfil. Closed-loop distance-keeping for long-term satellite cluster flight. *Acta Astronautica*, 94(1):73–82, 1 2014. ISSN 00945765. doi: 10.1016/j.actaastro.2013.08.002.

Leonel Mazal, G Mingotti, and Pini Gurfil. Global Low-Thrust Guidance Scheme for Disaggregated Spacecraft Architectures. In *63rd. International Astronautical Congress*, Naples, Italy, 2012. International Astronautical Federation.

Leonel Mazal, Giorgio Mingotti, and Pini Gurfil. Optimal On–Off Cooperative Maneuvers for Long-Term Satellite Cluster Flight. *Journal of Guidance, Control, and Dynamics*, 37(2):391–402, 3 2014. ISSN 0731-5090. doi: 10.2514/1.61431.

Shawn B McCamish, Marcello Romano, and Xiaoping Yun. Autonomous Distributed Control Algorithm for Multiple Spacecraft in Close Proximity Operation. In *AIAA Guidance, Navigation and Control Conference and Exhibition*, 2007.

C. McInnes. Autonomous Proximity Manoeuvring Using Artificial Potential Functions. *ESA Journal*, 17(2):159–169, 1993. ISSN 03792285.

Colin R. McInnes. Autonomous ring formation for a planar constellation of satellites. *Journal of Guidance, Control, and Dynamics*, 18(5):1215–1217, 9 1995. ISSN 0731-5090. doi: 10.2514/3.21531.

Colin R McInnes. Vortex formation in swarms of interacting particles. *Physical review. E, Statistical, nonlinear, and soft matter physics*, 75(3 Pt 1):032904, 3 2007. ISSN 1539-3755. doi: 10.1103/PhysRevE.75.032904.

F. McQuade and C. R. McInnes. Autonomous control for on-orbit assembly using potential function methods. *Aeronautical Journal*, 101(1006):255–262, 1997. ISSN 00019240.

Aristotle D. Michal. *Matrix and Tensor Calculus*. Dover Publications Inc., first edition, 2008.

Oliver Montenbruck and Ralph Kahle. Navigation and control of the TanDEM-X formation. *The Journal of the Astronautical Sciences*, 56(3):341–357, 2008. ISSN 0021-9142. doi: 10.1007/BF03256557.

Desineni Subbaram Naidu. *Optimal Control Systems*. CRC Press, 2003. ISBN 9780849308925.

Leonel Palacios, Matteo Ceriotti, and Gianmarco Radice. State Estimation for Spacecraft Formation Flying Based in the Separation Principle. In *International Astronautical Congress*, Toronto, 2014.

Leonel Palacios, Matteo Ceriotti, and Gianmarco Radice. Close proximity formation flying via linear quadratic tracking controller and artificial potential function. *Advances in Space Research*, 56(10): 2167–2176, 2015a. ISSN 18791948. doi: 10.1016/j.asr.2015.09.005.

Leonel Palacios, Gianmarco Radice, and Arun Misra. Formation Flying via Immersion and Invariance: An Adaptive Control Approach for Close-Manoeuvring Spacecraft Through Attractive Manifold Design. In *8th International Workshop on Satellite Constellations and Formation Flying*, Delft, Netherlands, 2015b.

Phil Palmer. Optimal Relocation of Satellites Flying in Near-Circular-Orbit Formations. *Journal of Guidance, Control, and Dynamics*, 29(3):519–526, 5 2006. ISSN 0731-5090. doi: 10.2514/1.14310.

Phil Palmer and Mark Halsall. Designing Natural Formations of Low-Earth-Orbiting Satellites. *Journal of Guidance, Control, and Dynamics*, 32(3):860–868, 2009. ISSN 0731-5090. doi: 10.2514/1.39631.

Haizhou Pan Haizhou Pan and V. Kapila. Adaptive nonlinear control for spacecraft formation flying with coupled translational and attitude dynamics. *Proceedings of the 40th IEEE Conference on Decision and Control*, 3:2057–2062, 2001. doi: 10.1109/.2001.980554.

Thomas V. Peters, João Branco, D. Escorial, Lorenzo Tarabini Castellani, and A. Cropp. Mission analysis for PROBA-3 nominal operations. *Acta Astronautica*, 102:296–310, 2014. ISSN 00945765. doi: 10.1016/j.actaastro.2014.01.010.

Carlo Pinciroli, Mauro Birattari, Elio Tuci, Marco Dorigo, Marco Del Rey Zapatero, Tamas Vinko, and Dario Izzo. Self-organizing and scalable shape formation for a swarm of pico satellites. In *Proceedings of the 2008 NASA/ESA Conference on Adaptive Hardware and Systems, AHS 2008*, pages 57–61, Bruxelles, Belgium, 2008. Institut de Recherches Interdisciplinaires et de Developpements en Intelligence Artificielle. ISBN 9780769531663. doi: 10.1109/AHS.2008.41.

Jaime L. Ramirez-Riberos, Marco Pavone, Emilio Frazzoli, and David W. Miller. Distributed Control of Spacecraft Formations via Cyclic Pursuit: Theory and Experiments. *Journal of Guidance, Control, and Dynamics*, 33(5):1655–1669, 2010. ISSN 0731-5090. doi: 10.2514/1.46511.

Marco Sabatini and Giovanni B Palmerini. Linearized formation-flying dynamics in a perturbed orbital environment. In *IEEE Aerospace Conference Proceedings*, number 1, pages 1–13. Ieee, 2008. ISBN 1424414881. doi: 10.1109/AERO.2008.4526271.

Luke Sauter and Phil Palmer. Analytic Model Predictive Controller for Collision-Free Relative Motion Reconfiguration. *Journal of Guidance, Control, and Dynamics*, 35(4):1069–1079, 2012. ISSN 0731-5090. doi: 10.2514/1.56521.

Daniel Scharf, FY Hadaegh, and Scott Ploen. A Survey of Spacecraft Formation Flying Guidance and Control (Part II): Control. In *Proceedings of the 2004 American Control Conference*, Boston, Mass., 2004.

Hanspeter Schaub. Stabilization of satellite motion relative to a Coulomb spacecraft formation. *Journal of Guidance, Control, and Dynamics*, 28(6):1231–1239, 2005. ISSN 00653438. doi: 10.2514/1.8577.

Hanspeter Schaub and Lee E. Z. Jasper. Orbit Boosting Maneuvers for Two-Craft Coulomb Formations. *Journal of Guidance, Control, and Dynamics*, 36(1):74–82, 2013. ISSN 0731-5090. doi: 10.2514/1.57479.

Hanspeter Schaub and John L Junkins. *Analytical mechanics of space systems.* AIAA, 2003. ISBN 1600867219. doi: 10.2514/4.861550.

Hanspeter Schaub, Gordon G Parker, Lyon B King, and Jan June. Challenges and Prospects of Coulomb Spacecraft Formation Control. *Journal of the Astronautical Sciences*, 52(1-2):169–193, 2004.

Shay Segal and Pini Gurfil. Effect of Kinematic Rotation-Translation Coupling on Relative Spacecraft Translational Dynamics. *Journal of Guidance, Control, and Dynamics*, 32(3):1045–1050, 5 2009. ISSN 0731-5090. doi: 10.2514/1.39320.

Prasenjit Sengupta, Srinivas R. Vadali, and Kyle T. Alfriend. Averaged Relative Motion and Applications to Formation Flight Near Perturbed Orbits. *Journal of Guidance, Control, and Dynamics*, 31(2):258–272, 3 2008. ISSN 0731-5090. doi: 10.2514/1.30620.

Dongeun Seo and Maruthi R. Akella. High-Performance Spacecraft Adaptive Attitude-Tracking Control Through Attracting-Manifold Design. *Journal of Guidance, Control, and Dynamics*, 31(4): 884–891, 7 2008. ISSN 0731-5090. doi: 10.2514/1.33308.

Sergey Shestakov, Danil Ivanov, and Mikhail Ovchinnikov. Formation-Flying Momentum Exchange Control by Separate Mass. *Journal of Guidance, Control, and Dynamics*, 38(8):1–10, 2015. ISSN 0731-5090. doi: 10.2514/1.G001137.

Dan Simon. *Optimal State Estimation: Kalman, H-Infinity, and Nonlinear Approaches.* Wiley-Interscience, first edition, 2006. ISBN 0471708585. doi: 10.1002/0470045345.

Joseph A. Starek, Behçet Açıkmeşe, Issa A. Nesnas, and Marco Pavone. Spacecraft Autonomy Challenges for Next-Generation Space Missions. In *Lecture Notes in Control and Information Sciences*, pages 1–48. Springer, 2016. ISBN 978-3-662-47694-9. doi: 10.1007/978-3-662-47694-9.

SR Starin. Design of a LQR controller of reduced inputs for multiple spacecraft formation flying. *American Control Conference*, 2:1327–1332, 2001.

M Suzuki, K Uchiyama, Derek Bennet, and Colin Mcinnes. Three-Dimensional Formation Flying Using Bifurcating Potential Fields. In *AIAA Guidance, Navigation and Control Conference*, pages 10–13, 2009. ISBN 978-1-60086-978-5. doi: 10.2514/6.2009-5884.

Michael Tillerson, Gokhan Inalhan, and Jonathan P. How. Co-ordination and control of distributed spacecraft systems using convex optimization techniques. *International Journal of Robust and Nonlinear Control*, 12(2-3):207–242, 2 2002. ISSN 1049-8923. doi: 10.1002/rnc.683.

MV Tollefson. Relative orbit design tool. *Aerospace Conference, IEEE Proceedings*, pages 3471–3478, 2001. ISSN 1095323X.

J. F. A. Tschauner and P. R. Hempel. Rendezvous zu einemin Elliptischer Bahn umlaufenden Ziel. *Acta Astronautica*, 11(2):104–109, 1965. ISSN 00046205.

UrtheCast. Fully-integrated, multispectral optical and Synthetic Aperture Radar (SAR) commercial constellation of Earth Observation satellites, 2015. URL https://blog.urthecast.com/updates/urthecast-announces-worlds-first-commercial-sar-and-optical-16-satellite-constellation/.

D. A. Vallado. *Fundamentals of Astrodynamics and Applications.* McGraw Hill Inc., 1997. ISBN 1881883140.

Avishai Weiss, Ilya Kolmanovsky, and Dennis Bernstein. Forward-integration Riccati-based output-feedback control of linear time-varying systems. In *American Control Conference*, number 11, pages 6708–6714, Montreal, Canada, 2012. ISBN 9781457710964.

James R Wertz. Coverage , Responsiveness , and Accessibility for Various “ Responsive Orbits ”. *3rd Responsive Space Conference*, 2005.

Hong Wong, Vikram Kapila, and Andrew G. Sparks. Adaptive output feedback tracking control of spacecraft formation. *International Journal of Robust and Nonlinear Control*, 12(2-3):117–139, 2 2002. ISSN 1049-8923. doi: 10.1002/rnc.679.

C. Wongsathan and C. Sirima. Application of GA to design LQR controller for an Inverted Pendulum System. *2008 IEEE International Conference on Robotics and Biomimetics*, (2):951–954, 2 2009. doi: 10.1109/ROBIO.2009.4913127.

M Xu, Yue Wang, and Shijie Xu. On the existence of J2 invariant relative orbits from the dynamical system point of view. *Celestial Mechanics and Dynamical Astronomy*, 112(4):427–444, 3 2012. ISSN 0923-2958. doi: 10.1007/s10569-012-9401-7.

Ming Xu, Yuying Liang, Tian Tan, and Lixin Wei. Cluster flight control for fractionated spacecraft on an elliptic orbit. *Celestial Mechanics and Dynamical Astronomy*, 125(4):383–412, 8 2016. ISSN 0923-2958. doi: 10.1007/s10569-016-9685-0.

SM Yoo, Sangjin Lee, C Park, and SY Park. Spacecraft fuel-optimal and balancing maneuvers for a class of formation reconfiguration problems. *Advances in Space Research*, 52(8):1476–1488, 2013. ISSN 0273-1177. doi: 10.1016/j.asr.2013.07.019.